STRUCTURAL, ELECTRONIC AND OPTICAL PROPERTIES OF CHALCOPYRITE TYPE SEMICONDUCTORS

A Thesis Submitted

In Partial fulfilment of the Requirements

for the Degree of

DOCTOR OF PHILOSOPHY

in

PHYSICS

by

SURABALA MISHRA

to the

DEPARTMENT OF PHYSICS

NATIONAL INSTITUTE OF TECHNOLOGY, ROURKELA

MAY, 2012

Dedicated

To My

Gurudev

&

Maa, Bapa

DECLARATION

I hereby declare that the work which is being presented in the thesis entitled **STRUCTURAL, ELECTRONIC AND OPTICAL PROPERTIES OF CHALCOPYRITE TYPE SEMICONDUCTORS** in partial fulfillment of the requirements for the award of the degree of **DOCTOR OF PHILOSOPHY** submitted to the Department of Physics of National Institute of Technology, Rourkela, is an authentic record of my own work under the supervision of Prof. Biplab Ganguli, Department of Physics. I have not submitted the matter embodied in this thesis for the award of any other degree or diploma of the university or any other institute.

31^{st} May, 2012 Surabala Mishra

CERTIFICATE

This is to certify that this thesis entitled : **STRUCTURAL, ELECTRONIC AND OPTICAL PROPERTIES OF CHALCOPYRITE TYPE SEMICONDUCTORS** has been carried out by **SURABALA MISHRA** under my supervision. No part of this work has been submitted elsewhere for degree.

Prof. Biplab Ganguli

Associate Professor

Department of Physics

National Institute of Tecnology

Rourkela 769008, India

31^{st} May, 2012

ACKNOWLEDGMENT

I wish to express my sincere gratitude to my supervisor Prof. Biplab Ganguli for his guidance, encouragement and support throughout my Ph.D programme. It is almost impossible to list out what all I got from him. His impressive knowledge, technical skills and human qualities have been a source of inspiration for me. In short working with him has been a pleasant and memorable experience of my life.

I gratefully thank my Doctoral Scrutiny Members, Prof. A. Satpathy, Prof. S. Jena and D.K. Bisoyi for their valuable contributions on this dissertation.

I am thankful to my friends Priyadarshini Parida and Satyabrata Satpathy for the patience and sincerity which they showed during the correction of the thesis.

I am especially grateful to my maa 'Basanti Mishra' and bapa 'Rabindra Kumar Mishra' who stood by me through testing times and provided me great moral and emotional courage. It would have been almost impossible to pursue my research work without their encouragement and support.

My special loving thanks goes to my husband who has always been the driving and inspiring force behind me.

I would like to thank my brother Amrut, sister Kunu, brother-in-law Susant, Goodly and grand mother for their special love and concerns. I am thankful to my father-in-law and mother-in-law for their constant support during my Ph.D programme.

This work was supported by Department of Science and Technology, India, under the grant no.SR/S2/CMP-26/2007. We would like to thank Prof. O.K. Andersen, Max Planck Institute, Stuttgart, Germany, for kind permission to use the TB-LMTO code developed by his group.

31^{st} May, 2012 Surabala Mishra

ABSTRACT

A theoretical study of the structural, electronic and optical properties of a series of group $I-III-VI_2$, $II-IV-V_2$, $I-III_2-VI_4$, $II-III_2-VI_4$, $I_2-III-VI_4$ and few substituted chalcopyrite type semiconductors are presented in this thesis. Systems studied are $AgAlM_2$ (M = S, Se, Te), $CuInSe_2$, $ZnSnX_2$ (X = P, As, Sb), AAl_2Se_4 (A = Ag, Cu, Cd, Zn), $CuIn_2X_4$ (X = S, Se), $CdGa_2X_4$ (S, Se, Te), $CdIn_2Te_4$, Cu_2InSe_4, $ZnXIn_2Te_4$ (X = O, Mn), $CdMGa_2S_4$ (X = Ag, Al), $CuNaIn_2S_4$, $CuLiIn_2Se_4$ and Cu_2InXSe_4 (X = Al, Ga) substituted chalcopyrite semiconductors. Our study is density functional theory (DFT) based first principle calculation within the frame work of tight binding linear muffin-tin orbital (TB-LMTO) basis.

The structural parameters such as lattice constants, anion displacement, tetragonal distortion and bond lengths are calculated by proper energy minimization. Bulk modulus of all the systems except $ZnXIn_2Te_4$ (X = O, Mn), are calculated by extended Cohen formula. Our study shows an inverse proportionality relation between lattice constant and bulk modulus for these systems. Band structure and total density of states (TDOS) of all the systems under study show that they are direct band gap semiconductors. AAl_2Se_4 (A = Ag, Cu), $CuIn_2X_4$ (X = S, Se) and Cu_2InSe_4 are p-type direct band gap semiconductors whereas $CdMGa_2S_4$ (X = Ag, Al) and $ZnXIn_2Te_4$ (X = O, Mn) are n-type direct band gap semiconductors. Our calculated results agree well with the available experimental results. Our study of partial density of states (PDOS) reveals that the contribution to upper valence band comes from the cation d and anion p hybrid orbitals in case of group $I-III-VI_2$, $I-III_2-VI_4$, $I_2-III-VI_4$ and their substituted chalcopyrites. This leads to a strong p-d hybridization. But this is not the case for the group $II-IV-V_2$,

$II - III_2 - VI_4$ and their substituted chalcopyrites. This is because cation d states behaves like core states and do not participate in p-d hybridization.

A quantitative estimate of effects of p-d hybridization and structural distortion on band gap and hence on electronic properties are carried out for $AgAlM_2$ (M = S, Se, Te), $CuInSe_2$ and $ZnSnX_2$ (X = P, As, Sb), AAl_2Se_4 (A = Ag, Cu, Cd, Zn), $CuIn_2X_4$ (X = S, Se), $CuNaIn_2S_4$ and $CuLiIn_2Se_4$ compounds. A significant reduction in band gaps are found for all the above systems due to the former effect. There is an increment of band gap due to the latter effect in the case of $AgAlM_2$ (M = S, Se, Te) and AAl_2Se_4 (A = Ag, Cu, Cd, Zn). Where as this effect on band gap is reversed in case of $CuInSe_2$ and $ZnSnX_2$ (X = P, As, Sb), $CuIn_2X_4$ (X = S, Se), $CuNaIn_2S_4$ and $CuLiIn_2Se_4$. Quantitative effect of cation-electronegativity on band gap of $ZnSnX_2$ (X = P, As, Sb) compounds is also carried out. Our study shows that there is an increment of band gap in these three systems with respect to their binary analogs due to this effect.

We calculate real and imaginary parts of the dielectric function, refractive index and absorption co-efficient in our optical properties study for the systems AAl_2Se_4 (A = Ag, Cu), $CuIn_2S_4$, $CdGa_2X_4$ (S, Se, Te), $CdIn_2Te_4$, $ZnXIn_2Te_4$ (X = O, Mn) and $CuNaIn_2S_4$ compounds. Static dielectric constants and static refractive index are also calculated for all the systems. We find a propertionality relation between static dielectric constant and refractive index. Our result agrees well with the available experimental and other theoretical results for systems studied by others.

We have explicitely caslculated optical matrix elements (OME) and joint density of states (JDOS) to show their respective contribution in the optical properties. Our result shows OME has greater contribition in the Infrared and visible region of the spectrum where as JDOS has greater contribution in UV region of the spectrum. Significant effects of

structural distortion and p-d hybridization on optical properties, JDOS and OME are also observed in case of the studied systems $AgAl_2Se_4$, $CuIn_2S_4$ and $CuNaIn_2S_4$. Effect of Na substitution in $CuIn_2S_4$ and Mn, oxygen substitutions in $ZnIn_2Te_4$ on optical properties are also reported. Their substitution significantly alters the optical properties of the host. Our study shows that chalcopyrites are anisotropic in nature and different optical properties get enhanced when photon is polarized $\perp$ c-axis.

Contents

List of Figures

List of Tables

Chapter 1

Introduction

Chalcopyrite is a copper iron sulfide mineral having chemical formula $CuFeS_2$. It crystallizes in tetragonal structure having space group $I\bar{4}2d$ (No.122) and cell dimension, a=5.289 $\mathring{A}$ and c=10.423 $\mathring{A}$. The crystal structure of the chalcopyrite was first described by Burdick and Ellis in 1917 [1]. The chalcopyrite structure is deduced from the diamond structure according to the Grimm-Sommerfeld rule [2] which states that if the average number of valence electrons per atom is equal to four then a tetragonal structure is formed. Figure 1.1 shows the deduction of the chalcopyrite structure from the diamond structure according to the Grimm-Sommerfeld Rule.

A group of materials that exhibits chalcopyrite structure with a composition of $I-III-VI_2$ were synthesized by Hahn et. al. in 1953 [3]. Here I is Cu/Ag, III is Al/Ga/In/Tl and VI is S/Se/Te and I, III, VI indicates the group number in the periodic table. He carried out the growth and structural characterization of these compounds by X-ray diffraction. These group of materials have been named after the mineral chalcopyrite ($CuFeS_2$) due to similar tetragonal structure. In 1954, Goodman and Douglass [4] discussed the possibility of semiconductivity in these materials. Thereafter these materials are known as

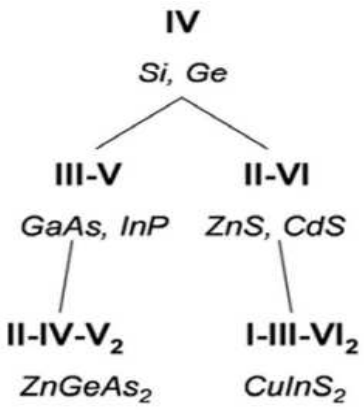

Figure 1.1: Origin of a chalcopyrite structure

chalcopyrite type semiconductors. More than fifty of such compounds are now known which belong to the group $I - III - VI_2$ and $II - IV - V_2$. Many defect systems of these type of chalcopyrite semiconductors have also been synthesized and studied. A series of single crystal defect chalcopyrites such as $HgAl_2Se_4$ were first grown by Hahn et. al. in 1955 [5]. These chalcopyrite semiconductors have been widely investigated since 1953 because of their wide range of applications. Most of the earlier works were based on the single crystal specimen. But the recent experimental investigations have been focused on thin film solar cell of these materials. The properties and promising applications of these materials are reviewed by Shay and Wernick [2].

The chalcopyrite compounds and their defect and doped/ substituted alloys are the interesting candidates from both experimental and theoretical points of view due to their potential applications in electro-optics, opto-electronic, non-linear optical devices, solar cell etc [2, 6–35]. They form a large group of semiconducting materials with diverse optical, electrical, and structural properties [2, 6–12]. These compounds are originally studied because of their low thermal conductivities. But they are now the promising candidates as non-linear optical materials and solar cells [13], photovoltaic detectors, modulators,

filters such as optical light eliminator filters [14], light-emitting diodes [15], nonlinear optics [16], and optical frequency conversion applications in all solid state based tunable laser systems [17]. Among the chalcopyrites $AgGaS_2$ and $CuGaS_2$ have band gaps in the visible part of the optical spectrum. Hence, it is easy to study with visible lasers such as Ar and HeCd lasers [2]. The narrow band gap of $AgGaSe_2$ makes it suitable as infrared detector including applications in photovoltaic solar cells and also in light emitting diodes [18, 19]. $AgGaS_2$ and $AgGaSe_2$ crystals have received more interest for the middle and deep infrared applications due to their large non-linear optical (NLO) coefficients and high transmission in the IR region [20–24]. So these are suitable candidates for nonlinear optical materials [25]. $AgGaS_2$ is used as a near infrared pumped optic parametric oscillators (OPO) [17]. $AgGaSe_2$ is used as a frequency doubler and tripler of CO_2 laser lines [17] because of the range of transparency in the infrared. Few defect chalcopyrite compounds like $CdGa_2Se_4$ and $CdAl_2S_4$ have found practical applications as tunable filters and ultra-violet photodetector [26, 27]. Few of the $II - III_2 - VI_4$ defect chalcopyrites are well known for acusto-optical or thermoelectric [28, 29] devices. Al containing defect chalcopyrite compounds, such as $CdAl_2Se_4$, $CdAl_2S_4$, $ZnAl_2Se_4$ etc. are the suitable materials for the applications in opto-electronics due to their wide range of transparency, high photo-sensitivity, high optical strength and strong luminescence properties [30, 31]. Various type of impurities including magnetic impurities may be doped/ substituted into the defect and pure chalcopyrite compounds to design a new class of materials, like dilute magnetic semiconductors (DMS) for spintronics application [32], optoelectronic devices [33] and solar cells [13]. $CdGa_2S_4$ doped with Cr is used as laser active material [34]. $Cu(In, Ga)Se_2$ thin-film solar cells have attracted the attention of the technologiest to become a leading member of the future solar-cell market [35]. So there are a series of wide

range of applications of the chalcopyrites and their related defect and doped/substituted chalcopyrite semiconductors.

1.1 Complexcity in Crystal Structure of Chalcopyrite

Chalcopyrite compounds of both the types "$A^{I}B^{III}C_2^{VI}$" and "$A^{II}B^{IV}C_2^{V}$" are ternary analogous of the zinc blende type binary compounds $A^{II}B^{VI}$ and $A^{III}B^{V}$ respectively [2, 36, 37]. The ternary chalcopyrites have some interesting structural anomalies [38, 39] relative to their binary analogous (figure 1.2). The tetragonal unit cell of a typical

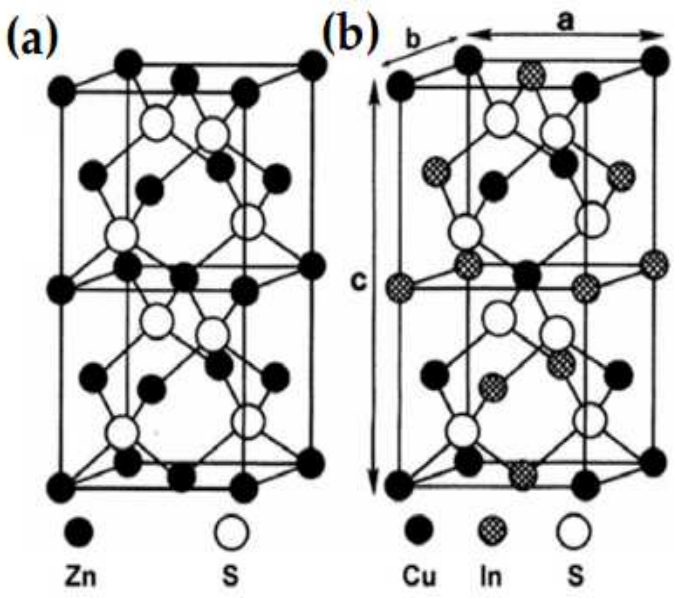

Figure 1.2: Structure of (a) zincblende (ZnS) (double cells) (b) chalcopyrite $(CuInS_2)$ structure (single cell).

chalcopyrite semiconductor consists of two Zinc blende unit cells. There are four group I/II atoms, four group III/IV atoms and eight group VI/V atoms per unit cell. First, it can be seen from figure 1.2 that the chalcopyrite structure can be derived from the zinc blende structure if one half of the cations (Zn) are replaced by copper and the other half

by indium atoms but the sulfur atoms remain unchanged in the same position. So there is a single cation in a zinc blende structure where as the ternary chalcopyrite havs two cations with different chemical properties. If A and B are two different cations then in the vertical direction, through intervals of $\frac{c}{2}$, the sequence $ABABAB\ldots$ is found. Whereas translating horizontally with an interval of a, the sequence $AAA\ldots$ can be found [36]. Second, due to the two different kinds of atoms occupying the cation sites, the lattice is slightly distorted. Therfore the interatomic distances between the anion C and the respective cations A and B are in general not equal in the chalcopyrite structure. This is called tetragonal distortion (η) where the ratio between the lattice parameters ($\eta \equiv c/2a$) differs from 1 [36]. Third, the anions are displaced from their zinc-blende sites. In binary (AC) zinc-blende compounds, each cation A has four anions C as nearest neighbors (and vice versa), where as in ternary chalcopyrite ABC_2 each cation A and B has four anions C as nearest neighbors, and each anion has two A and two B cations as nearest neighbors. As a result, the anion C usually adopts an equilibrium position close to one pair of cations than to the other. This is called anion displacement (u). This results unequal bond lengths, known as bond alternation. So the anion displacement measures the extent of bond alternation in the compounds [36].

1.2 Review of previous work

1.2.1 Experimental Work

A detailed study on $I-III-VI_2$ and $II-IV-V_2$ chalcopyrite semiconductor's growth, luminescent studies, non-linear optical properties, electrical-transport properties have been carried out by Shay et a1. [2]. Lerner [40] had grown single crystals of twelve

members of the group $I-III-VI_2$ and reported their semiconducting properties. Growth and properties such as energy gap and refractive index of five members of the group of single crystals of group $I-III-VI_2$ ($CuGaS_2$, $CuAlTe_2$, $AgGaS2$, $AgAlS_2$, $AgAlSe_2$) were studied by Honeyman et. al. [41]. Tell et. al. [42] studied the band structure and electro-reflectance spectrum for $AgMTe_2$ (M= Al, Ga, Te) at 77 K. The room temperature electrical properties of ten compounds of $I-III-VI_2$ family were also discussed by Tell et. al. [43]. Tang et. al. [44] investigated the electronic and optical properties of $AgGaS_2$ and $AgGaSe_2$ by both theoretical and experimental tecnique. The phase transition in $AgGaS_2$ and $AgGaSe_2$ [45], the optical absorption, single crystal x-ray diffraction and electronic structure calculation of $AgGaSe_2$ [46], high-pressure X-ray diffraction measurement of $AgGaTe_2$ [47] and structural, electrical and optical properties of $CuInSe_2$ thin films were reported by many researchers [48–51]. Study of electrical and luminescent properties of bulk $CuInSe_2$ and dependence of hall parameters on temperature for $CuInSe_2$ single crystals had been carried out by Migliorato et. al. [52] and Horig et. al [53] respectively. Electrical properties of few $I-III-VI_2$ chalcopyrite compounds grown by solid state growth method were reported by Ashida et a1 [54]. Optical properties of a series of chalcopyrite semiconductors such as $AgGaS_2$, $ZnGeAs_2$, $ZnGeP_2$, $CuGaS_2$, $CuAlS_2$, $CuInSe_2$ and $AgInSe_2$ have also been studied by Boyd et.al. [55] and Rife et.al.[56]. X-ray photo emission measurements of the valence band density of states and core levels of $CuAlS_2$ was discussed by Luciano [57]. Several studies have been carried out on the elctronic, electrical and optical properties of $CuAlX_2$ (S,Se,Te) at ambient pressure [58, 59]. Optical functions and electronic structure of $CuInSe_2$, $CuInS_2$,$CuGaS_2$ and $CuGaSe_2$ at room temperature were studied by Alonso and his group [60]. EPR and optical properties were studied for $Cu-III-VI_2$ [61], $CuAlS_2$

[62], $CuAlS_2$ [63], $CuAlS_2$ [64] to investigate the point defects in these semiconductors. The crystal field and spin orbit interactions at the fundamental gap of $AgGaS_2$ was carried out by Artus et. al. using a linear hybridization model [65]. They had estimated the d-level hybridization percentage. A study on p-d hybridization of the valence bands of $I-III-VI_2$ compounds is reported by Shay et. al.[66]. They have shown that the valence bands of $I-III-VI_2$ compounds result from hybridization of the noble metal d levels with p levels of the anion atoms. They have estimated that the uppermost valence bands are 40% d-like in the Cu compounds and $\sim 20\%$ d-like in Ag compounds. Hsu [67] has studied p-d hybridization in $CuInS_2$ by photoreflectance. In his work he has used a simple model to measure the separation energy between the p and d levels, the interaction strength between these levels and the d-electron contribution to different energy levels. He has also shown that the d-contribution decreases when temperature increases. Negative crystal-field splitting of the valence band in $CdSnP_2$ [68] and the optical properties and the electronic band structure were studied by Shay and his group [69]. Electronic properties and pinnig of the Fermi level in irradiated in $II-IV-V_2$ semiconductors were studied by Brudnyi [70].

Extensive experimental work has been carried out on group $II-III_2-VI_4$ defect chalcopyrites semiconductors [71–84]. The structural refinement of $ZnIn_2S_4$ single crystal [71], the structure and phase transitions of the defect-stannite $ZnGa_2Se_4$ and defect-chalcopyrite $CdGa_2S_4$ [72], crystal structure and structural parameter of $HgAl_2Se_4$ [73] and the growth of $CdIn_2S_4$, $ZnIn_2S_4$ and $CdGa_2S_4$ single crystals [74] are well investigated. S. Ozaki et. al. have carried out both experimental and theoretical studies to calculate the optical properties and electronic band structure of $ZnIn_2Te_4$, $CdGa_2Te_4$ and $CdIn_2Te_4$ [75–77]. Different studies on $CdIn_2Te_4$ such as optical and transport

properties [78], band gap and valance band splitting [79], the dielectric constant measurement [80], low and high electric field transport [81], infrared and Raman spectra [82] were carried out by different workers. Raman and infrared spectra of $CdIn_2S_4$ and $ZnIn_2S_4$ and point defects in p-type $CdIn_2Te_4$ were studied by Unger et. al. [83] and You et. al. [84] respectively.

During last decade or so the work on doped/ substituted chalcopyrite semiconductors have accelerated due to their wide range of device applications. Albbornoz et.al. have found significant changes in electronic and optical properties of $CuInSe_2$ when oxygen is included by annealing [85]. Ishida et. al. successfully synthesized Mn doped $ZnGeP_2$ system [86] and they have studied the various Mn states and p-d exchange interaction. The optical properties of $CuIn_{1-x}Ga_xSe_2$ epitaxy single crystal layer was determined by spectroscopic ellipsometry (SE) method [87], Diifferent properties of Na incorporated $CuInS_2$ was carried out by several workers [88–90]. Magnetic properties of Mn doped $CuInS_2$ [91] and $ZnSiAs_2$ [92] are studied. Souilah et.al. [93] have reinvestigated the crystal structure of bulk CIGS compound for both stoichiometric and Cu-poor composition. Structural, electrical and optical properties of Zn-doped $CuInS_2$ thin films [94, 95], annealed Sb [96, 97] and Na doped [98] $CuInS_2$ thin films have been studied by different researchers. Optical constants of Na-doped $CuInS_2$ thin films were calculated by Zribi et.al. [99]. Several other works such as Seebeck co-efficient and optical properties study of Cd-doped $CuInS_2$ single crystal [100], preparation of Sn, N, P doped $CuIns_2$ thin films by co-evaporation technique [101] absorption and photoluminescence studies of Cr doped $CdGa_2S_4$ [102], optical and charge transport properties of $CuIn_{1-x}Ga_xSe_2$ solar cell [103], structural study of Ge doped $CuGaSe_2$ [104], growth, structure and optical properties of $Li_xCu_{1-x}InSe_2$ thin films [105], structural, electronic

and optical calculations of $Cu(In, Ga)Se_2$ chalcopyrite [106], structural characterization of the dilute magnetic semiconductor $CuGa_(1-x)Mn_xSe_2$ [107], magnetic properties of $Zn_(1-x)Mn_xIn_2Te_4$ semiconductor for concentration $0.3 < x < 1.0$ [108], effect of sodium and oxygen doping on the conductivity of $CuInS_2$ thin films [109] were carried out by different researchers .

1.2.2 Theoretical Works

In 1972 J.L. Shay et.al. [110] had pointed out that the anomalous reduction in the band gaps of chalcopyrites relative to their binary analogous is due to the existence of d bonding in the former compounds. They had suggested that $CuAlS_2$, $CuGaS_2$, $CuGaSe_2$ and $CuInSe_2$ have nearly constant percentage of d character where as $CuInS_2$ has the largest $\%$ of d character in this group. They had suggested that the decrement in band gaps of the ternary chalcopyrite relative to their binary analogous results extensively from the existence of d-character in the chalcopyrite compounds. Their correlation showed 75% d character for $CuAlS_2$ in contrast with the experimental value 35%. This disagreement with experimental results indicates that the d-character could not be the only factor which controls the band gap anomaly. So there may be some other factors which influence the band gap of the chalcopyrite compounds. In 1984 Jaffe et.al. [36, 38] filled up this gap. They used self consistent band structure methods to analyze the remarkable anomalies ($> 50\%$) in the energy band gaps of $IA - IIIB - VIC_2$ compounds (e.g. $CuGaS_2$) relative to their zinc blende analogous $IIA - VIB$ (e.g. ZnS). They suggested that this happens due to p-d hybridization, cation- electronegativity and structural distortion effects. They basically gave a qualitative idea about the effect of the above three factors on the density of states and band structure of these semiconductors. They also showed how

the non-ideal anion displacement and the lattice constants of all the ternary chalcopyrites can be obtained from elemental co-ordinates without using experimental data. In another work Jaffe et. al. [39] calculated self consistently the electronic structure of six Cu-based ternary chalcopyrite semiconductors within the density functional formalism. They used the potential-variation mixed basis (PVMB) approach to analyze the chemical trends in the band structure, electronic charge density, density of states, chemical bonding and percentage of d-character for all these chalopyrites. In contrast to Shay et.al. [110] results, their result showed that the band gap anomaly is partly induced from the d-orbital character. They showed that $CuAlS_2$ has the highest d-character in the series and $CuInS_2$ and $CuInSe_2$ have the lowest d-character. This is in contrast with the suggestion of Shay et.al. [110]. Poplavnoi et.al. [111] used non-self consistent empirical pseudopotential method, neglecting the noble atom d-orbitals and anion displacement to calculate the band structure which led to produce larger gaps and narrower bands than the calculated band structure of of Jaffe. et.al. [39]. In another work, Poplavnoi [112] included the structural effect and calculated the band structure for $CuAlS_2$, $CuAlSe_2$ and $CuInS_2$, $CuInSe_2$. Yoodee et.al [113] studied the effect of p-d hybridization of the valence band of $I-III-VI_2$ chalcopyrites using a model developed, by adding the effect of p-d hybridization and the crystal field to the Hamiltonian of the Kane model [114]. Oguchi et.al. [115] had applied the self consistent numerical LCAO approach to study the band structure of $CuAlS_2$ and $CuGaS_2$. Several first principle studies of different properties of chalcopyrite semiconductors, within density functional formalism, such as band offsets and optical bowings of chalcopyrite [116], defect formation energy in $CuInSe_2$, $CuGaSe_2$ and $CuAlSe_2$ [117], defect properties of $CuInSe_2$ and $CuGaSe_2$ [118], band structure anomalies of $CuGaX_2$ versus $AgGaX_2$ (X=S, Se, Te) and their alloys [119],

structural phase transition, elastic properties and electronic properties of $CuAlX_2$ (X=S, Se, Te) [120], electronic and structural properties of $CuAlX_2$ (X=S,Se,Te) [121, 122], volume-dependent elastic and lattice dynamical properties of $CuGaSe_2$ [123], calculation of vibrational spectra of $AgInSe_2$ [124], structural, electronic and optical properties of $CuGaS_2$ and $AgGaS_2$ [125] were carried out by different researchers. Bulk modulus [126, 127], microhardness [126], dielectric properties [128] of a series of $I-III-VI_2$ and $II-IV-V_2$ chalcopyrite semiconductors were also carried out. Electronic structure calculation of $ZnSiP_2$, $ZnGeP_2$, $ZnSnP_2$, $ZnSiAs_2$ and $MgSiP_2$ and structural and chemical changes in $MgSiP_2$ chalcopyrite with respect to its binary analogous were performed by Jaffe et.al. [129] and Martins et.al. [130] respectively using first principle density functional theory. Several literature are reported for the structural, electronic and optical properties of group $II-IV-V_2$ chalcopyrite semiconductors [131–136]. Some interesting properties such as anomalous grain boundary in polycrystalline $CuInSe_2$ [137] and intrinsic DX centers in $CuInSe_2$ [138] were studied by Zunger and his group.

Electronic band structure study of a series of ordered vacancy compounds with formula $II-III_2-VI_4$ was carried out by Jiang et.al. [139]. They clarified the relationship with the band structure of the the few of the group $II-III_2-VI_4$ compounds with $I-III-VI_2$ chalcopyrites and $II-VI$ binary compounds. They introduced an empirical correction for the band gaps beyond LDA. But they have used the experimental structural parameters to calculate the band gaps of the defect $II-III_2-VI_4$ chalcopyrites. Electronic band structure study of $CdGa_2Se_4$ [140], Bulk moduli and band structure of $ZnGa_2X_4$ [141], electronic properties of $CdIn_2Se_4$ [142], ab initio calculations of electronic structure of $CdGa_2S_4$ [143], ab-initio study of the structural, linear and nonlinear optical properties of $CdAl_2Se_4$ [144], structural, electronic and optical

properties of $HgAl_2Se_4$ [145], birefringence, linear and nonlinear second order susceptibilities of $HgGa_2S_4$ [146] are reported in literature for the better understanding of the physical and chemical properties of the of defect chalcopyrite semiconductors. Ganguli et.al. [147] had studied the band structure and optical properties of $ZnIn_2Te_4$ defect chalcopyrite semiconductors using density functional based TB-LMTO and NMTO first principle technique. They had used the experimental lattice parameters [75] and excluded the structural distortion in their calculation. Structural, electronic, linear and non-linear optical properties of the same defect chalcopyrite compound using FP-LAPW method was studied by Ayeb et.al.[148].

Mahadevan et.al. [149] and Zhao et.al. [150] investigated the magnetic properties of Mn doped $II - IV - V_2$ chalcopyrite semiconductors. The optical properties of high-efficiency photovoltaic material $CuGaS_2$, substituted by Ti atoms in place of Ga atoms, were studied by Aguilera et.al. [151]. Their study showed that Ti substituted material is able to absorb photons of energy lower than the band gap of $CuGaS_2$. Electronic band structure of transition metal substituted chalcopyrites ($Cu_4MGa_3S_8$ with M = Ti, V, Cr, Mn) [152] and the structural, electronic and magnetic properties of Mn doped $BeSiAs_2$ and $BeGeAs_2$ compounds [153] were investigated by means of ab initio calculation. Yamamoto et.al. studied the electronic structures of Na incorporated In rich bulk $CuInS_2$ [154] and $CuInS_2$ thin film [155] based on ab-initio band structure calculation and XPS study. They carried out both theoretical calculation and experiments and concluded that for p-type In rich $CuInS_2$ thin films, Na incorporation in Cu site is stable but in other site it is unstable. Yi et.al. [156] had presented ab-initio pseudopotential density functional calculations for the electronic and magnetic structure of Cr containing $CdGeP_2$ chalcopyrite semiconductor. These materials offer a potential for the spintronics appli-

cations at room temperature. Several remarkable works had been reported for different doped chalcopyrite materials [157–160]. The n-type doping of halogen in $CuInS_2$ [161] and the n-type doping of $CuInSe_2$ and $CuGaSe_2$ are also reported.

1.3 Motivation

Our literature survey shows that these systems are very important for both application point of view and from physics and chemistry point of view. Literature survey shows that it is obvious that due to presence of group IB transition metal, the d-electrons participate in chemical bonding in group $I-III-VI_2$. Therefore it is important to know how much contribution of d-electrons are there and how they influence the electronic properties and hence optical and magnetic properties. The effects of structural distortion, p-d hybridization and cation-electronegativity are found in group $I-III-VI_2$ and $II-IV-V_2$ systems. These effects make these systems interesting from both physics and chemistry point of view. A qualitative study of the effect of the above three factors on band gap and electronic properties are reported in literature. But we do not find detailed quantitative calculation of these effects. Detail band structure and bulk modulus are not also reported in literature for many pure chalcopyrite compounds.

Defect chalcopyrites of the type AB_2C_4 and A_2BC_4 are more porous and so they have rich chemistry. These structure have vacancies at certain sites. But these defects do not break the translational symmetry. Since they have vacancies, impurity elements including magnetic impurities can be doped/substituted by suitable elements to synthesize new materials. We do not find any sufficient band structure calculations for the substituted chalcopyrites where the substitution is 50% in cation place. Like pure chalcopyrites,

no quantitative effects of the structural, p-d hybridization and cation-electronegativity on electronic properties and hence on optical properties are reported in literature for defect and doped chalcopyrites. For many of these systems bulk modulus are also not available. Though some optical properties studies are found for defect systems, we do not find any study which show the structural and p-d hybridization effects on optical properties. We do not find any optical study of defect and substituted chalcopyrites where the effect of optical matrix elements on optical response functions is discussed in detail. In our work we have tried to fill up these gaps.

Currently there is an extensive search for new materials for the next generation of semiconductor devices which would exploit electronic, optical and magnetic properties as well. Our work would be of great importance in these directions. Much of physics can still be explored of these systems, doped with different types of impurities. The main thrust of our work is to understand the physics of defect/substituted systems.

1.4 Objective

Our main objectives are to understand the physics of p-d hybridization, structural distortion and nature of bonding for electronic properties of chalcopyrite type semiconductors. Detailed analysis of linear optical properties is another objective to understand the factors which control these properties. To address the above mentioned objectives, we carried out the following detailed studies.

- To calculate the structural paramters and bondlengths of $AgAlM_2$ (M = S, Se, Te), $CuInSe_2$ and $ZnSnX_2$ (X = P, As, Sb), AAl_2Se_4 (A = Ag, Cu, Cd, Zn), $CuIn_2X_4$ (X = S, Se), $CdGa_2X_4$ (S, Se, Te), $CdIn_2Te_4$, and Cu_2InSe_4, (belong to group

$I - III_2 - VI_4$, $II - III_2 - VI_4$ and $I_2 - III - VI_4$) and $ZnXIn_2Te_4$ (X = O, Mn), $CdMGa_2S_4$ (X = Ag, Al), $CuNaIn_2S_4$, $CuLiIn_2Se_4$ and Cu_2InXSe_4 (X = Al, Ga) substituted chalcopyrite semiconductors.

- To calculate the bulk modulus of the above systems except $ZnXIn_2Te_4$ (X = O, Mn) substituted chalcopyrites using extened Cohen formula.

- To study the electronic properties such as band structure, total density of states (TDOS) and partial density of states (PDOS) of the above mentioned systems.

- To show the quantitative effects of p-d hybridization and structural distortion on band gap and in general the total electronic properties.

- To show the quantitative effect of cation-electronegativity on band gaps in $ZnSnX_2$ (X = P, As, Sb) with respect to their binary analogs.

- To study the detail optical response functions like imaginary and real part of dielectric functions, refractive index and absorption co-efficient in AAl_2Se_4 (A = Ag, Cd), $CuIn_2S_4$, $CdIn_2Te_4$, $CdGa_2X_4$ (X = S, Se, Te) compounds and $CuNaIn_2S_4$, $ZnXIn_2Te_4$ $(X = O, Mn)$ substituted chalcopyrites.

- To study the effects of joint density of states (JDOS) and optical matrix elements (OME) on imaginary part of dielectric function and hence on over all optical properties.

- To study the effect of structural distortion and p-d hybridization on JDOS and OME, hence on other optical response function in $AgAl_2Se_4$, $CuIn_2S_4$ and $CuNaIn_2Se_4$ compounds.

- To study the effects of Na, Mn and oxygen subtitutions on optical properties of $CuIn_2S_4$ and $ZnIn_2Te_4$ defect chalcopyrite systems respectively.

Chapter 2

Theory of Electronic Properties

The stationary states of a quantum mechanical system is given by the Schrödinger equation

$$\left[-\nabla^2 + V(\mathbf{r})\right] \psi_n(\mathbf{r}) = \varepsilon_n \psi_n(\mathbf{r}) \tag{2.1}$$

This equation can be exactly solved for simple systems like H atom as the potential energy $V(\mathbf{r})$ of the electron in the electrostatic field of the proton is known to be $-\frac{2}{r}$ (in CGS system), where r is the electron nucleus-distance. However as we move towards higher Z elements and their compounds or solids, the electrostatic repulsion among the multiple electrons in presence of the attractive centers (i.e. nuclei) make the solution of the problem very difficult. Such problems become more intractable due to quantum mechanical electron-electron exchange and correlation effects. One way to solve this problem is to replace the many-electrons problem to an effective one-electron problem. But this can be done by introducing certain approximations. Several approximations such as Born and Oppenheimer approximation (adiabatic approximation) [164], self consistent field approximation by Slater [165] are considered to solve such problem.

The most successful theory to tackle such a problem is density functional theory (DFT) of Hohenberg-Kohn-Sham [166, 167]. DFT reduces the quantum mechanical ground state many-electrons problem to self consistent one-electron form through the Kohn-Sham equation [168]. This is an extremely successful approach for the description of ground state properties of metal, semiconductors and insulations. The success of DFT not only encompasses standard bulk materials but also complex materials such as proteins and carbon nanotubes.

DFT is based on two Hohenberg-Kohn [166] theorems. The first theorem asserts that the electronic charge density of any system determines all ground state properties of the system that is $E = E[\rho_0]$, where the energy E is a functional of ρ_0, the ground state electronic charge density of the system. The second H-K theorem shows that there exists a variational principle for the above energy density functional $E = E[\rho']$. Namely, if ρ' is not the ground state electronic charge density of the above system, then $E = E[\rho'] > E[\rho_0]$. Kohn and Sham [167] gave a prescription for a mapping of the interacting many body-electron system onto a system of non-interacting electrons moving in an effective potential due to all other electrons and ions. The one electron energy Kohn-Sham equation is given by

$$\left[-\nabla^2 + V_{eff}(\mathbf{r})\right] \psi_i(\mathbf{r}) = \varepsilon_\mathbf{i}\psi_\mathbf{i}(\mathbf{r}) \tag{2.2}$$

where the effective potential,

$$V_{eff}(\mathbf{r}) = 2\int dr' \frac{\rho(\mathbf{r}')}{|\mathbf{r}-\mathbf{r}'|} + 2\sum_R \frac{Z_R}{|r-R|} + \frac{\delta E_{XC}[\rho]}{\delta\rho(\mathbf{r})} \tag{2.3}$$

The effective potential consists of the Hartree potential (1st term in R.H.S), the external or ionic potential V_{ext} (2nd term) and the exchange-correlation potential (3rd term). In KS equation, the total electronic energy is a functional of electron density which is calculated

using variational principle. This requires self consistent calculation. The KS equation (eq.2.2) is of same form as the Schrödinger equation (eq. 2.1) but the only difference is that the single particle potential is replaced by the effective potential. The XC potential describes the effects of the Pauli exclusion principle and the Coulomb potential beyond a pure electrostatic interaction of electrons. The exact form of the exchange correlation is unfortunately not known. The exact knowledge of this implies that the exact solution of the entire many body problem is known. So one needs to introduce some approximation and the most successful and well tested is the so called local density approximation (LDA) [168]. In LDA, the exchange-correlation energy functional $E_{XC}[\rho]$ is taken to be the same as for the homogeneous electron gas with the replacement of the constant density ρ_0 by the local density $\rho(\mathbf{r})$ around each volume element $d\mathbf{r}$ of the actual inhomogeneous systems. If the density of the system is slowly varying, say on the scale of the Fermi wavelength λ_F, then each small element of the electronic system can be thought of as uniform, suggesting the following approximation to $E_{XC}[\rho]$.

$$E_{XC} = \int \rho(\mathbf{r})\epsilon_{XC}[\rho(\mathbf{r})]d\mathbf{r} \tag{2.4}$$

Here $\epsilon_{XC}[\rho]$ is the exchange correlation energy per particle for a uniform system of density $\rho(\mathbf{r})$. These XC potentials have been approximated by different authors such as von Barth-Hedin [169], Barth-Hedin modified by Janak [170], Slater X_α [171] etc. We have used von Barth-Hedin exchange correlation potential [169] for our calculation. DFT with LDA and other exchange correlation is a major tool in computational condensed matter physics. It is applicable to all atoms in periodic table (alkali, transition, actinide). It can be used for metallic, covalent, ionic or even Van der Waals solids. LDA does have limitations to explain strongly correlated phenomena. These limitations may be ressolved

by a new developments such as LDA+U. Basically in DFT one has to find a self consistent solution of Kohn-Sham equation (equation 2.2) which leads to the true ground state density. In practice, for calculating the band structure of a solid, the Kohn Sham (KS) orbitals $\psi_i(\mathbf{r})$ are usually expanded in terms of some chosen basis functions with some coefficients which are to be determined variationally. The choice of basis set may lead to the nearly correct solution of the one-electron band structure problem.

There are different approaches for the choice of the basis set and hence to find the solution of the one electron band structure.

(a) Fixed basis method such as LCAO method

(b) Partial wave method such as KKR method.

The approach (a) is straight forward and versatile but less accurate. The approach (b) is sophisticated and time taking but highly accurate. There is another approach called linear muffin tin orbital method (LMTO). The LMTO method not only establishes the connection with both LCAO and KKR-ASA method but also combines the desire features of both. Here basically one derives an energy independent basis set from the energy dependent partial waves in the form of muffin tin orbitals. Then this gives a fast efficient and reasonably accurate prescription for computing one electron energies and wavefunctions for all the elements in the periodic table.

LMTO is the linearized version of KKR multiple scattering method which is the most accurate partial wave band structure method. It leads to the smallest Hamiltonian and overlap matrices and hence faster from the computational point of view. In this method it is also possible to define a localized basis such that the Hamiltonian can be recast in a tight binding form (TB-LMTO). This can be solved in reciprocal as well as in real space. This TB-LMTO method gives very good result for the compounds having localized d and

f orbitals. For the first principle calculations of the electronic structure of solids, LDA based TB-LMTO-ASA is the most handy tool and it is also known as “minimal basis set” method. This is the only method which can be implemented at different levels of sophistication and can be run even on PC. Density of states (DOS), band structure, electron density and total energy can be calculated easily for non-magnetic, ferromagnetic, antiferromagnetic solids in bulk, surface or interface/multilayer. There are three fundamental concepts that laid the foundation of TB-LMTO [174]. Brief description of this method is discussed in the following sections.

2.1 Tight Binding Linear Muffin Tin Orbital-Atomic Sphere Approximation

The starting point is the Kohn-Sham equation with the muffin tin effective crystal potential. The basis chosen for representation of the wavefunction are the muffin tin orbitals. The muffin tin approximation to the potential is nothing but a spherically symmetric potential $V_R(\mathbf{r})$ centered at the position of each atom and within a sphere of radius r_{MT}. A constant potential V_0 is assumed between the spheres.

$$V(r_R) = \sum_R V_R(|\mathbf{r} - \mathbf{R}|) + V_0 \tag{2.5}$$

where $\mathbf{R}$ is the position of ions cores and $\mathbf{r}$ is the position of the electron. A radius S_R around $\mathbf{R}$ is defined within which it is assumed that the potential is spherically symmetric. These spheres are called muffin tin spheres. In the interstitial region, the potential is

assumed to vary very slowly. But in muffin tin approximation, the slowly varying potential in interstitial region is replaced by a constant average potential. The resulting potential is called muffin tin potential. A schematic diagram showing the approximation is given in

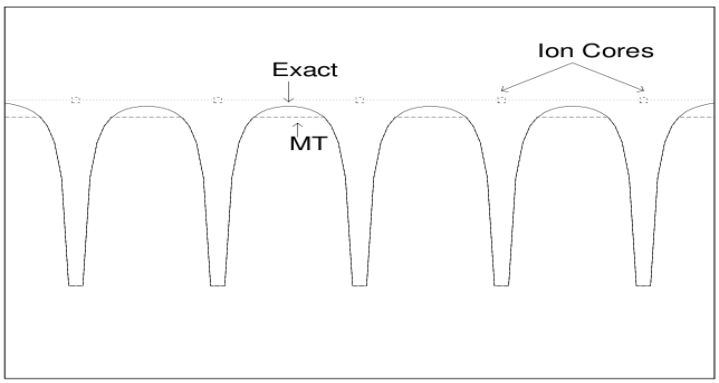

Figure 2.1: Construction of Muffin-Tin potential.

figure 2.1 and a more realistic illustration of muffin tin approximation is given in figure 2.2.

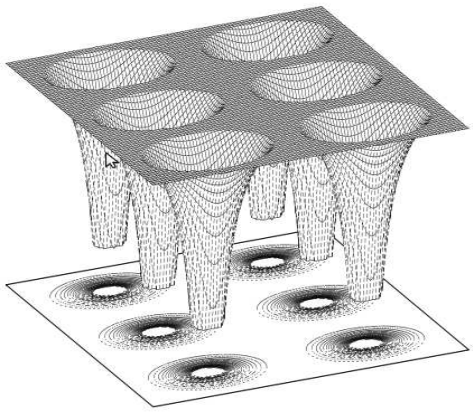

Figure 2.2: Muffin-Tin orbital potential.

The Schrödinger equation for the single electron wave function is given by

$$\left[-\frac{\hbar^2}{2m}\nabla^2 + V(r_R)\right]\phi_{RL}(\varepsilon, r_R) = \varepsilon\phi_{RL}(\varepsilon, r_R) \tag{2.6}$$

Within the MT approximation the one electron Schrödinger equation can be solved in two regions i.e. inside the MT sphere and in the interstitial regions. So the potentials in these

regions are given by

$$V(r) = \begin{cases} V_R(r), & r_R \leqslant S_R \\ \\ V_0, & r_R > S_R, r_R = |\mathbf{r} - \mathbf{R}| \end{cases} \tag{2.7}$$

Equation 2.7 can be solved for the region $r_R \leqslant S_R$ (inside sphere) in which potential is symmetric and

$$\phi_{RL}(\varepsilon, r_R) = \phi_{Rl}(\varepsilon, r_R) Y_L(\hat{\mathbf{r}}) \tag{2.8}$$

where $\phi_{Rl}(\varepsilon, r_R)$ are the solutions for a single MT well inside the muffin tin sphere. This is obtained from the numerical solutions of the radial Schrödinger equations.

$$\frac{d^2}{dr_R^2} r_R \phi_{Rl}(\varepsilon, r_R) = \left[V_R(r_R) + \frac{l(l+1)}{r_R^2} - \varepsilon \right] r_R \phi_{Rl}(\varepsilon, r_R) \tag{2.9}$$

The radial equation to find the solution for the constant potential out side the sphere is

$$\left[\frac{d^2}{dr_R^2} + \frac{l(l+1)}{r_R^2} - \kappa^2 \right] r_R \phi_{Rl}(\varepsilon, r_R) = 0 \tag{2.10}$$

where

$$\kappa^2 = \varepsilon - V_0 \tag{2.11}$$

The solution outside the spheres are represented as linear combination of the spherical Bessel function $j_l(\kappa, r_R)$ and the spherical Neumann function $n_l(\kappa, r_R)$. So the total solution around a single MT well can be written as

$$\chi_{RL}(\varepsilon, \kappa, r_R) = Y(\hat{\mathbf{r}}_{\mathbf{R}}) \begin{cases} \phi_{Rl}(\varepsilon, r_R), & r_R \leqslant S_R \\ \\ n_l(\kappa, r_R) - \cot \eta_{Rl}(\varepsilon, \kappa) j_l(\kappa, r_R), & r_R > S_R \end{cases} \tag{2.12}$$

Here L is used as a combined index for $\{lm\}$ and r_R refers to $|\mathbf{r} - \mathbf{R}|$. κ^2 can be represented as the kinetic energy in the "interstitial region" which can be positive or negative

depending on ε lying above or below the V_0 value. $\eta_{Rl}(\varepsilon,\kappa)$ is known as the "phase shift" of the l^{th} partial wave which , along with the normalization of $\phi_{Rl}(\varepsilon,r_R)$ can be determined by matching the partial waves and its derivatives at the MT spheres boundary [174].

Mathematically the matching is done via the Wronskian relation

$$\cot\eta_l(\varepsilon,\kappa)=\frac{W[\phi_l(\varepsilon,r_R),\eta_l(\kappa,r_R)]}{W[\phi_l(\varepsilon,r_R),j_l(\kappa,r_R)]}$$

$\cot\eta_l(\varepsilon,\kappa)$ is directly related to the potential function $P_{Rl}(\varepsilon,\kappa)$ which are monotonically increasing function of ε. The outside solution i.e. the "tail" of the partial wave depends on energy ε via the phase shift $\eta_{Rl}(\varepsilon,\kappa)$ and when $\kappa^2<0$ $(\varepsilon<V_0)$, it diverges exponentially. Therefore it is useful to add the function $\cot\eta_{Rl}(\varepsilon,\kappa)j_l(\kappa,r_R)$ to the partial wave and the equation 2.11 and 2.12 can be written as

$$\chi_{RL}(\varepsilon,\kappa,r_R)=Y_L(\hat{\mathbf{r}}_\mathbf{R})\begin{cases}\phi_{Rl}(\varepsilon,r_R)+\cot\eta_{Rl}(\varepsilon,\kappa)j_l(\kappa,r_R), & r_R\leqslant S_R\\ n_l(\kappa,r_R), & r_R>S_R\end{cases}\tag{2.13}$$

Equation 2.13 ensure that the head (inside sphere) and the tail (outside sphere) of the above function match continuously and differentiably at the muffin tin boundary at S_R. These functions are called muffin tin orbitals (MTO) and qualify as suitable basis for representation of the wavefunctions in solids. It is because these basis are such that its head contains all the informations about the potentials while its tail contains informations only about the constant potential outside the muffin-tin sphere. In this basis, the tail part is the Neumann function $n_l(\kappa,r_R)$ and the head part is $\phi_{Rl}(\varepsilon,r_R)+\cot\eta_{Rl}(\varepsilon,\kappa)j_l(\kappa,r_R)$ which joins smoothly and differentiably with the tail.

This is illustrated in figure 2.3 . This is the partial waves and muffin tin orbitals asso-

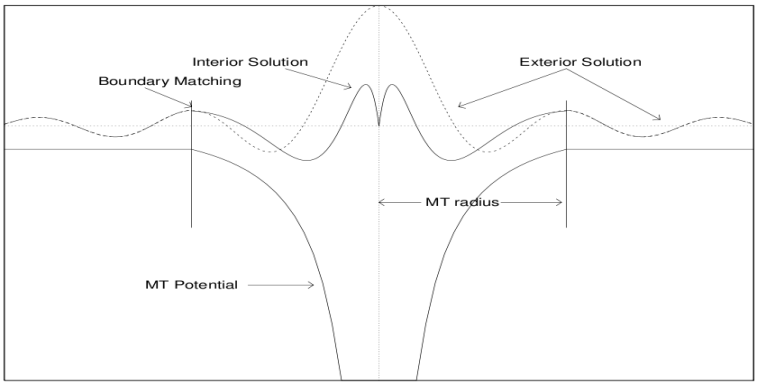

Figure 2.3: Construction of Muffin-Tin orbital.

ciated with a single muffin-tin potential. But it is necessary to introduce the wavefunction solution of the whole solid muffin tin potential of type shown in figure 2.1. So the wavefunction must be expanded as a linear combination of the muffin tin orbitals associated with individual muffin tin potentials centered at different sites $\{\mathbf{R}\}$. The condition for this is that the multi-center expansion of the MTOs should be expressible in terms of the one-center partial wave expansion. i.e.

$$\psi(\varepsilon, r_R) = \sum_{RL} \chi_{RL}(\varepsilon, \kappa, r_R) C_{RL} \tag{2.14}$$

The expression for the tail of the Neumann function $n_l(\kappa, r_R)$ outside its sphere can be written as

$$n_l(\kappa, r_R) = \sum_{L'} j_{L'}(\kappa, r_R) B_{R'L',RL}(K) \tag{2.15}$$

where $B_{R'L',RL}(K)$ are the Hermitian KKR structure matrix. If we consider one MT sphere (eq. 2.13) then the 1st term inside the atomic sphere i.e. $Y_L(\hat{\mathbf{r}}_\mathbf{R})\phi_{Rl}(\varepsilon, r_R)$ is already a solution of the Schrödinger equation. But the total head part i.e. $Y_L(\hat{\mathbf{r}}_\mathbf{R})\phi_{Rl}(\varepsilon, r_R) + \cot\eta_{Rl}(\varepsilon, \kappa) j_l(\kappa, r_R)$ is not a solution of Schrödinger equation. So the head part will be a solution of Schrödinger equation if and only if the tails from the other spheres cancel the 2nd term of the head part. i.e.$Y_L(\hat{\mathbf{r}}_\mathbf{R}) \cot\eta_{Rl}(\varepsilon, \kappa) j_l(\kappa, r_R)$. Now the head part is the

solution of the Schrödinger equation. This is called the tail cancellation [175]. The clear

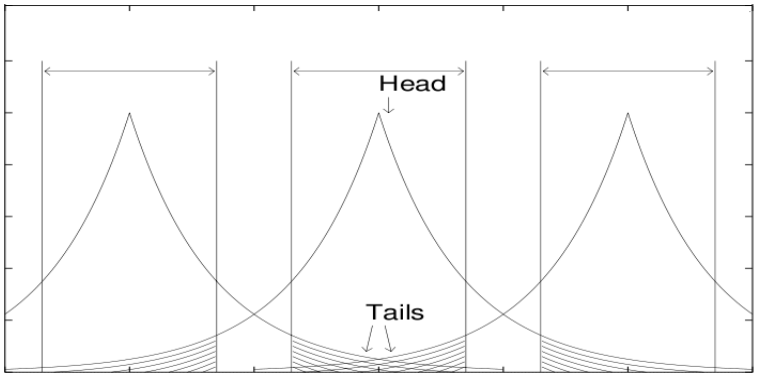

Figure 2.4: The tail cancelation illustration.

illustration is given in figure 2.4. This so called tail cancellation condition directly leads to KKR set of homogeneous linear equations

$$\sum_{RL} \left[B_{R'L',RL}(\kappa) + K \cot \eta_{R'l'}(\varepsilon, \kappa) \delta_{R'R} \delta_{L'L} \right] C_{RL}(\varepsilon) = 0 \tag{2.16}$$

for each R',l'. $C_{RL}(\varepsilon)$ are the eigenvectors and the corresponding energy eigenvalues can be calculated from its nontrivial solutions of equation 12. These can be found from the roots of the secular determinant

$$det|B(\kappa) + \cot \eta_{Rl}(\varepsilon, \kappa)| = 0 \tag{2.17}$$

So in this method, there is an elegant separation of potential and structure dependent parts in the secular equation. But here the structure constant B(κ) are strongly energy dependent and are long range in real space. This increases the computational time immensely. Again finding roots of secular determinant for each energy is computationally very expensive. The MT sphere approximation faces problems when the atoms are displaced from their high symmetric positions.

To remove these short comings of KKR method, a first step in these direction is to intro-

duce the Atomic Sphere Approximation (ASA) and to get the KKR-ASA secular equations which leads to TB-LMTO-ASA method. Introducing ASA with KKR secular equation means, introducing three important points to the KKR secular equation.

(i) Neglecting the non-spherical parts of the potential $V(\mathbf{r})$.

(ii) Neglecting interstitial region (flat potentials).

(iii) Neglect higher partial waves (only s, p, d, f are considered).

In ASA approximation [172, 175, 177], each Wigner-seitz sphere is approximated by atomic spheres which are inflated MT spheres. These atomic spheres should fill the space and hence slightly overlap each other. This overlap is 10% to 14% for Wigner-seitz spheres in the fcc and bcc structure respectively. For non-monoatomic solids, unequal size atomic spheres are required. So for satisfying ASA condition, the sphere should fill the electron containing parts of the space and at the same time these spheres should not overlap more than 30% with any sphere. It works surprisingly well for closed packed structure. But for open structure, introduction of empty spheres which are hypothetical atomic spheres with zero nuclear charge are needed [177].

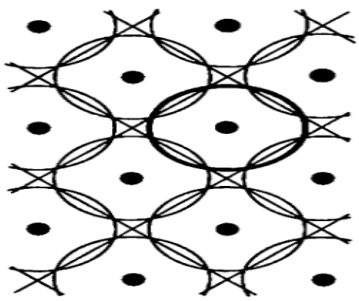

Figure 2.5: Crystal structure with muffin-tin spheres.

Figure 2.5 shows atomic cells, touching muffin tin spheres and one atomic sphere.

Invoking ASA means, instead of integrating out the atomic potential as far as the MT spheres, one can integrate out a more up to the WS sphere. In this process the region of

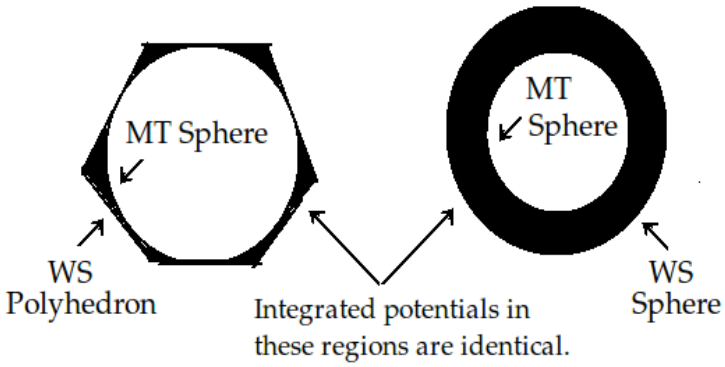

Figure 2.6: Construction of Muffin-tin sphere.

the flat potential V_0 across the annular volume $V_{WS} - V_{MT}$ (i.e. the volume bounded by the WS polyhedron and the inscribed MT spheres are included (figure 2.6).

2.2 KKR-ASA

In KKR secular equation, the structure constant B(K) is energy dependent. By invoking ASA i.e. $\kappa^2 = 0$, to KKR which is nothing but the "zero energy" version of the multiple scattering theory, B(K) becomes energy independent. So here one can define the MTOs in terms of the overlapping WS spheres rather than the touching MT spheres. The wave equation then changes to Laplace's equation whose regular and irregular solutions respectively replace the radial Bessel and Hankel functions. So in KKR-ASA, the equation 2.13 takes the form

$$\chi_{RL}(\varepsilon, \kappa, r_R) = Y_L(\hat{\mathbf{r}}_\mathbf{R}) \begin{cases} \phi_{Rl}(\varepsilon, r_R) + P^0_{Rl}(\varepsilon)(r/S_R), & r_R \leqslant S_R \\ r_R/S_R)^{-l-1}, & r_R > S_R \end{cases}$$

where

$$P^0_{Rl}(\varepsilon) = 2(2l+l)\frac{D_{Rl}(\varepsilon)+l+1}{D_{Rl}-l}$$

is the potential function defined in terms of the logarithmic derivative $D_{Rl} \equiv D\{\phi_{Rl}(\varepsilon, S_R)\}$ of the partial wave $\phi_{Rl}(\varepsilon, r_R)$ at $r_R = S_R$ and $D_{Rl}(\varepsilon)$ is a monotonically decreasing function. After introducing ASA to KKR method, the B(κ) which is energy dependent becomes $S^0_{R'L',RL}$. It is called bare canonical structure matrix which are now energy independent. So by applying the tail cancellation argument, one arrives at the KKR-ASA ($\kappa^2 = 0$) secular equation [177].

$$\sum_{RL}\left[S^0_{R'L',RL} - P^0_{R'l'}(\varepsilon)\delta_{R'R}\delta_{L'L}\right]\left[N^0_{Rl}(\varepsilon)\right]^{-1}C_{RL}(\varepsilon) \tag{2.18}$$

for each R'L'. $[N_R l^0(\varepsilon)]$ is the normalization function.

The corresponding secular equation is

$$det|S^0_{R'L',RL} - P^0_{R'l'}(\varepsilon)\delta_{R'R}\delta_{L'L}| = 0 \tag{2.19}$$

Equation 2.19, exhibits two kinds of terms, potential function $P^0_{R'l'}(\varepsilon)$ and the structure constant $S^0_{R'L',RL}$. Here $P^0_{R'l'}(\varepsilon)$ is a function of energy which depends only on the potential inside the atomic sphere. The structure matrix is a function of Bloch vector $\mathbf{k}$ which depends only on crystal structure but not on lattice constant. The KKR-ASA equations therefore establish the link between the potential and the structure dependent parts of the energy band problem which are otherwise completely decouple within ASA. This KKR-ASA equation provides the connection between $\mathbf{E}$ and $\mathbf{k}$ which is the energy band diagram. Figure 2.7 shows a clear illustration [177]. The main diagonal terms in the canonical structure matrix are equal to 0 whereas the off diagonal terms (hopping integral) depends only on the atomic separation $d = |\mathbf{R}-\mathbf{R}'|$. This canonical structure matrix

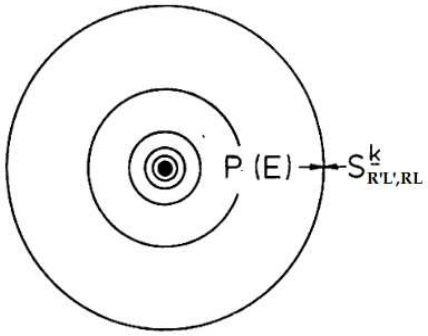

Figure 2.7: Atomis Wigner-sitze sphere.

obeys a long ranged power law decay. From computational point of view, this long range power scaling behavior of MTOs is too slow and at least for s- and p- orbitals (especially for structurally disorder system) and to a less extent for d-orbitals. This makes the real space summation of the MTO tails very difficult. To overcome this difficulty, Andersen [172] proposed the localized or screened MTO basis set.

2.3 The Screening Formalism

The zero energy ($\kappa^2 = 0$) multiple scattering theory or the bare KKR-ASA formalism does not take into account the 'screening' by multipoles at neighboring sites. However, in most systems, be it solids, surfaces or clusters, the process of screening effect is quite natural. Andersen and Jepsen [179] made some transformation in conventional KKR-ASA ($\kappa^2 = 0$) equation which leads to a localized or short ranged MTO. This screening formalism leads to the so called TB-LMTO method [178].

The conventional set of MTO envelop extended in all spaces (designated by the suffix ∞). This can be written as in matrix notation [181].

$$\left|K^0_{RL}\right\rangle^{\infty} = \left|K^0_{RL}\right\rangle - \left|J^0_{RL}\right\rangle S^0_{RL} + \left|K^0_{RL}\right\rangle^{i}$$

$|K^0_{RL}\rangle$ is the head part which is vanishing outside the WS sphere under consideration centered at $\mathbf{R}$. Similarly $|J^0_{RL}\rangle$ which appears in the tail expansion vanishes outside the "foregion sphere" (i.e. neighboring WS sphere centered at $\mathbf{R}'$). $|K^0_{RL}\rangle^{\,i}$ is the interstitial contribution which vanishes inside the spheres. ASA is used, where interstitial region is eliminated by inflating the MT spheres. This term is dropped in the present case but it is included for a general MTO basis set. The above envelop function is going to spread not only inside the sphere at $\mathbf{R}$ but also inside all other neighboring spheres $\mathbf{R}'$. The multipole fields at $\mathbf{R}$ may be screened by surrounding it by multipoles at $\mathbf{R}'$, so that a very localized field is obtained. Here one can introduce a general MTO representation, which is characterized by the "screening parameters α" $\{\equiv \alpha_{Rl}\}$. It is chosen to be a diagonal matrix for simplicity. Now the new screened quantities are K^α_{RL}, J^α_{RL} and $S^\alpha_{R'L',RL}$. These are related to the unscreened quantities. First of all the tail function $|J^0_{RL}\rangle$ is modified by mixing an amount of α of the irregular Hankel function K^0, so that the new tail function can be written as

$$J_{RL}(\mathbf{r_R}) = J^0_{RL}(\mathbf{r_R}) - \alpha_{RL} K^0_{RL}(\mathbf{r_R})$$

The screen envelop function $K^\alpha_R L$ has a head proportional to K^0_{RL}. The screen quantity $|K^\alpha_{RL}\rangle^\infty$ will be a superposition of the corresponding unscreened quantity. For this, the screened structure matrix S^α should satisfy the Dyson equation.

$$\begin{aligned} S^\alpha &= S^0(1 + S^\alpha \\ \Rightarrow S^\alpha &= S^0 + S^0 \alpha S^\alpha \\ \Rightarrow S^\alpha &= S^0(1 - \alpha S^0)^{-1} \\ \Rightarrow (S^\alpha)^{-1} &= (S^0)^{-1} - \alpha \end{aligned}$$

Thus the localized envelop function can be constructed for any set of α's for which $(1 - \alpha S^0)$ exists. The tight binding structure constants can be generated directly in real space for each site $\mathbf{R}$, by inverting the positive definite matrix $\alpha_{Rl}^{-1}\delta_{R'R}\delta_{L'L} - S^0_{RL,R'L'}$ for say a cluster of 20 to 40 nearest neighbor $\mathbf{R}'$.

The great advantage of this real space technique is that it can now be applied even for disorder solids or finite size cluster. It has been found by trial and error [180] that the screened structure matrix is exponentially decaying function and for best possible localization, the screening parameters α_L are unique (independent of **R**), i.e., 0.3485, 0.0530, 0.0107 for l = 0, 1, 2 respectively and 0 for $l > 2$. In contrast to the unscreened structure matrix S^0, the localized structure constant S^α is much more rapid with $d = |\mathbf{R} - \mathbf{R}'|$ and extends at most up to two WS spheres. So the Dyson equation can be calculated for each atom **R** on a cluster of only first and 2nd neighbor atoms $\mathbf{R}'$. Similarly the screened potential function $P^\alpha_{Rl}(\varepsilon)$ which are related to the conventional potential functions $P^0_{RL}(\varepsilon)$ via a similar transformation relation as that of S^0. Finally the screened KKR-ASA secular equation is

$$det|S^\alpha_{R'L',RL} - P^\alpha_{R'l'}(\varepsilon)\delta_{R'R}\delta_{L'L}| = 0 \tag{2.20}$$

This is the basic equation that leads to the so called TB-LMTO method.

2.4 Energy Linearization

In the above equation, the secular matrix has a nonlinear energy dependence. So it is very difficult to find out the roots. By invoking ASA, the energy dependence of the structure matrix has been removed (it is the off diagonal part of KKR-ASA matrix). The remaining energy dependence now occurs only along the diagonal of KKR-ASA matrix

and that is through the potential function $P_{Rl}(\varepsilon)$ evaluated at atomic sphere. It is always desirable to somehow bypass the energy dependence in KKR method so that the entire band structure problem can be simplified. To achieve this goal, Andersen [172, 176] expressed the energy dependent solution $\phi_{Rl}(\varepsilon, r)$ of the Schrödinger equation 2.9 within a sphere in terms of a well converged Taylor series about some arbitrary chosen energy $\varepsilon = E_\nu$ at the center of interest. The energy E_ν is chosen suitably as center of the energy window of own interest.

$$\phi_{Rl}(\varepsilon, r_R) = \varphi_{Rl}(r_R) + (\varepsilon - E_\nu)\dot{\varphi}_{Rl} + \Theta(\varepsilon - E_\nu)^2 \tag{2.21}$$

where $\varphi_{Rl}(r_R) \equiv \phi(E_\nu, r_R)$ and $\dot{\varphi}_{Rl} \equiv \frac{\partial\phi(\varepsilon, r_R)}{\partial\varepsilon}|_{\varepsilon=E_\nu}$ are the solution of Shrödinger equation and its derivatives. Truncating the Taylor series (eq. 2.21) after the term linear in energy (2nd term), one gets the linear basis set which describes fairly well the change of the radial wavefunction through out the atomic sphere $(r_R \leq s)$. The general LMTO basis can therefore be written in an energy independent form in matrix notation.

$$|\chi^\alpha\rangle = |\varphi^\alpha\rangle + |\dot{\varphi}^\alpha\rangle\, h^\alpha + |\chi^\alpha\rangle^i \tag{2.22}$$

where the expression for the Harmitial matrix , h^α, can be derived starting from KKR-ASA secular equation 2.18 as,

$$h^\alpha = (C^\alpha - E_\nu) + \sqrt{\Delta^\alpha} S^\alpha \sqrt{\Delta^\alpha} \tag{2.23}$$

$(C^\alpha - E_\nu)$ is diagonal and ensures the boundary condition at sphere under consideration while the 2nd term $\sqrt{\Delta^\alpha} S^\alpha \sqrt{\Delta^\alpha}$ is the off diagonal term which ensures the boundary condition at "foregion sphere". C^α and Δ^α are some standard potential parameters [181] which denotes the band-center parameter and band width parameters respectively. These two parameters can be defined in terms of the slope and amplitude of the potential function

as

$$C^{\alpha} = E_{\nu} - P^{\alpha}/\dot{P}^{\alpha}$$

$$\Delta^{\alpha} = 1/\dot{P}^{\alpha}$$

Finally energy linearization gives the eigenvalue type LMTO secular equation

$$det|H^{(2)}_{RL,R'L'} - E\delta_{RR'}\delta_{LL'}| = 0 \tag{2.24}$$

where the second order effective one-electron LMTO-ASA Hermitian $H^{(2)}$ is given by

$$H^{(2)} \simeq E_{\nu} + h = E_{\nu} + h^{\alpha} + h^{\alpha}O^{\alpha}h^{\alpha} + \dots$$

$$H^{(2)} \simeq H^{(1)} - h^{\alpha}O^{\alpha}h^{\alpha} + h^{\alpha}O^{\alpha}h^{\alpha}O^{\alpha}h^{\alpha} + \dots \tag{2.25}$$

Further simplification may be introduced. An effective two center TB Hamiltonian $H^{(1)}$ may be defined by truncating the series representation (eq. 2.25) of h to first order in h^{α} which gives rise equation 2.23. So the first order Hamiltonian within the ASA can be written as

$$H^{(1)} \simeq E_{\nu} + h^{\alpha} = C^{\alpha} + \sqrt{\Delta^{\alpha}}S^{\alpha}\sqrt{\Delta^{\alpha}} \tag{2.26}$$

This is the two centered TB-LMTO Hamiltonian. Here the potential parameters are in Rydberg. Since S^{α} is short ranged, H^{1} is itself is short ranged (essentially vanished beyond the second nearest neighbor). So for this first order Hamiltonian H^{1} we will get similar type of equation such as equation 2.24 and we can find the corresponding energy eigenvalues. In localized basis such as TB-LMTO basis, the computational effort in calculating Hamiltonian and overlap matrices or the full charge density scales linearly with number of atoms and is independent of number of **k** points [182]. Thus for sufficiently

large number of atoms in the unit cell, the computer time required for TB-LMTO calculation is dominated by matrix diagonalization.

Figures 2.8 and 2.9 show flow charts how the TB-LMTO package runs. Scheme of typical electronic structure calculations in the form of flow chart is shown in figure 2.10.

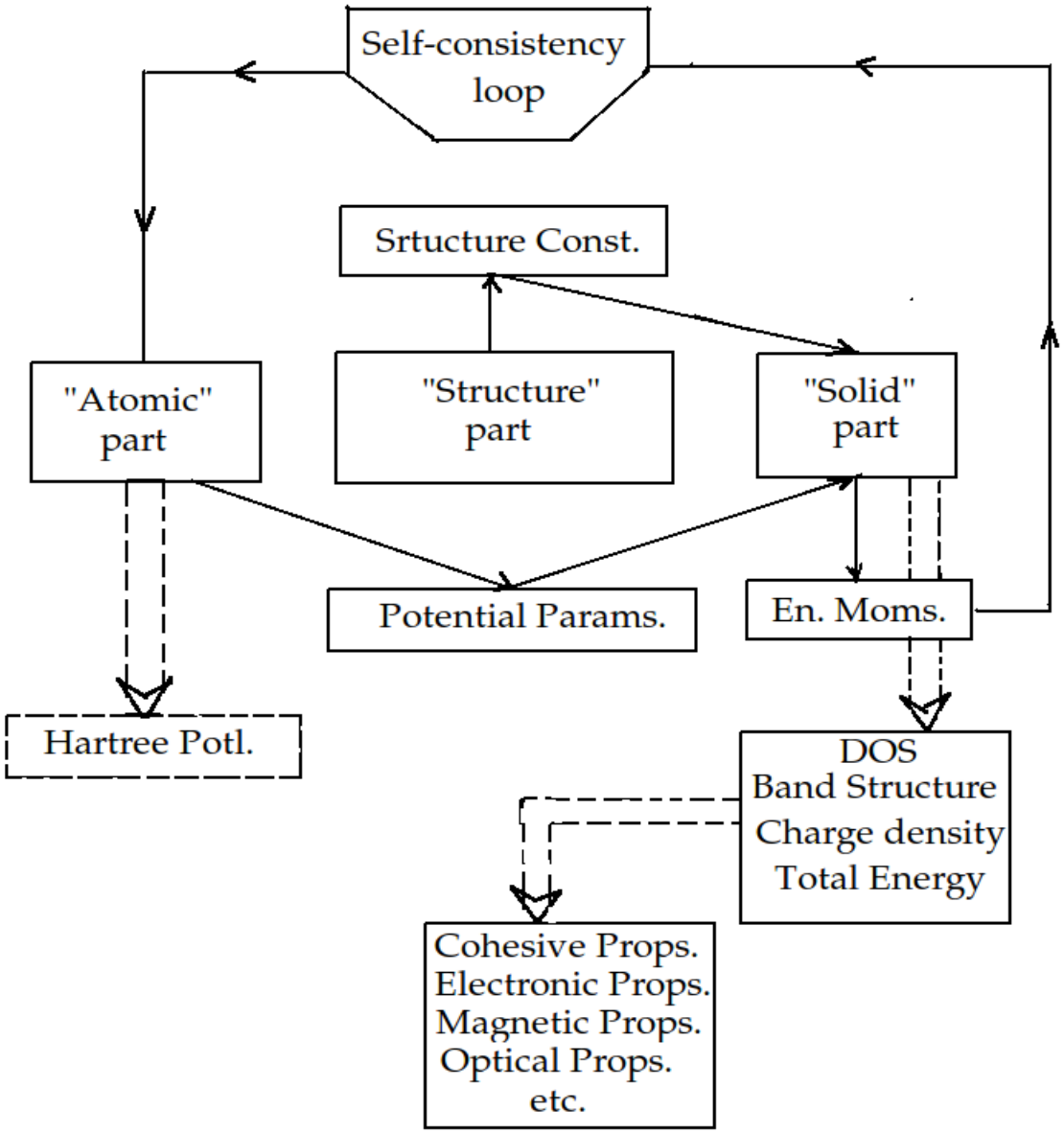

Figure 2.8: TB-LMTO package : Working principle

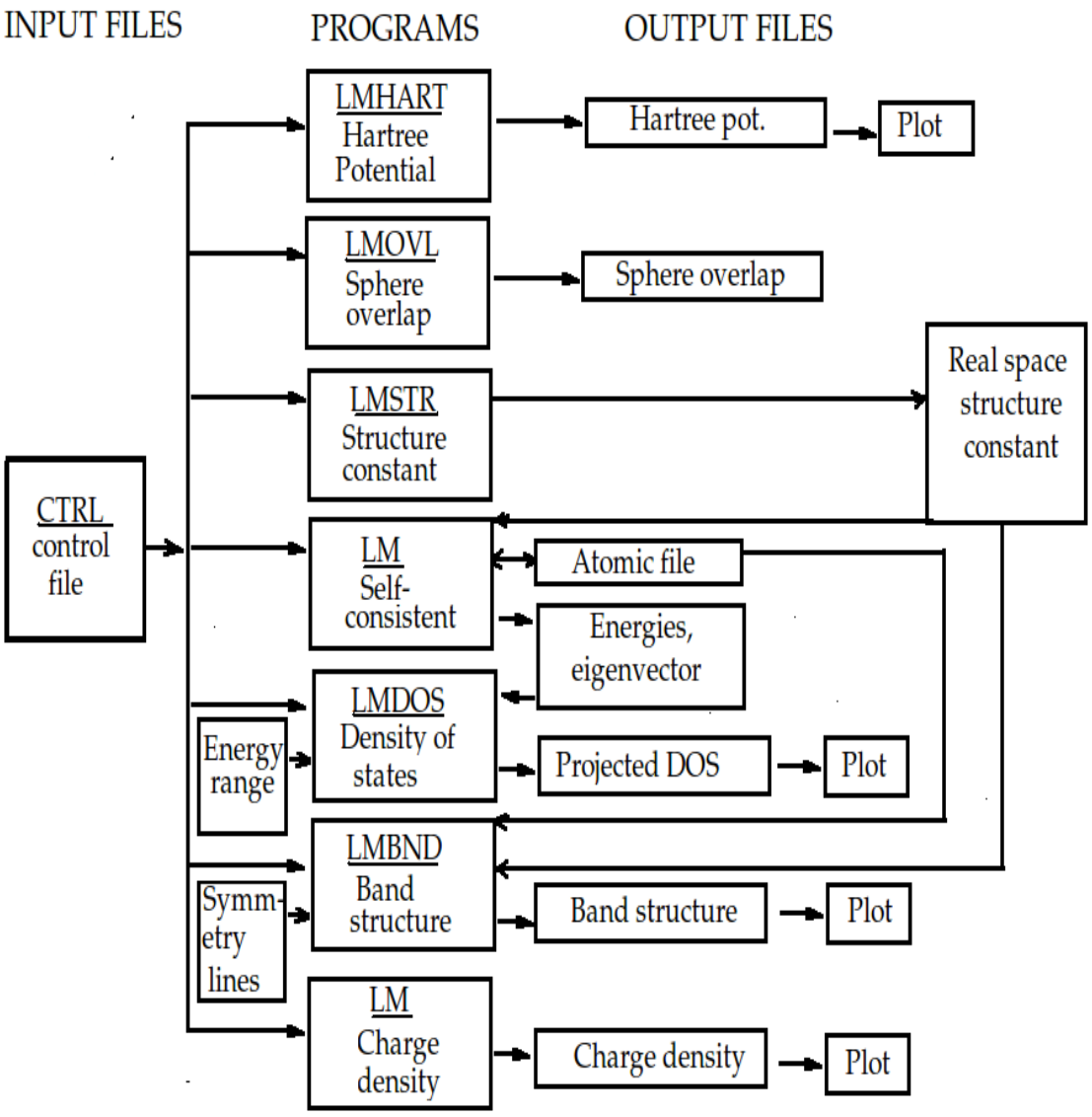

Figure 2.9: Flow chart of TB-LMTO package.

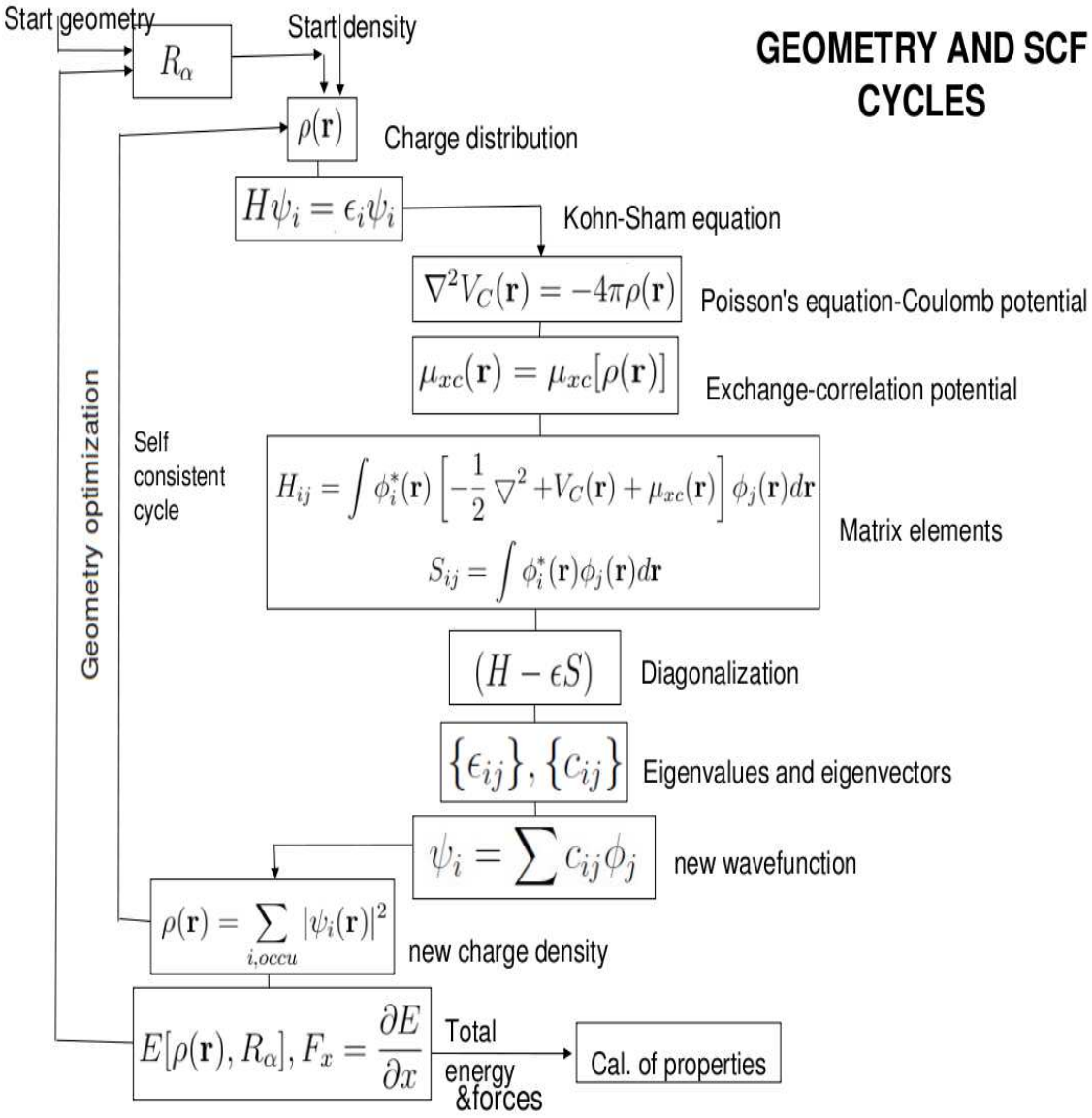

Figure 2.10: Scheme of typical electronic structure calculations.

Chapter 3

Structural and Electronic Properties

3.1 Structural properties

3.1.1 Pure Chalcopyrite Semiconductor

The structure of $A^I - B^{III} - C_2^{VI}$ and $A^{II} - B^{IV} - C_2^V$ groups of chalcopyrite semiconductors is tetragonal. The positions of the various atoms in the tetragonal unit cell are (in Wyckoff notation) : group I/II atom at 4a : 0 0 0; group III/IV atom at 4c : 0.0 0.0 0.5 and group VI/V atom at 8d: u 0.25 0.125, where 'u' is anion displacement parameter. u refers only the x-coordinate of anions for such pure systems, whereas, y- and z-component remain the same as for ideal case. In an ideal zinc-blende structure of binary compound like GaAs each anion has four similar cations as nearest neighbor. So all the four bond lengths are equal and the charge distribution is identical around each bond. Therefore in binary compound, having zinc blende structure, u is 0.25 and $\eta\left(\frac{c}{2a}\right) = 1$. We refer this as ideal case. But in both types of ABC_2 chalcopyrite systems each anion has two group I/II and two group III/IV cations as nearest neighbors as shown in figure 3.1. Figure 3.1

shows one unit cell of a group II-IV-V_2 chalcopyrite lattice. Due to dissimilar atoms as neighbors the anion acquires an equilibrium position closer to one pair of cation than to other. This new position of anion is called anion displacement which is the main cause for bond alternation $(R_{AB} \neq R_{BC})$. We refer this case as non-ideal case $(u \neq 0.25$ and $\eta \neq 1)$. The quantity $u - \frac{1}{4} = (R_{AC}^2 - R_{BC}^2)/a^2$ measures the extent to which the bond alters in a system. Thus the two near-neighbor distances A-C and B-C can be calculated by equation 3.1 and equation 3.2.

$$R_{AC} = a\left[u^2 + \frac{(1+\eta^2)}{16}\right]^{\frac{1}{2}} \tag{3.1}$$

$$R_{BC} = a\left[\left(u - \frac{1}{2}\right)^2 + \frac{(1+\eta^2)}{16}\right]^{\frac{1}{2}} \tag{3.2}$$

The bond alternation gives rise to structure anomalies relative to the ideal zinc blend structure and it has significant effect on band gap.

Chalcopyrite semiconductors, including defect and substituted chalcopyrites, are loosely packed crystals (low packing fraction). Therefore, conventional LMTO-ASA method is not suitable for such systems. To overcome such unfavorable physical situation, it is necessary to introduce empty spheres at appropriate chosen interstitial sites for self consistent calculation. This is indeed possible in the advanced TBLMTO-ASA method. We ensure proper overlap of muffin tin spheres for self consistency and the percentage of overlap is found.

Table 3.1 shows the structural parameters including bond lengths of the systems under study. Obtained lattice parameters are in good agreement with experimental results [3] as well as other computational work [36]. Jaffe and Zunger [36] have calculated 'u' and bond lengths using experimental values of the lattice parameters obtained by Hahn [3] and conservation of tetrahedral bonds (CTB). In CTB, the difference of bond lengths

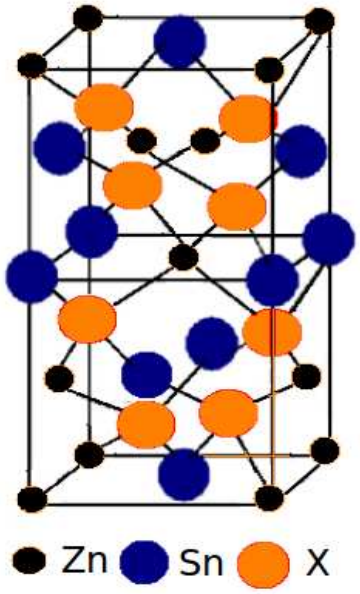

Figure 3.1: One unit cell of the chalcopyrite lattice

($R_{AC} - R_{BC}$) is minimized to find the new values of lattice parameters and u.

We obtain the ground state equilibrium values of lattice parameters, u, η and bond lengths by minimizing the total energy using first principle procedure. Our result shows that u increases from the ideal value for all the three systems, $AgAlM_2$ ($M = S, Se, Te$). But u decreases from the ideal value in the case of $ZnSnX_2$ ($X = P, As, Sb$) and $CuInSe_2$. Jaffe et.al. [36, 38] have shown that the anion shift is the consequence of the atomic sizes i.e. the tetrahedral covalent radii. On the basis of this argument, $Zn - X$ and $Cu - Se$ bonds are shorter compared to $Sn - X$ and $In - Se$ bonds respectively. This is because atomic radii of Zn/Cu are smaller than the group IV/III atoms Sn/In. Our calculated bond lengths for $ZnSnX_2$ ($X = P, As, Sb$), $CuInSe_2$ and $AgAlM_2$ ($M = S, Se, Te$) support this consequence.

We calculate the bulk modulus, 'B' by the slightly modified form of Cohen formula

[1] Solid State Communications 151 (2011) 523-528.

[2] Journal of Alloys and Compounds 512 (2012) 17-22

Table 3.1: Structural parameters of pure chalcopyrite semiconductors. a_{exp}, c_{exp}, u_{exp} are experimental parameters and u_{other}: other calculated parameters.

Systems	a ($\AA$)	c ($\AA$)	a_{exp} ($\AA$)	c_{exp} ($\AA$)	η	u	u_{exp}	u_{other}	R_{AC} ($\AA$)	R_{BC} ($\AA$)
$AgAlS_2$	5.48[1]	10.90	5.72[a]	10.13[a]	0.994	0.265	0.290[a]	0.288[b]	2.42	2.32
$AgAlSe_2$	5.78 [1]	11.52	5.95[a]	10.75[a]	0.996	0.263	0.270[a]	0.287[b]	2.54	2.45
$AgAlTe_2$	6.22 [1]	12.28	6.29[a]	11.83[a]	0.987	0.261	0.260[a]	0.285[b]	2.72	2.64
$CuInSe_2$	5.75[2]	11.61	5.78[c]	11.61[c]	1.010	0.236	0.235[c]	0.237[b]	2.45	2.54
$ZnSnP_2$	5.65	11.30	5.65[d]	11.30[d]	1.000	0.230	0.239[d]	0.236[b]	2.38	2.51
$ZnSnAs_2$	5.85	11.70	5.85[e]	11.70[e]	1.000	0.236	0.231[e]	0.236[b]	2.48	2.58
$ZnSnSb_2$	6.28	12.56	6.27[e]	12.54[e]	1.000	0.235	0.228[e]	0.237[b]	2.66	2.77

[a] Ref.[3],[b] Ref.[36],[c] Ref.[183],[d] Ref.[184],[e] Ref.[185]

given in equation (3.4). The original Cohen's empirical formula [186]

$$B = (1971 - 220\lambda)/d^{3.5} \tag{3.3}$$

is appropriate for zinc blende solids. Due to different ionicity and covalency, λ is chosen to be 0, 1 and 2 for group IV, III-V and II-VI semiconductors respectively. This is because there is increase of ionicity and loss of covalency from the group IV to III-V and II-VI semiconductors. Here 'd' is bond length ($\mathring{A}$). In modified Cohen formula we have considered the average of Bulk modulus corresponding to different tetrahedral bonds. Therefore, it can be written as :

$$B = \frac{1971 - 220\lambda}{4} \sum_{i=1,2,3,4} \frac{1}{d_i^{3.5}} \tag{3.4}$$

where B is in GPa and the nearest-neighbor distances d_i in $\mathring{A}$. The coefficient λ is chosen equal to 1 and 2 for group II-IV-V_2 and I-III-VI_2 respectively. This is because the group III-V and II-VI semiconductors are the binary analogues of group II-IV-V_2 and I-III-VI_2 chalcopyrite semiconductors respectively.

The calculated result shows an inverse proportionality relation between bulk modulus and lattice constant 'a'. This result agrees with the similar study carried out for II-VI type semiconductors [187]. Table 3.2 shows the calculated bulk modulus of the pure chalcopyrite semiconductors. Corresponding experimental and other theoretically calculated bulk moduli are also given in table 3.2 for those systems which are available for comparison. Our result of bulk moduli show good agreement with the other results.

Table 3.2: Bulk modulus B for the pure chalcopyrite systems.

Systems	B (GPa) (Our result).	B (GPa) (Expt.)	B (GPa) (Other theoretical)
$AgAlS_2$	74.96	-	73.19[b], 75.2[c]
$AgAlSe_2$	62.56	-	62.15[b], 62.8 [c]
$AgAlTe_2$	48.67	-	56.02[b], 40.4 [c]
$CuInSe_2$	62.56	62.0[a]	61.42[b], 64.0 [c]
$ZnSnP_2$	77.04	-	75.44[b], 84.2 [d]
$ZnSnAs_2$	68.18	-	67.43[b], 67.0 [d]
$ZnSnSb_2$	53.27	-	-

[a] Ref.[188],[b] Ref.[126],[c] Ref.[189],[d] Ref.[190]

3.1.2 Defect/ Substitutional Chalcopyrite Semiconductor

In a defect chalcopyrite there is a 50% vacancy in one type of cation compared to pure chalcopyrite. Thus such defect compounds fall under vacancy defect systems. Similar definition has also been used by other authors [191, 192]. When substitution (50%) is introduced in place of one of the cation, there are three types of cations in a unit cell unlike pure and defect chalcopyrites. One unit cell of a defect AB_2C_4 and Li substituted $CuInSe_2$ chalcopyrite are shown in figure 3.2. In pure ABC_2 chalcopyrite, 50% of the A atoms are substituted by different constituent atoms. In both defect and substituted chalcopyrites, the vacancies/ substituted atoms are occupied in such a manner that the crystal maintains periodicity. Therefore, these systems are ordered-defect compounds [191]. There are two A, two vacancy/ substituted, four B and eight C atoms per unit cell. In such systems the positions of the various atoms in the tetragonal unit cell are (in Wyck-

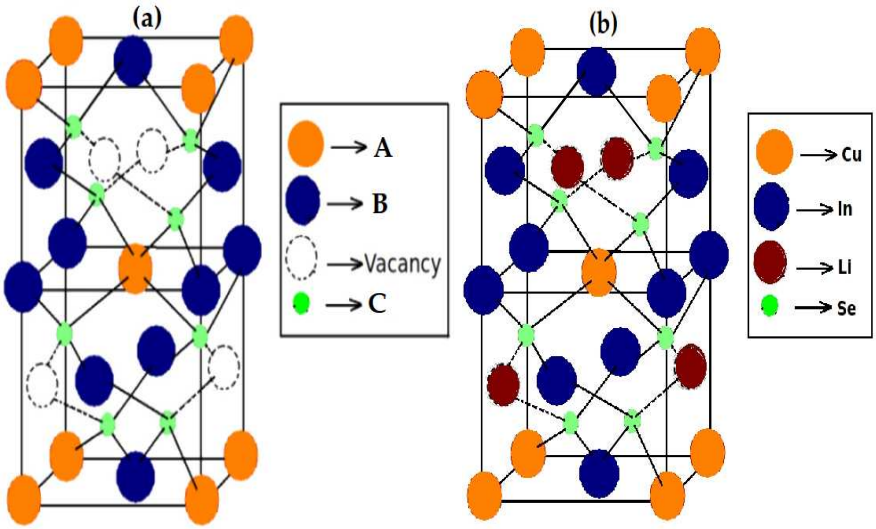

Figure 3.2: One unit cell of (a) defect chalcopyrite semiconductor (b) Li-substituted $CuInSe_2$ chalcopyrite semiconductor.

off notation): A on 2a site (0 0 0), B1 on 2b site (0 0 0.5), B2 on 2d site (0 0.5 0.75), vacancy/ substituted on 2c site (0 0.5 0.25) and C on 8g site (u_x u_y u_z). Here 'u_x', 'u_y' and 'u_z' are anion displacement parameters along three axes. In the case when vacancies are created at the place of B cations, the various positions of atoms in A_2BC_4 are (in Wyckoff notation): A1 on 2a site, A2 on 2d site, B on 2b site, vacancy/ substituted on 2c site and C on 8g site. The space group of the defect and substituted chalcopyrites are $I\bar{4}(S_4^2)$. Unit cell with $\eta = 1$, u_x, u_y and u_z equal to 0.25, 0.25 and 0.125 respectively, is referred as ideal case. Anion shifts along all the three directions in both defect and substituted chalcopyrite, unlike only along x-direction as found in the case of pure chalcopyrites [36]. This is due to the reduction in symmetry in these systems. Therefore, all cations-anion bond lengths are inequivalent in these systems.

Table 3.3 shows the calculated lattice parameters 'a' & 'c', tetragonal distortion, anion

[1] Journal of Solid State Chemistry, 184, Issue 7 (2011) 1614-1621

[2] Journal of Alloys and Compounds 512 (2012) 17-22

[3] Article in book "Crystal Growth and Computational Materials Science : MACMILLAN Advanced

Table 3.3: Calculated structural parameters of defect chalcopyrite semiconductors.

Compounds	a ($\AA$)	c ($\AA$)	η	a_{exp}	c_{exp}	u_x	u_y	u_z	B (GPa)
$AgAl_2Se_4$	5.72[1]	11.31	0.989	-	-	0.262	0.248	0.130	46.87
$CuAl_2Se_4$	5.65[1]	11.28	0.999	-	-	0.271	0.251	0.130	47.98
$CdAl_2Se_4$	5.76[1]	11.49	0.998	5.73[a]	10.60[a]	0.264	0.249	0.132	44.89
$ZnAl_2Se_4$	5.53[1]	10.94	0.990	5.49[a]	10.87[a]	0.266	0.247	0.131	52.06
$CuIn_2Se_4$	5.74[2]	11.64	1.014	-	-	0.251	0.235	0.126	45.44
$CdGa_2S_4$	5.51	10.94	0.992	5.53[b]	10.16[b]	0.270	0.248	0.133	52.48
$CdGa_2Se_4$	5.72	11.41	0.997	5.73[c]	10.70[c]	0.264	0.249	0.133	46.15
$CdGa_2Te_4$	6.18	12.22	0.988	6.11[d]	11.81[d]	0.264	0.251	0.128	36.20
$CdIn_2Te_4$	6.36	12.75	1.002	6.22[e]	12.46 [e]	0.262	0.247	0.131	31.95
$CuIn_2S_4$	5.50	11.14	1.013	-	-	0.252	0.228	0.125	52.84
Cu_2InSe_4	5.70[3]	11.34	0.995	-	-	0.251	0.232	0.128	83.84

[a] Ref.[193],[b] Ref.[72],[c] Ref.[5],[d] Ref.[194],[e] Ref.[82]

Table 3.4: Calculated bond lengths in $\mathring{A}$

Systems	R_{A-C} ($\mathring{A}$)	R_{B1-C} ($\mathring{A}$)	R_{B2-C} ($\mathring{A}$)	$R_{Vacancy-C}$ ($\mathring{A}$)
$CuIn_2S_4$	2.33	2.45	2.46	2.32
$CuIn_2Se_4$	2.45	2.55	2.54	2.43
$CdGa_2S_4$	2.48	2.37	2.40	2.26
$CdGa_2Se_4$	2.57	2.48	2.47	2.37
$CdGa_2Te_4$	2.74	2.63	2.69	2.59
$CdIn_2Te_4$	2.83	2.76	2.76	2.65
	R_{Cu1-Se}	R_{Cu2-Se}	R_{In-Se}	$R_{Vacancy-Se}$
Cu_2InSe_4	2.08	2.06	2.21	2.20

displacement and bulk modulus (B) for a series of group $I-III_2-VI_4$, $II-III_2-VI_4$ and $I_2-III-VI_4$ defect chalcopyrite semiconductors. Calculated structural parameters agree well with the available experimental lattice parameters. The experimental lattice parameters of $AgAl_2Se_4$, $CuAl_2Se_4$, $CuIn_2Se_4$, $CuIn_2S_4$ and Cu_2InSe_4 are not available for comparison. These parameters are also found by energy minimization procedure. We have calculated the bulk modulus 'B' for these systems also using extended Cohen formula [141]. In this formula only three bond lengths are taken into account for calculation because of one vacancy. Here also our result shows an inverse proportionality relation between bulk modulus and lattice constant 'a' as expected. Bond lengths for the above series of defect systems are given in table 3.4 and 3.5.

In all the defect chalcopyrite systems we have found that anion acquires an equilibrium

Research Series", Macmillan Publishers India Ltd., (2012) 250-253

position closer to the vacancy than to the other three cations as expected. We get a different result in case of Cu_2InSe_4. Firstly unlike in other defect systems in this case anion (Se atom) moves towards the Cu atom than the vacancy. Secondly the bulk modulus of this system does not show the inverse proportionality relation with the lattice parameter.

Table 3.5 shows the calculated bond lengths and corresponding covalent and ionic radii of AAl_2Se_4 ($A = Ag, Cu, Cd, Zn$).

Table 3.6 shows the calculated lattice parameters 'a' & 'c', tetragonal distortion, anion displacement and bulk modulus (B) for a series of substituted chalcopyrite semiconductors. Our result of lattice parameters agree well with the available experimental values in the case of $CuLiIn_2Se_4$. Experimental values are not available for other system for comparison. The calculated result shows an inverse proportionality relation between bulk modulus and lattice constant 'a' like pure and defect chalcopyrites.

Bond lengths for the substituted chalcopyrite semiconductors are given in table 3.7.

3.2 Electronic Properties

3.2.1 Band structure & Density of states (DOS)

Band structure, total density of states and partial density of states are plotted to study the detail electronic properties for a series of pure, defect and doped chalcopyrite semiconductors. The Fermi level is set at zero energy in band structure and total DOS plot and marked by dashed horizontal line. In band structure diagram, e, E, E1 and E2 represent

[1]Our work : Journal of Alloys and Compounds 512 (2012) 17-22

[2] SPIE : International Society for Optics and Photonics (accepted 2012-May)

[3] Article in book "Crystal Growth and Computational Materials Science : MACMILLAN Advanced Research Series", Macmillan Publishers India Ltd., (2012) 250-253

Table 3.5: Calculated bond lengths in $\mathring{A}$ for AAl_2Se_4 (A = Ag, Cu, Cd, Zn)

Systems	R_{A-Se} $(\mathring{A})$	R_{Al1-Se} $(\mathring{A})$	R_{Al2-Se} $(\mathring{A})$	$R_{Vacancy-Se}$ $(\mathring{A})$
$AgAl_2Se_4$	2.533	2.468	2.483	2.406
	(2.65)*			
	[2.92]**			
$CuAl_2Se_4$	2.551	2.409	2.481	2.349
	(2.52)*			
	[2.71]**			
$CdAl_2Se_4$	2.583	2.498	2.498	2.396
	(2.64)*			
	[2.93]**			
$ZnAl_2Se_4$	2.467	2.385	2.412	2.288
	(2.42)*			
	[2.72]**			

* Sum of the covalent radii. ** Sum of the ionic radii.

Sum of the covalent radii of Al-Se is 2.41$(\mathring{A})$.

Sum of the ionic radii of Al-Se is 2.37$(\mathring{A})$.

Table 3.6: Structural parameters of a series of substituted chalcopyrite semiconductors.

Compounds	a $(\AA)$	c $(\AA)$	a_{exp} $(\AA)$	c_{exp} $(\AA)$	η	u_x	u_y	u_z	B (GPa)
$CdAgGa_2S_4$	5.64	11.23	-	-	0.995	0.254	0.236	0.125	68.14
$CdAlGa_2S_4$	5.82	11.70	-	-	1.005	0.251	0.248	0.126	60.28
$CuLiIn_2Se_4$	5.84 [1]	11.64	5.85[a]	11.62 [a]	0.996	0.253	0.233	0.127	60.14
$CuNaIn_2S_4$	5.69	11.39	-	-	1.0008	0.244	0.236	0.121	65.83
$ZnOIn_2Te_4$	6.38[2]	12.74	-	-	0.998	0.267	0.215	0.124	-
$ZnMnIn_2Te_4$ [2]	6.33 [2]	12.65	-	-	0.999	0.259	0.245	0.127	-
$Cu_2InAlSe_4$	5.67 [3]	11.36	-	-	1.005	0.247	0.234	0.128	66.33
$Cu_2InGaSe_4$ [3]	5.65[3]	11.39	-	-	1.007	0.236	0.244	0.125	67.20

[a] Ref.[195]

Table 3.7: Bond lengths of the substituted chalcopyrite semiconductors

Systems	Bond Lengths in $\AA$			
$CdAgGa_2S_4$	Cd-S : 2.40	Ag-S : 2.38	Ga1-S : 2.47	Ga2-S : 2.49
$CdAlGa_2S_4$	Cd-S : 2.51	Al-S : 2.50	Ga1-S : 2.53	Ga2-S : 2.54
$CuLiIn_2Se_4$	Cu-Se :2.49	Li-Se : 2.44	In1-Se : 2.58	In2-Se :2.57
$CuNaIn_2S_4$	Cu-S : 2.41	Na-S : 2.37	In1-S : 2.57	In2-S : 2.45
$ZnOIn_2Te_4$	Zn-Te : 2.69	O-Te : 2.58	In1-Te : 2.83	In2-Te : 2.96
$ZnMnIn_2Te_4$	Zn-Te : 2.77	Mn-Te : 2.67	In1-Te : 2.74	In2-Te : 2.77
$Cu_2InAlSe_4$	Cu1-Se : 2.41	Cu2-Se : 2.39	In-Se : 2.54	Al-Se : 2.48
$Cu_2InGaSe_4$	Cu1-Se : 2.38	Cu2-Se : 2.47	In-Se : 2.51	Ga-Se : 2.42

empty spheres of different radii which are introduced at appropriately chosen interstitial sites. The detail electronic properties are studied for the following systems.

I. AgAlM$_2$ (M = S, Se, Te)

(i) $AgAlS_2$: The band structure and total density of states (TDOS) (figure 3.3) show four major subbands of different band widths below fermi level E_F within the energy range 0 to -13.84 eV. The first three subbands having band widths 2.29 eV, 0.91 eV, 3.17 eV respectively below the valence band maxima are separated by very narrow band gaps of 0.22 eV and 0.11 eV respectively. The lowest subband having band width 1.24 eV is

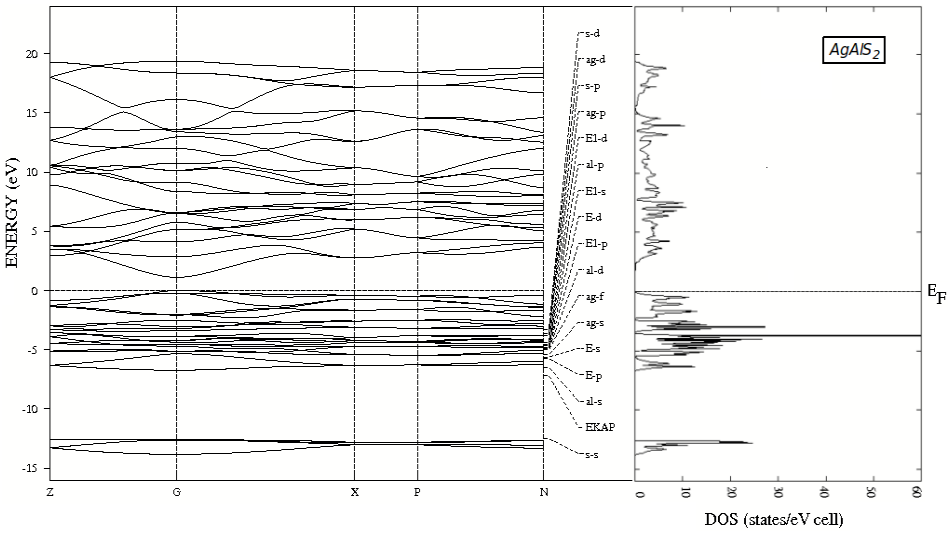

Figure 3.3: Band structure and TDOS for $AgAlS_2$.

formed mainly due to the contribution of Sulfur 3s states. There is a large band gap of $\simeq$ 5.90 eV between the lowest and third subband. Partial density of states (PDOS) for Ag d and S p are plotted in figure 3.4 to study the orbital character and nature of hybridization. These figures show that Ag-d and S-p hybridization contribute to upper valence band

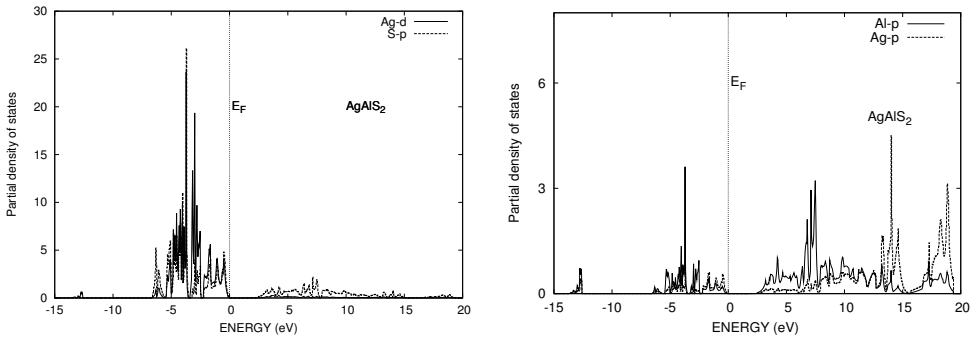

Figure 3.4: PDOS of $AgAlS_2$.

near fermi level. There is a very weak contribution of Ag d states in conduction band. Calculated PDOS for s,p,d states of Ag, Al, S (figure 3.4) show that the contribution to conduction band is due to Ag p, Al p, S d and S p states.

(ii) $AgAlSe_2$: The lowest subband is formed due to Se 4s states within the energy range

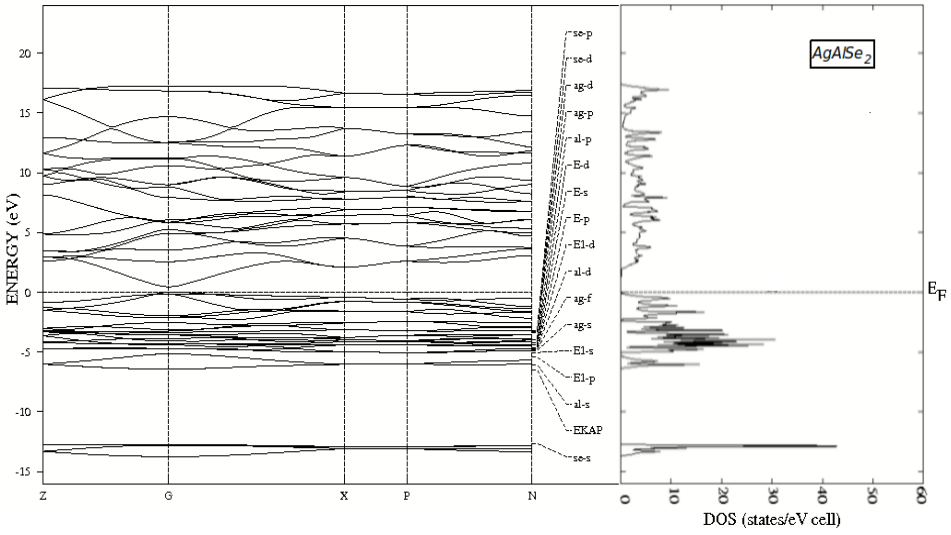

Figure 3.5: Band structure and TDOS for $AgAlSe_2$.

-12.71 to -13.73 eV. There is a large band gap of nearly 6.24 eV between the lowest and just above subband. The second lowest band is mainly formed due to the contribution of Al s and Se p states. Figure 3.5 for band structure and TDOS show four subbands of different band widths below fermi level E_F within the energy range 0 to -13.73 eV.

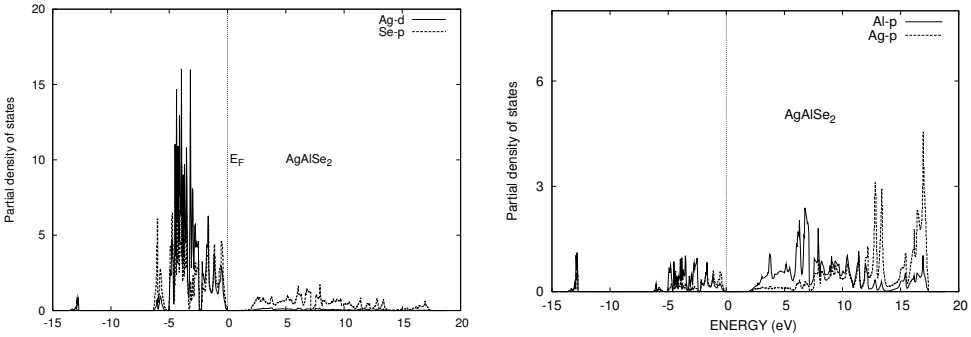

Figure 3.6: PDOS of $AgAlSe_2$.

A very narrow band gap of about 0.36 eV separates the second lowest subband from the third one. The main contribution to the third lowest subband is due to Al p, Se p and Ag d states. The upper most valence band is separated by the previous subband by a band gap of about 0.24 eV. Figure 3.6 for PDOS of Ag d and Se p depicts that all the Ag character is concentrated at the upper valence band leaving a very negligible amount in conduction band. The upper valence band is dominated by Ag d and Se p hybrid character. Figure 3.6 shows that the conduction band has main contribution from Ag p, Al p and Se p and a very less contribution from Ag s and Al s states.

(iii) $AgAlTe_2$: Figure 3.7 shows band structure and TDOS. Unlike the previous two systems this semiconductor has only three major subbands of different band widths below fermi level E_F within the energy range 0 to -12.03 eV.

The upper most valence band is in the region of 0 to -4.63 eV. It mainly consists of Ag d with some contribution from Te p states. There is a very narrow band gap of about 0.48 eV between the upper most valence band and the previous subband.

This second subband is in the region -5.11 to -6.24 eV. It is mainly formed due to the contribution of Al s and less contribution from Te p states. Whereas the lowest or third subband is formed in the region of -11.0 to -12.03 eV due to the contribution of Te 5s

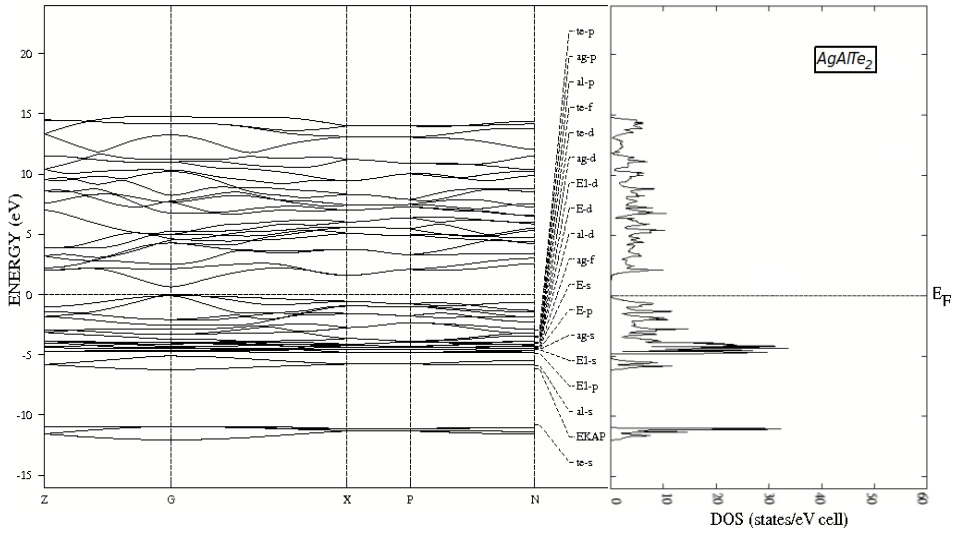

Figure 3.7: Band structure and TDOS for $AgAlTe_2$.

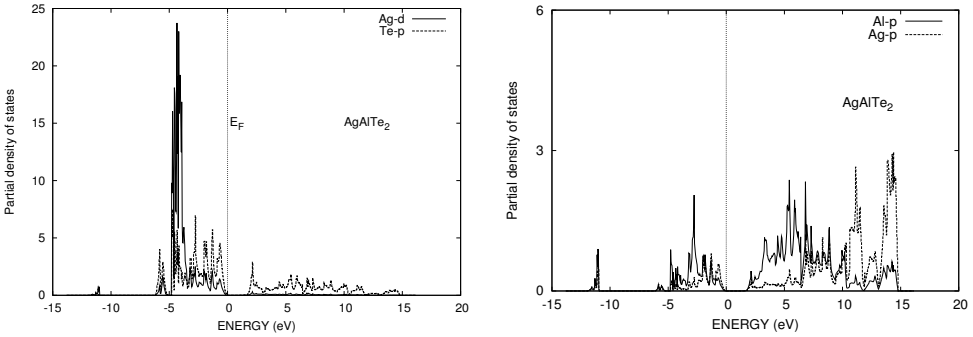

Figure 3.8: PDOS of $AgAlTe_2$.

states. Figure 3.8 shows Ag d character is concentrated in the upper most valence band and a very negligible amount of Ag d character in conduction band. Like in the case of $AgAlSe_2$ the main contribution to upper most valence band is due to Ag d and Te p hybrid orbitals. Figure 3.8 shows that the main contribution to conduction band is from Te p, Ag s/p and Al s/p states.

II. $CuInSe_2$: Figure 3.9 (a) (TDOS) shows four major sub valence bands of different band widths. The first two subbands below the valence band maximum have band widths 1.9 eV and 2.7 eV respectively. They are separated by very narrow band gap of

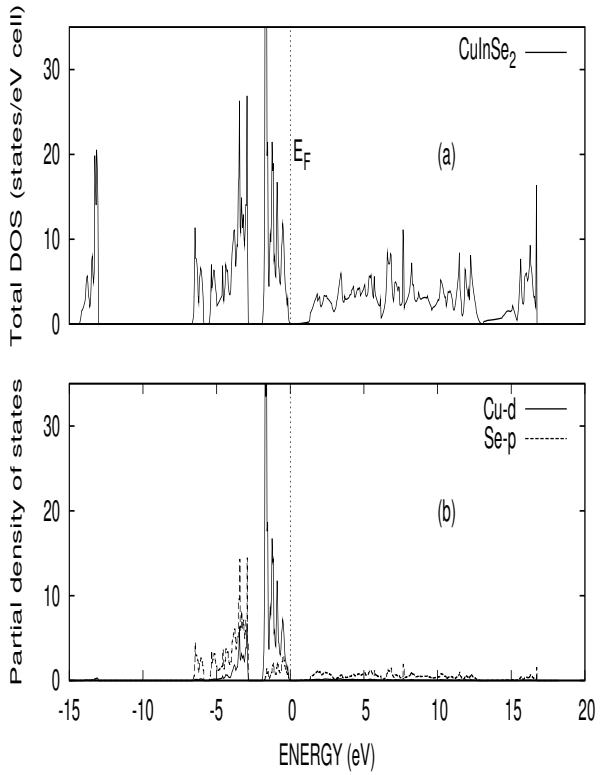

Figure 3.9: $CuInSe_2$: (a) TDOS (b) PDOS.

0.95 eV . The third and fourth subbands have band width 0.8 eV and 1.3 eV respectively. They are separated by a large band gap of 6.4 eV. The second and third subbands are separated by a very narrow band gap of 0.3 eV. The major contribution for the formation of the first subband comes from Cu d orbitals and weak contribution from Se p orbitals. Whereas, it is other way round for the formation of the second subband. Contribution for the formation of the third subband comes from the admixture of In s and Se p orbitals. The lowest subband is Se 4s band. It is clear from the figure 3.9(b) (PDOS) that Cu d and Se p hybridization contribute to upper valence band near Fermi level and there is no contribution of Cu d states to conduction band. The main contribution to the conduction band comes from Cu p, In p and Se p states and very weak contribution from Cu s and In s orbitals. The conduction band width is 16.0 eV. Our band structure result agrees with

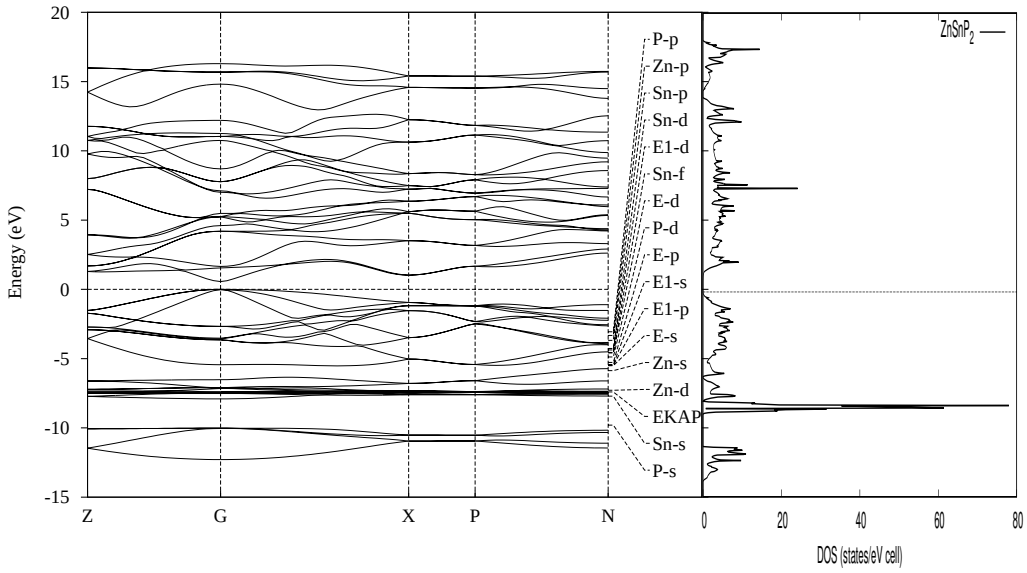

Figure 3.10: Band structure and TDOS for $ZnSnP_2$.

the work of Jaffe and Zunger [36].

III. Z$nSnX_2$ **(X** $= P, As, Sb$**):** Figure 3.10 (Band structure and TDOS) shows that

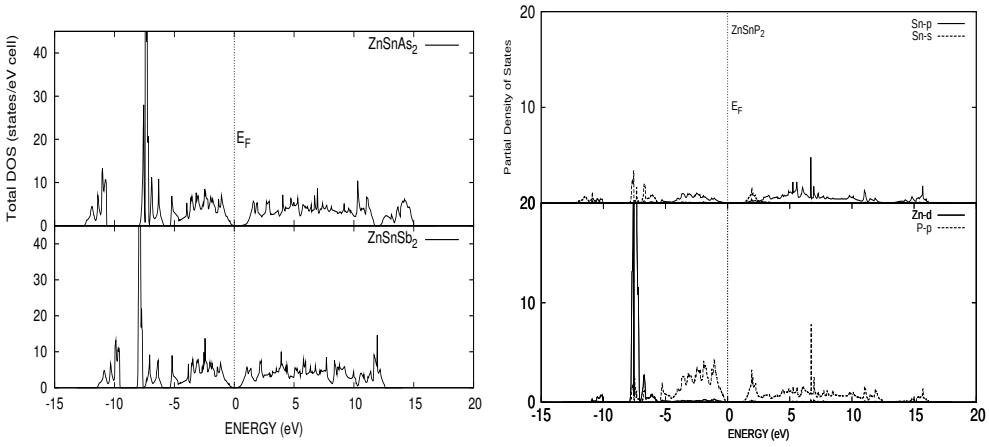

Figure 3.11: TDOS (left panel) of $ZnSnAs_2$ and $ZnSnSb_2$. PDOS (right panel) for $ZnSnP_2$

$ZnSnP_2$ has four main subvalence bands between valence band maxima (E_{VBM}) and -12.2 eV. Figure 3.11 (left panel - TDOS) shows that $ZnSnX_2$ ($X = As$ and Sb) have

four main subvalence bands in the region E_{VBM} and -13.0 eV and E_{VBM} and -11.57 eV respectively. The band width of the upper most valence band for the three systems $ZnSnX_2$ (P, As, Sb) are respectively 5.5, 5.35 and 5.35 eV. Figure 3.11 (right panel - PDOS) for $ZnSnP_2$ and Figure 3.12 (PDOS) for other two systems show that the upper most subband is formed mainly due to the contribution of the admixture of group V anion p states (P p, As p and Sb p respectively), Zn s, Zn p and Sn p states in all the three systems. It is separated by a heteropolar gap from the subband that lies below it. This heteropolar band gap for all these three systems are 0.17, 0.52 and 0.70 eV respectively.

The second sub-valence band consists of mainly anion p and Sn s states. This gives

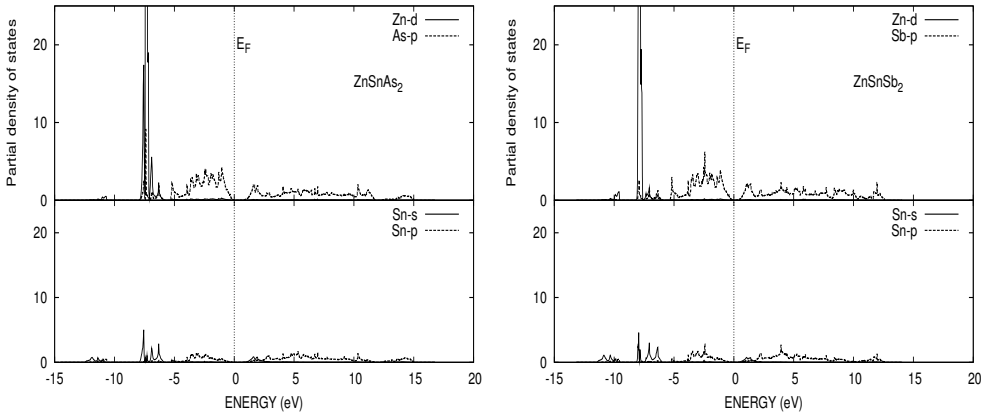

Figure 3.12: PDOS for (left panel) $ZnSnAs_2$ and (right panel) $ZnSnSb_2$.

rise to a strong overlap of the Sn s orbitals with the P p or Sb p orbitals in the case of $ZnSnP_2$ and $ZnSnSb_2$ respectively. As a result the $B^{IV} - C^V$ band (bonding state) is formed. But in the case of $ZnSnAs_2$ As s state also admixed with As p and Sn s states to form the same band. The third subband is the narrow Zn 3d states which touches the bottom of $B^{IV} - C^V$ band. These bands have total band width 2.53 and 2.10 eV respectively in case of $ZnSnP_2$ and $ZnSnSb_2$. But in case of $ZnSnAs_2$, Zn 3d states overlap slightly with $B^{IV} - C^V$ band having band width 2.1 eV. The lowest subband is formed

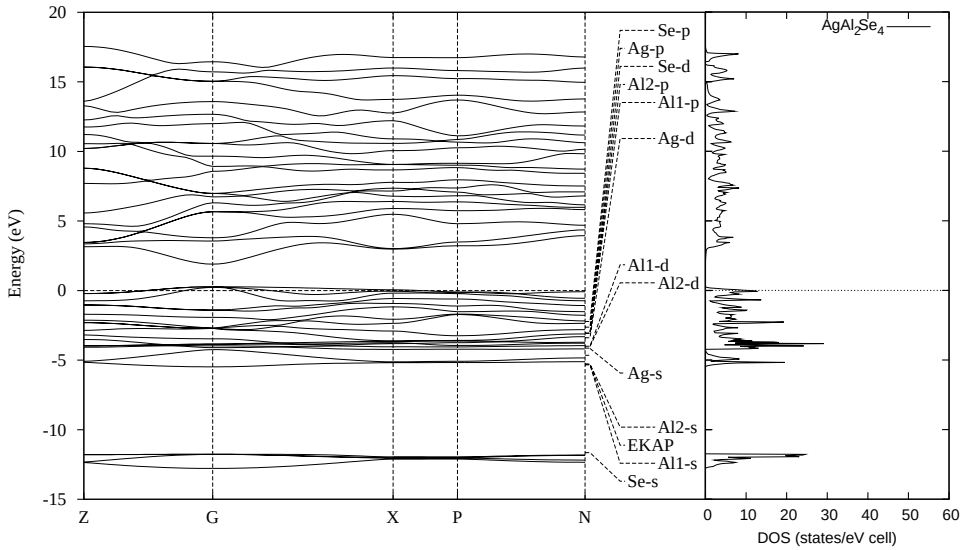

Figure 3.13: Band structure and TDOS for $AgAl_2Se_4$.

by anion s states (P s, As s, Sb s respectively). It is separated from the above subband by heteropolar gap also of 2.1, 2.8 and 1.4 eV for $ZnSnX_2$ ($X = P, As, Sb$) respectively. The band width are 2.27, 1.76 and 1.92 eV respectively.

Figure 3.11 (right panel - PDOS) and 3.12 (PDOS) show that the main contribution to the lower conduction band comes from the admixture of anion (P, As, Sb) s, p states and little Sn s states. Our band structure result for $ZnSnP_2$ agrees well with Jaffe et.al. . But in our case as we have discussed earlier that Zn 3d band touches with $B^{IV} - C^{V}$ band, whereas, Jaffe et.al. found a gap between these two bands. There are no other result available for the other two system for comparison.

IV. $\mathbf{AAl_2Se_4}$ ($\mathbf{A = Ag, Cu, Cd, Zn}$) defect Chalcopyrite Semiconductors

(i) $AgAl_2Se_4$: Figure 3.13 (Band structure and TDOS) shows that this compound is a slightly p-type semiconductor. There are three major sub valence bands of different band

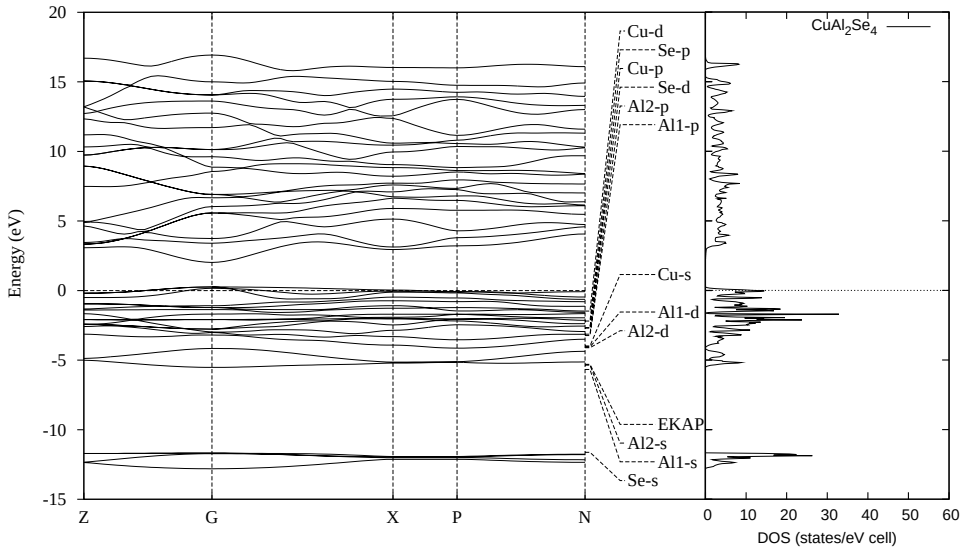

Figure 3.14: Band structure and TDOS for $CuAl_2Se_4$.

widths. The first two subbands of band widths 4.5 and 1.1 eV respectively below the valence band maxima are separated by very narrow band gap of 0.1 eV. The lowest subband having band width 1.0 eV is formed mainly due to the contribution of Se-4s states. There is a large band gap of $\simeq$ 6.2eV between the lowest and second subbands. The second subband is formed due to the admixture of Al s and Se p orbitals.

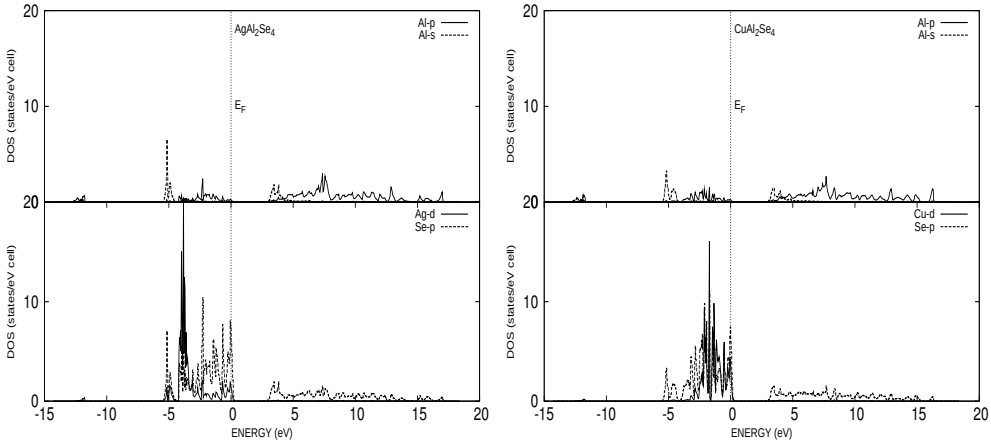

Figure 3.15: PDOS for (left panel)$AgAl_2Se_4$ and (right panel) $CuAl_2Se_4$.

It is clear from the figure 3.15 (left panel) that Ag d and Se p hybridization contributes to upper valence band near fermi level and there is a very weak contribution of Ag d states

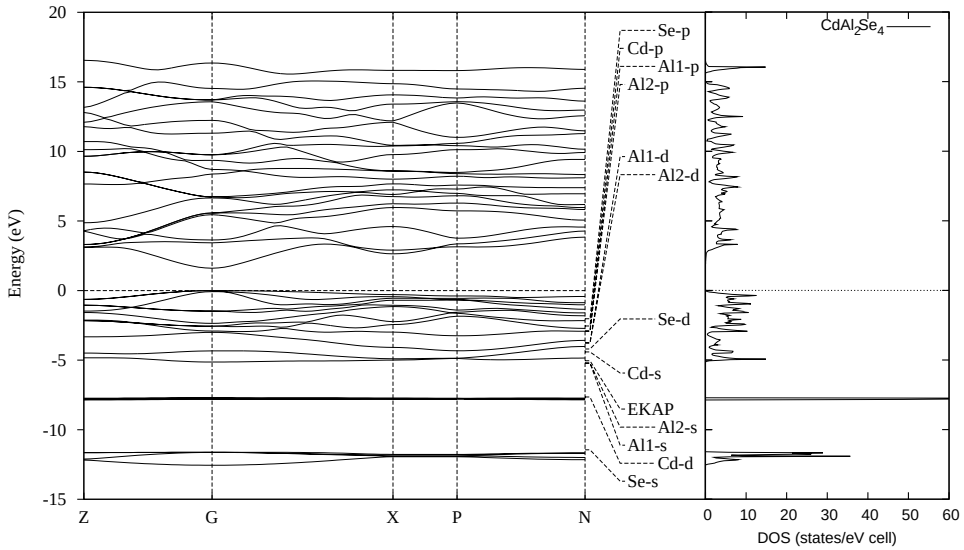

Figure 3.16: Band structure and TDOS for $CdAl_2Se_4$.

to conduction band. The main contribution to conduction band comes from Al p and Se p states and very weak contribution from Al s orbitals. The conduction band width is $\simeq$ 14.4 eV.

(ii) $CuAl_2Se_4$: Like $AgAl_2Se_4$, this compound is also slightly p-type semiconductor. Figure 3.14 (band structure and TDOS) shows three sub valence bands of different band widths. The first two subbands having band widths 4.4 and 1.3 eV respectively are separated by very narrow band gap of 0.1 eV. The lowest subband having band width 1.2 eV is formed due to Se-4s states. There is a large band gap of nearly 6.1 eV between the lowest and just above subband. The second subband is mainly formed due to the admixture of Al s and Se p states. The upper valence band is dominated by Cu d and Se p hybrid orbitals. The conduction band width is approximately 14.0 eV. Figure 3.15 (right panel) shows that Al p and Se p have main contribution to conduction band and Al s state has weak contribution.

(iii) $CdAl_2Se_4$: Unlike $AgAl_2Se_4$ and $CuAl_2Se_4$, this compound does not behave as a

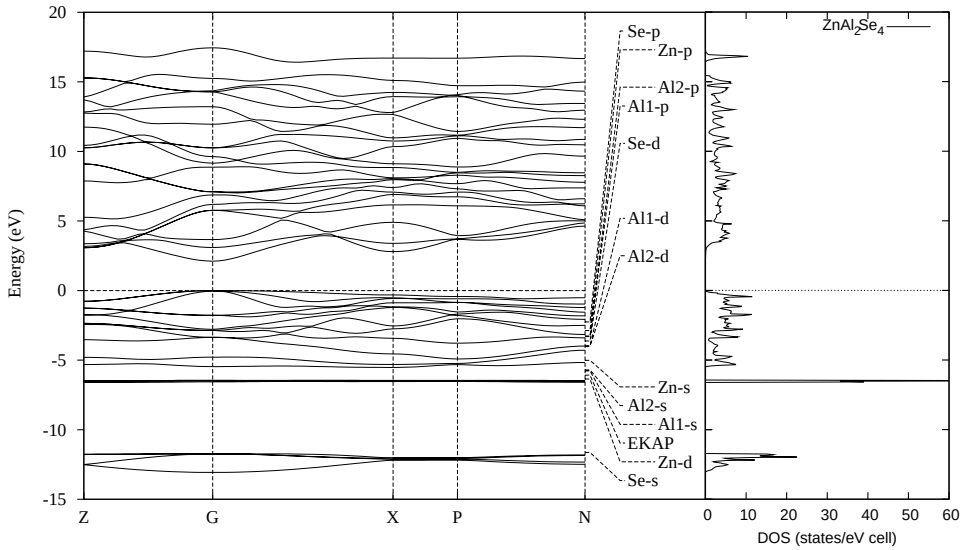

Figure 3.17: Band structure and total DOS for $ZnAl_2Se_4$.

p-type semiconductor. Figure 3.16 (band structure and TDOS) shows three major subvalence bands of different band widths. The two upper most subvalence bands have band widths of 5.1 and 0.2 eV respectively. They are separated by 2.6 eV. The second band is mainly formed due to the contribution of Cd d and very weak contribution from Se p states. The lowest band of band width 0.9 eV is formed due to the contribution of Se 4s states. Figure 3.18 (left panel) shows that the middle valence subband is formed due to the Cd d orbitals. There is no contribution of Cd d orbital to conduction band. Unlike in

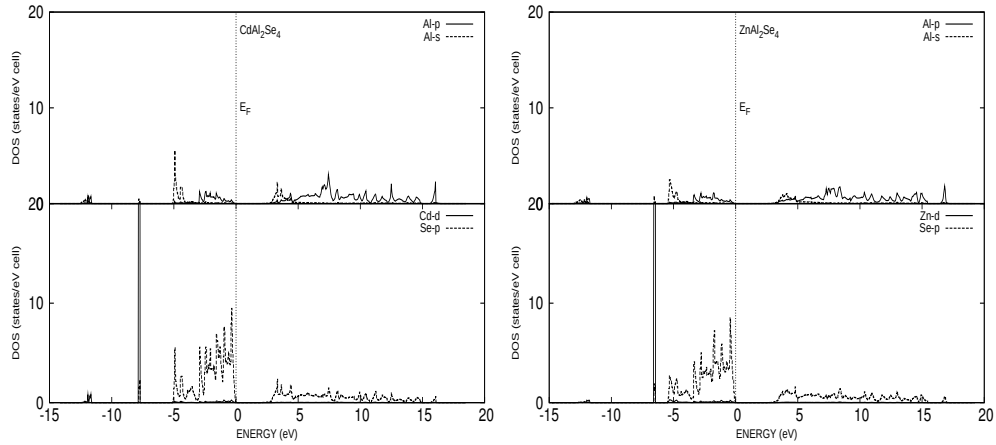

Figure 3.18: PDOS for (left panel) $CuAl_2Se_4$ and (right panel) $ZnAl_2Se_4$.

$AgAl_2Se_4$ and $CuAl_2Se_4$, the main contribution to upper most valence band comes from the admixture of Se p, Al s and very weak contribution from Al p states in this compound. The main contribution to conduction band comes from Se p, Al p states. The conduction band width is found to be 14.0 eV.

(iv) $ZnAl_2Se_4$: Figure 3.17 (band structure and TDOS) show three major sub valence bands. The first two subbands having band widths 5.5 eV and 0.2 eV respectively are separated by band gap of 1.0 eV . The lowest subband having band width 1.3 eV is formed mainly due to the contribution of Se 4s states. There is a large band gap of $\simeq$ 5.1eV between the lowest and the second subband. The second subband is formed due to the contribution of Zn d and there is very weak contribution of Se p orbital. From figure 3.18 (right panel) it is clear that Zn d orbital do not contribute to upper valence band near Fermi level. The contribution to conduction band comes from Al p, Al s and Se p states. The conduction band width is $\simeq$ 14.4 eV.

Among the four AAl_2Se_4 defect chalcopyrite semiconductors, both $AgAl_2Se_4$ and $CuAl_2Se_4$ show p-type character because valency is not maintained by the Se bonds with Ag/Cu and Al. In the pure compounds $AgAlSe_2$ and $CuAlSe_2$, Se makes four bonds, two with Ag/Cu and two with Al. This way valency in these pure chalcopyrites is maintained. Therefore such compounds do not show p-type character [196]. But by creating regular vacancies in place of Ag/Cu in these compounds, one $Se-Ag/Cu$ bond is broken which creates accepter (hole) state.Therefore these compounds show p-type character. In case of $CdAl_2Se_4$ and $ZnAl_2Se_4$, Se makes two bonds with Al and one bond with Cd/Zn. Three bonds are sufficient to maintain valency in these compounds because Cd and Zn are group II elements, whereas in the previous cases Ag and Cu are group I elements [196]. Therefore, these two compounds (Ag and Cu based) do not show p-type character

though there is regular defects in the crystal.

Calculated bond lengths and corresponding covalent and ionic radii are listed in table 3.5. Two different Al-Se bond lengths are corresponding to the two inequivalent sites for Al. We observe that calculated $Ag-Se$, $Al1-Se$ and $Al2-Se$ bond lengths are closer to the sum of the covalent radii rather than the sum of the ionic radii. Similarly in the case of $CuAl_2Se_4$ and $CdAl_2Se_4$ all the three calculated bond lengths are closer to the sum of the covalent radii of the atoms than the sum of the ionic radii. But in the case of $ZnAl_2Se_4$ the bond length of $Al1-Se$ is closer to the sum of the ionic radii of Al and Se than the sum of the covalent radii. This shows that all bonds except $Al1-Se$ for $ZnAl_2Se_4$ are covalent in nature. This little ionicity of $Al1-Se$ bond in $ZnAl_2Se_4$ increases the band gap in comparison to other three compounds. Similar type of discussion may be carried out for other defect chalcopyrite semiconductors.

V. $CuIn_2X_4$ (X = S, Se)

(i) $CuIn_2S_4$:

Figure 3.19 (band structure and TDOS) of $CuIn_2S_4$ shows three subvalence bands of different band widths. Calculated PDOS (figure 3.20 (left panel)) shows that the upper valence band is dominated by Cu d and S p hybrid orbitals. This semiconductor shows p-type conductivity because S p and Cu d hybrid orbitals cross Fermi level. The upper subvalence band is separated from the band, just below it, by a very narrow heteropolar gap. Contribution to the second subband comes from the admixture of In s and S p states. The lowest subvalence band is formed due to the S s states. This subband is separated from its above subvalence band by a wide heteropolar band gap. The main contribution

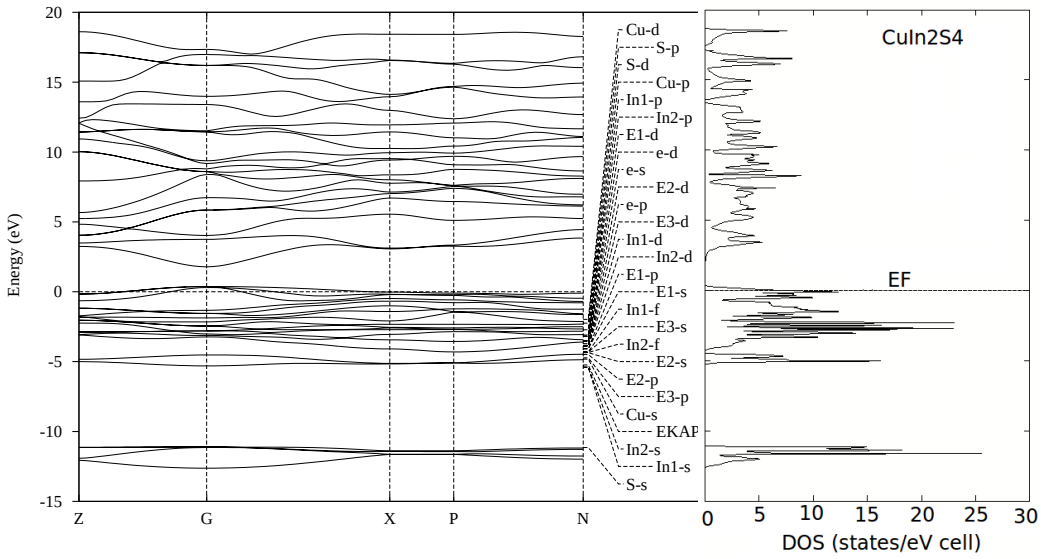

Figure 3.19: Band structure and total DOS for $CuIn_2S_4$.

to lower conduction band comes from In s and S p states. The middle conduction band is formed due to admixture of In p, S p and S d states. The main contribution to the upper conduction band comes from Cu p states.

(ii) $CuIn_2Se_4$:

Unlike $CuInSe_2$, this compound is slightly p-type semiconductor. Figure 3.20 (right panel) shows three sub valence bands of different band widths. The first two subbands have band widths 4.6 eV and 1.0 eV respectively. These bands are separated by a very narrow band gap of 0.4 eV. The lowest subband with band width 1.3 eV is formed due to Se 4s states. There is a large band gap of nearly 6.1 eV between the lowest and second subband. Contribution to the second subband comes from the admixture of In s and Se p states. Figure 3.20 (right panel)-PDOS shows that the upper valence band is dominated by Cu d and Se p hybrid orbitals. This semiconductor shows p-type conductivity because

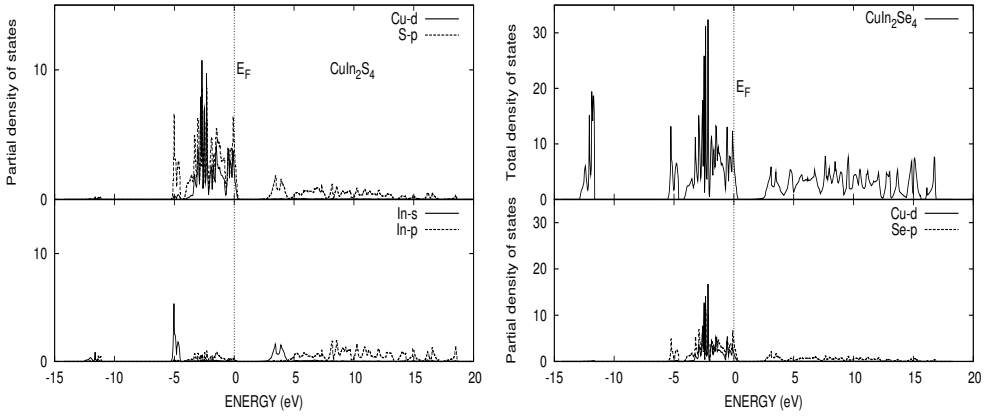

Figure 3.20: (Left panel) PDOS for $CuIn_2S_4$ and (right panel) TDOS & PDOS for $CuIn_2Se_4$.

Se p and Cu d hybrid orbitals cross Fermi level. The conduction band width is approximately 14.9 eV. The main contribution to the conduction band comes from Cu p, In p and Se p states. There is a very weak contribution from Cu s and In s states to conduction band.

VI. Cu_2InSe_4 :

Figure 3.21 (band structure and TDOS) shows that any defect created at 2c site (In atom) affects the density of states near Fermi level. It is clear from figure 3.21 (TDOS) that the Fermi level shifts towards valence band and makes it p-type. This is expected from valency consideration. There is also a significant increase in band gap in this case comparison to $CuInSe_2$. This is expected because In concentration reduces with respect to Cu. Our study shows that Cu d and Se p hybrid orbitals contribute to upper valence band near Fermi level. The contribution to conduction band comes from In p, In s and Se p states. This indicates that defect created in place of group III atom (here 'In') in $I-III-VI_2$ chalcopyrite, affects the conduction band significantly. The conduction

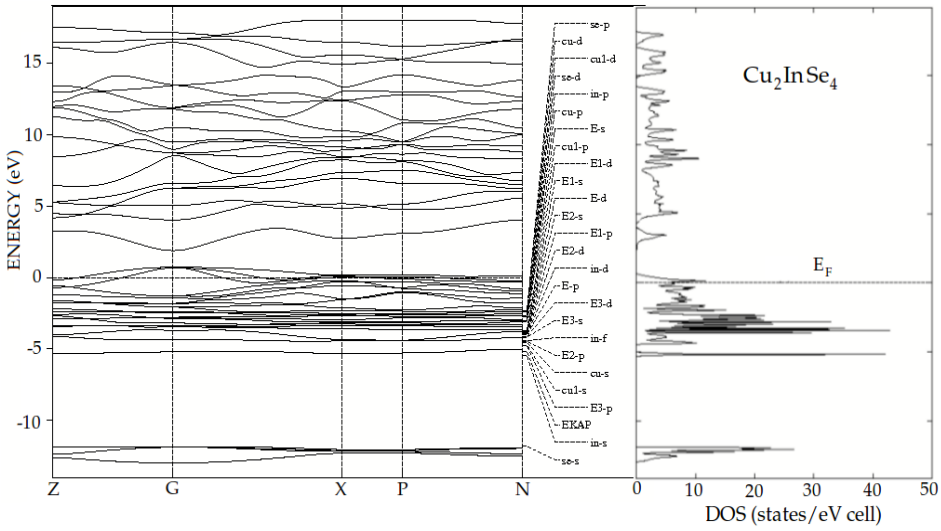

Figure 3.21: Band structure and TDOS for Cu_2InSe_4.

band width is $\simeq$ 8.0 eV.

VII. $CdGa_2X_4$ (X = S, Se, Te):

Figure 3.22 shows that there are four main subvalence bands between valence band maxima (E_{VBM}) and -12.45 eV in case of $CdGa_2S_4$. Figure 3.23 shows that $CdGa_2Se_4$ and $CdGa_2Te_4$ have also four main subvalence bands in the region E_{VBM} and -12.89 eV & E_{VBM} and -11.75 eV respectively. The band widths of the upper most valence bands for the three systems are respectively 4.9, 4.56 and 4.65 eV. Figure 3.23 (PDOS) shows that the upper most subband is formed mainly due to the contribution of the admixture of group VI anion p states (S p, Se p and Te p respectively), Cd s, Cd p and Ga p states in all the three systems. It is separated by a heteropolar gap from the subband that lies below it. This heteropolar band gap for all these three systems are 0.52, 0.35 and 0.52 eV respectively. The second sub-valence band consists of mainly anion p and Ga s states. There is a heteropolar band gap between the second and third sub-valence band. These

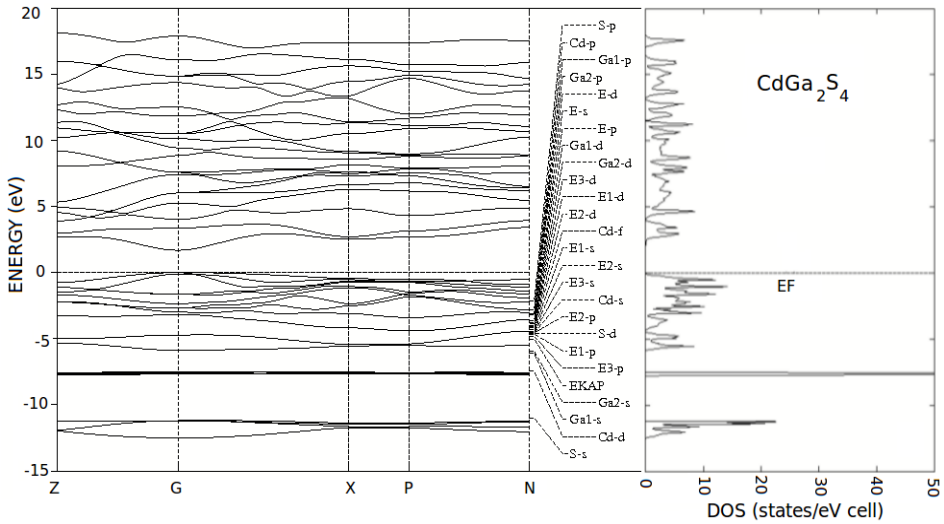

Figure 3.22: Band structure and TDOS of $CdGa_2S_4$.

band gaps are 1.92, 1.75 and 2.1 eV respectively for $CdGa_2X_4$ (X = S, Se, Te). The third subband is the narrow Cd 4d states having band width 0.35, 0.26 and 0.26 eV respectively. The lowest sub-valence band is formed by anion s states (S s, Se s, Te s respectively). It is separated from the above subband by heteropolar band gap of 3.32, 3.58 and 1.57 eV respectively. The lowest sub-valence band width is 1.22 eV for all the three systems. Figure 3.23 (PDOS) shows that the main contribution to the lower conduction band comes from the admixture of anion (S, Se, Te) p states. The middle conduction band is formed due to the admixture of anion p, d & Ga p states. The upper conduction band is formed due to Cd p states. The conduction band widths are 15.57, 14.3 and 12.07 eV respectively.

VIII. $CdIn_2Te_4$:

Figure 3.24 (band structure and TDOS) shows that there are five main sub-valence bands between valence band maxima and -11.4 eV. The band width of the upper valence band is 3.06 eV. Figure 3.25 shows that the upper most subband is formed mainly due to the

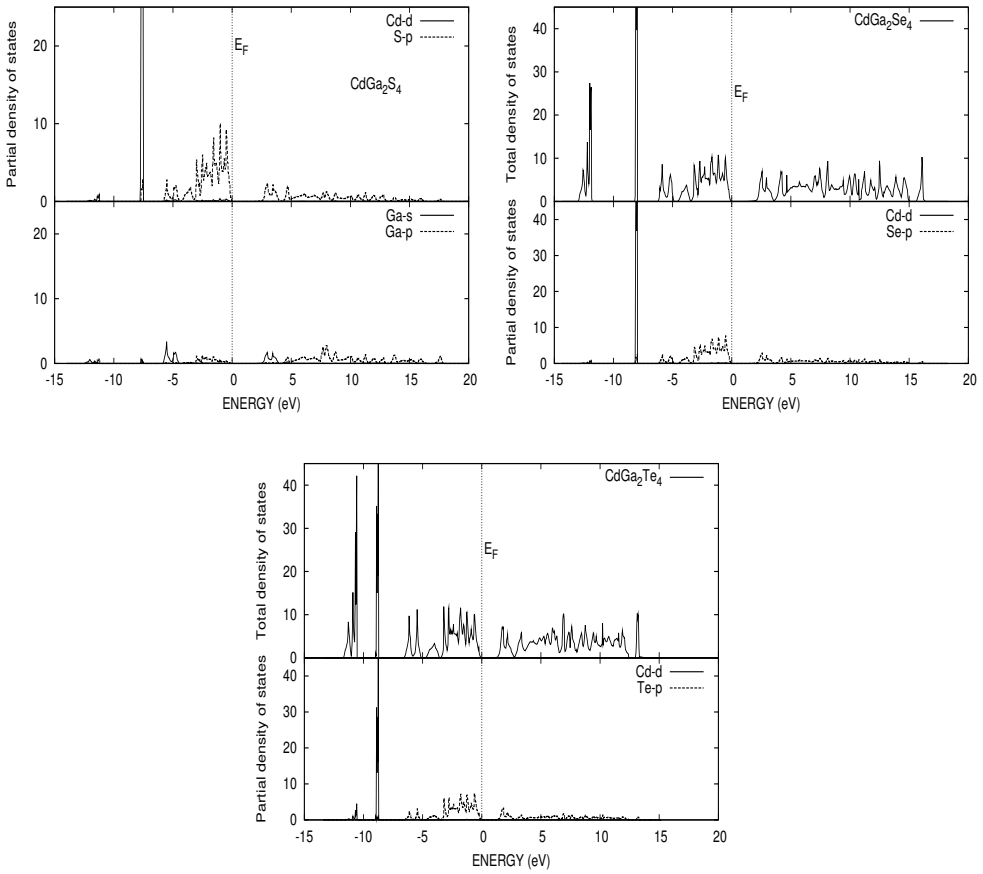

Figure 3.23: (Left panel) PDOS for $CdGa_2S_4$. (Right panel) TDOS and PDOS for $CdGa_2Se_4$. (Bottom panel) TDOS and PDOS for $CdGa_2Te_4$.

contribution of admixture of Te p, Cd p and In p states. It is separated by a narrow heteropolar gap of 0.26 eV from the subband that lies below it. The second sub-valence band consists of mainly Te p and Cd s states. There is a very narrow heteropolar band gap of 0.17 eV between the second and third sub-valence band. The third subband is composed of Te p and In s states. There is a wide band gap of 2.64 eV between third and fourth subbands. The fourth band is composed of very narrow Cd 4d states, having band width 0.26 eV. The lowest subband is formed by Te s states. This subband is separated from the above subband by another heteropolar band gap of 1.59 eV. The lowest sub-valence band width is 1.13 eV. Figure 3.25 shows that the main contribution to the lower conduction

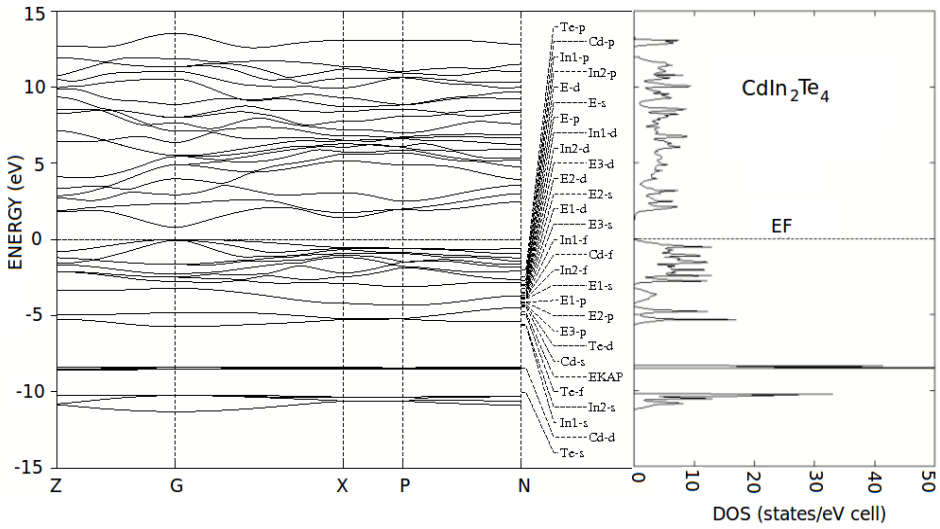

Figure 3.24: Band structure and TDOS for $CdIn_2Te_4$.

band comes from the admixture Te p, In s and Cd s states. The middle conduction band is formed mainly due to Te p states.

The upper conduction band is formed due to the contribution of Cd p states. The con-

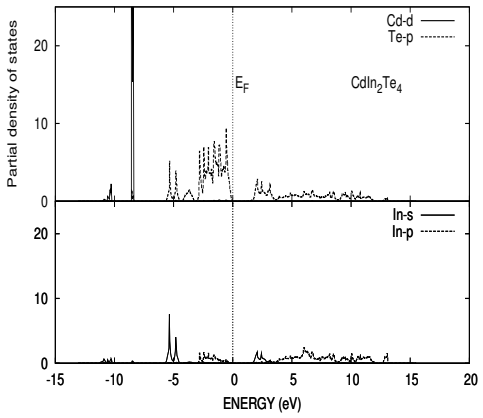

Figure 3.25: PDOS for $CdIn_2Te_4$.

duction band width is 11.72 eV.

IX. CdXGa$_2$S$_4$ (X = Ag, Al) substituted chalcopyrite semiconductor

(i) $CdAgGa_2S_4$:

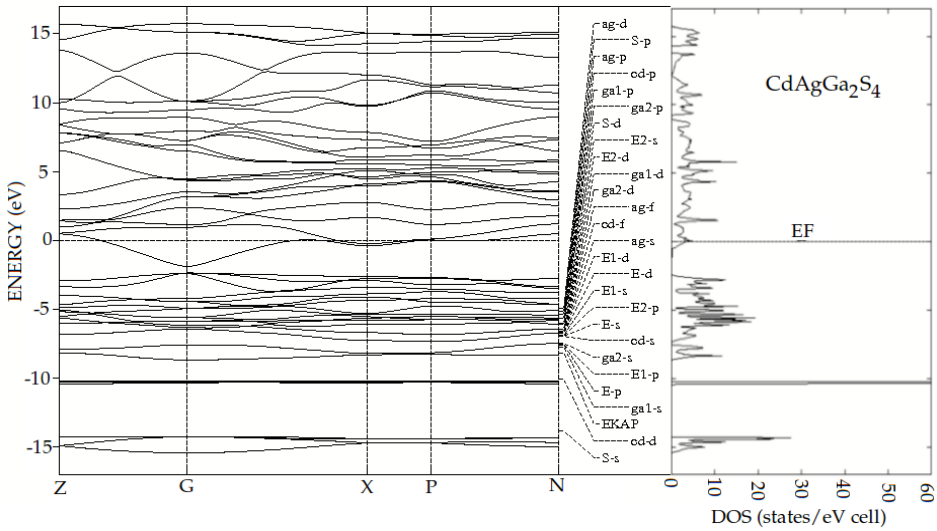

Figure 3.26: Band structure and TDOS of $CdAgGa_2S_4$.

Figure 3.26 (band structure and TDOS) shows four major sub-valence bands. The first two subbands having band widths 4.78 and 1.04 eV respectively are separated by band gap of 0.20 eV. The third subband having band widths 0.20 eV is separated by band gap of 1.45 eV from the second subvalence band. The lowest subband having band width 1.04 eV is formed mainly due to the contribution of S 3s states. There is a large band gap of 3.74 eV between the lowest and the third subband. Figure 3.27 shows that the upper most subvalence band is formed due to the Ag d and S p hybrid states. The second subvalence band consists of the admixture of S p and Ga s states. The third subband is formed due to the contribution of Cd d states and S p orbital. Figure 3.27 (left panel) shows that Cd d orbitals do not contribute to upper valence band. But Ag d orbitals are present in upper valence band. The main contribution to conduction band comes from Ga p, Ga s and S p states. Very weak contribution to the conduction band is found from Cd s and Cd p states. The conduction band width is $\simeq$ 16.43 eV for this system.

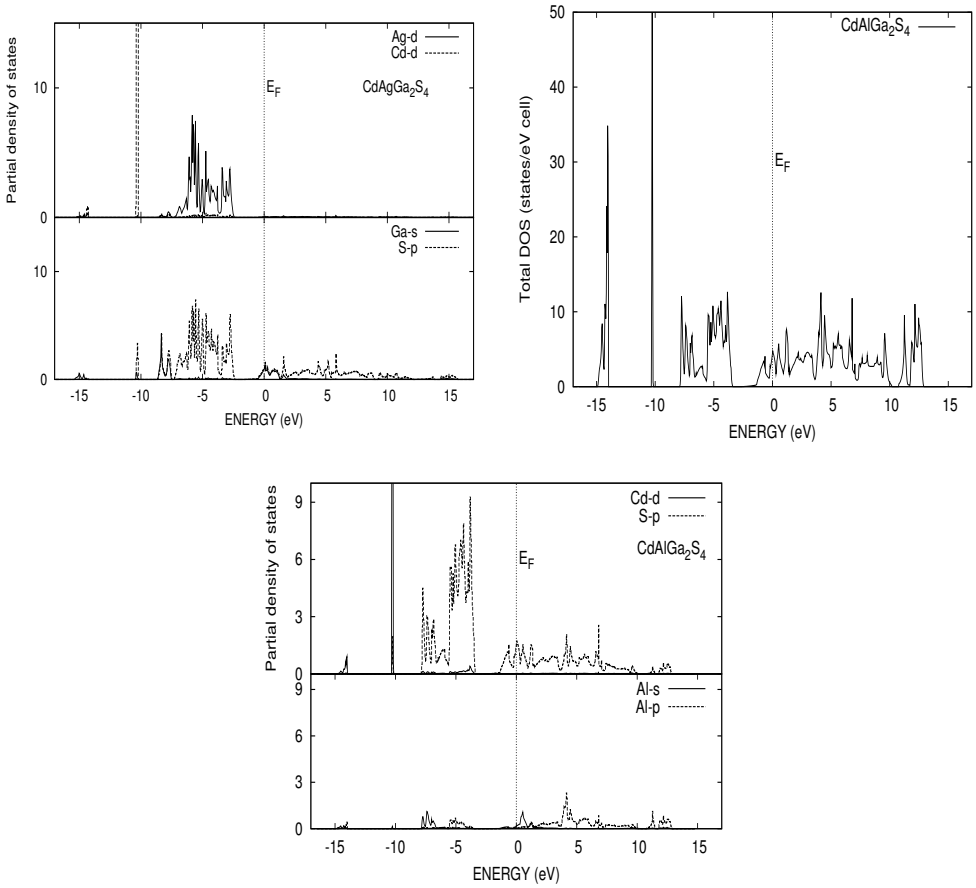

Figure 3.27: (Left panel) PDOS for $CdAgGa_2S_4$. (Right panel) TDOS for $CdAlGa_2S_4$. (Bottom panel) PDOS for $CdAlGa_2S_4$.

(ii)$CdAlGa_2S_4$:

Unlike $CdAgGa_2S_4$, figure 3.27 (right panel - TDOS) shows three major sub-valence bands in this system. The first two subbands having band widths 4.70 and 0.2 eV respectively are separated by band gap of 2.3 eV. The lowest subband having band width 1.0 eV is formed mainly due to the contribution of S 3s states. There is a large band gap of 3.80 eV between the lowest and the second subband. Figure 3.27 (bottom panel) shows that the upper most subband is formed mainly due to S p states. There is also a very weak

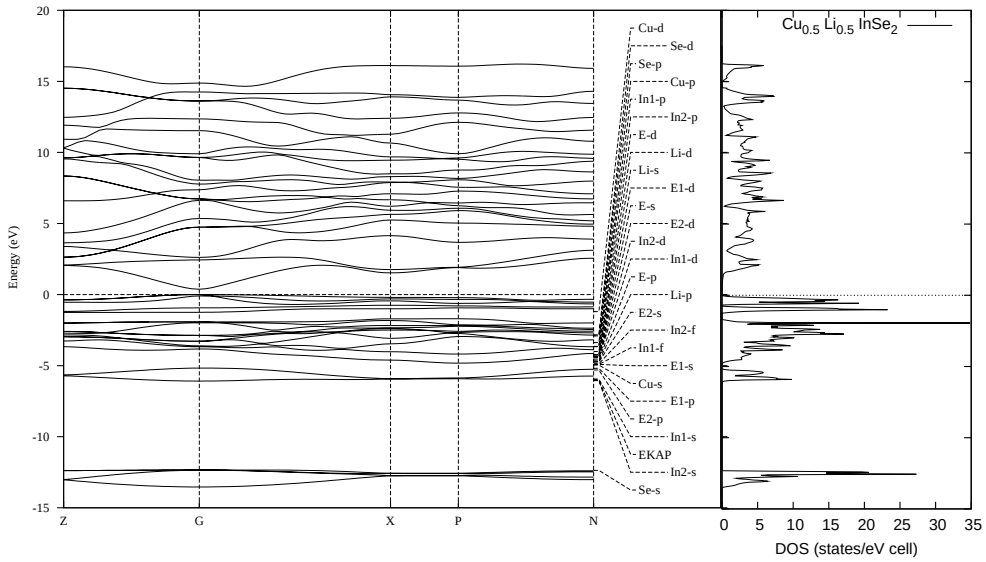

Figure 3.28: Band structure and total TDOS for $Cu_{0.5}Li_{0.5}InSe_2$.

contribution from Cd p, Cd s, Al p and Al s states to the upper valence band. The second subband is formed due to Cd d with little contribution from S p orbitals. Figure 3.27 (bottom panel)) shows that Cd d orbitals do not contribute to upper valence band. The main contribution to conduction band comes from Ga p, Ga s and S p states. Very weak contribution to the conduction band comes from Cd s, Al s, Cd p and Al p states. The conduction band width is $\simeq$ 14.40 eV.

The admixture of S p and Ga s orbitals of lower conduction band crosses the Fermi level and it makes $CdAgGa_2S_4$ n-type semiconductor. Whereas, the admixture of S p, Ga s, Al s and Al p orbitals of the lower conduction band makes $CdAlGa_2S_4$ the n-type semiconductors.

X. $Cu_{0.5}Li_{0.5}InSe_2$

Figure 3.28 (band structure and TDOS) show four major sub-valence bands of differ-

ent band widths. The two upper most sub-valence bands have band widths of 1.2 and 3.1 eV respectively. They are separated by 0.4 eV. Figure 3.29 (left panel) shows that the main contribution to the upper most subband comes from Cu d orbital and very weak contribution comes from Se p orbitals. The second subband is formed mainly due to the contribution of Se p and very weak contribution from Cu d states like in the case of $CuInSe_2$ as discussed earlier. The lowest band of band width 1.2 eV is formed due to the contribution of Se 4s states. The third subband is formed due to the admixture of In s

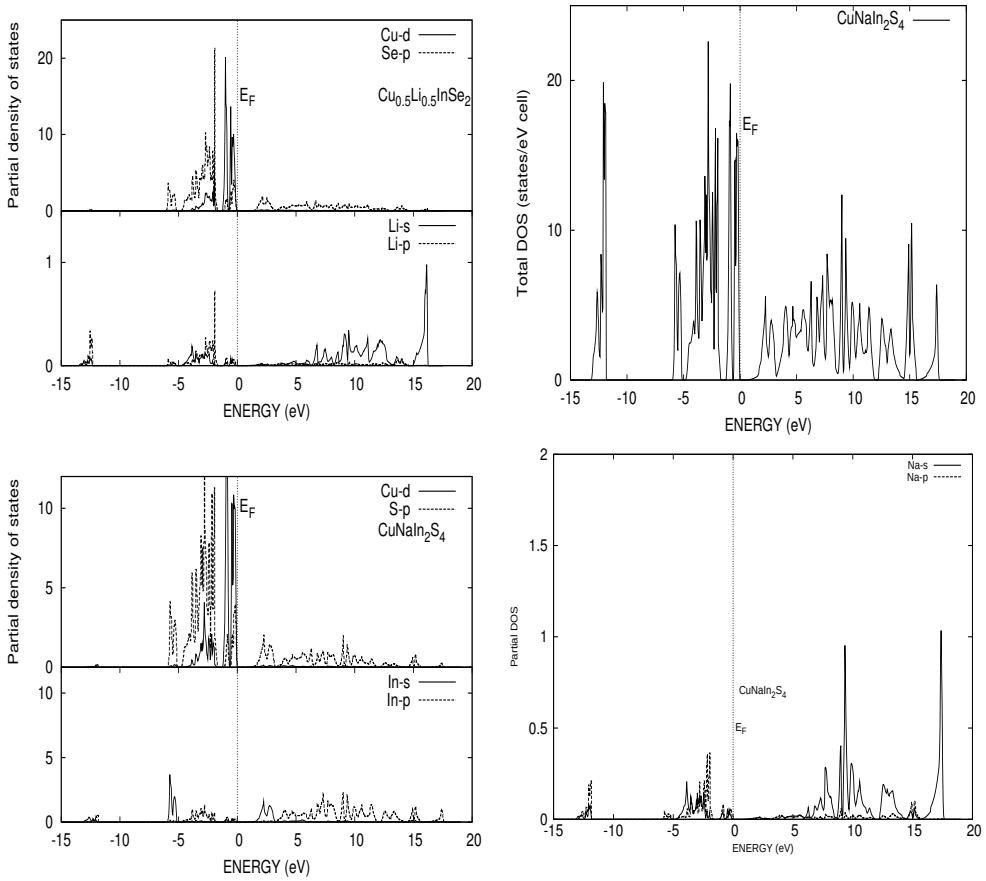

Figure 3.29: (Top-left panel) PDOS for $Cu_{0.5}Li_{0.5}InSe_2$. (top-right panel) TDOS for $CuNaIn_2S_4$. (Bottom-left panel) PDOS for $CuNaIn_2S_4$. (Bottom-righ panel) PDOS of Na s and Na p orbitals for $CuNaIn_2S_4$.

and Se p orbitals. The main contribution to conduction band comes from Cu p, Se p, In p

and very weak contribution comes from In s and Li s orbitals. From figure 3.29 (top-left panel), we find that there is no significant participation of Li-orbitals neither in valence band nor in conduction band. The conduction band width is found to be 15.2 eV for this system.

XI. $CuNaIn_2S_4$:

Figure 3.29 (top-right panel) shows four sub-valence bands of different band widths. Figure 3.29 (bottom-left panel) shows that the main contribution to the upper most subvalence band comes from Cu d orbital and very weak contribution comes from S p orbitals. The second sub-valence band is formed mainly due to the contribution of S p and very weak contribution from Cu d states. The third subband is formed due to the admixture of In s and S p orbitals.The lowest band is formed due to the contribution of S 3s states. The main contribution to conduction band comes from Cu p, S p, In p and very weak contribution comes from In s and Na s orbitals. Figure 3.29 (bottom-right panel), we find that there is no significant participation of Na-orbitals neither in valence band nor in conduction band.

XII. $ZnXIn_2Te_4$ (X = O, Mn)

Figure 3.30 (top-left and bottom panels) show that both $ZnOIn_2Te_4$ and $ZnMnIn_2Te_4$ are n-type semiconductors. Figure 3.30 (top-left panel) shows three subvalence bands for $ZnOIn_2Te_4$. They are separated from each other by heteropolar band gaps. The band width of the upper most sub-valence band, second subband and third subbands are 4.58,

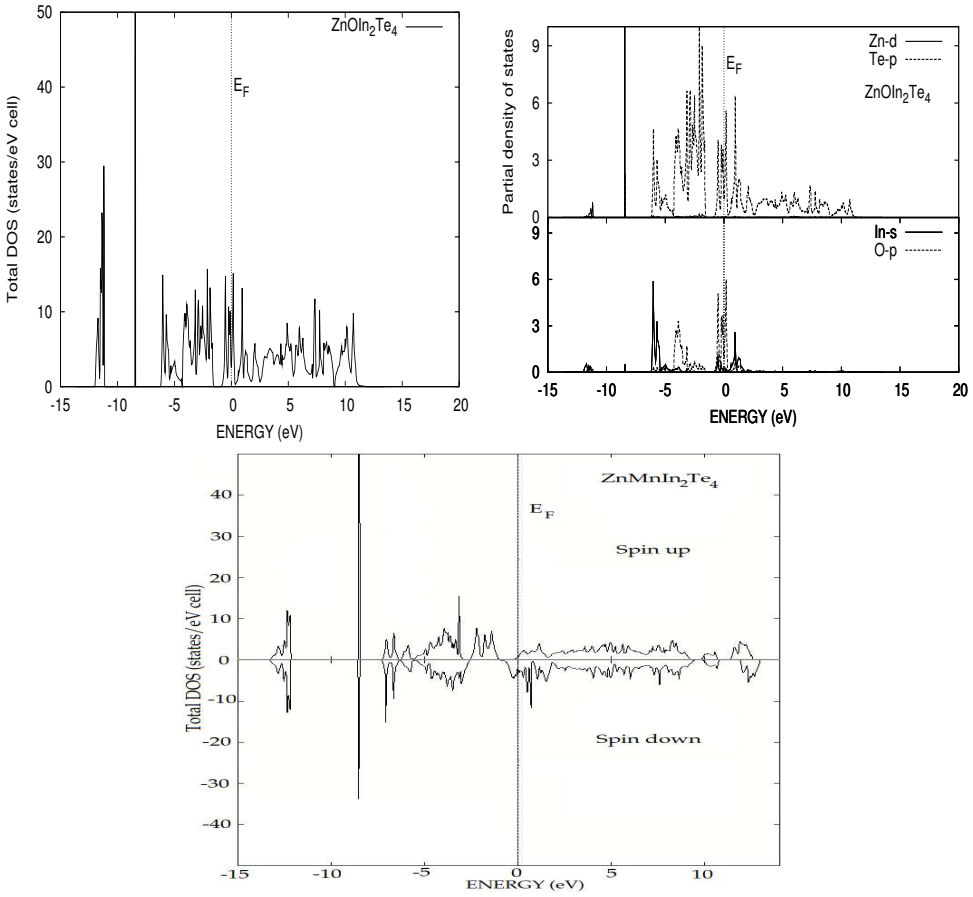

Figure 3.30: (Top-left panel) TDOS of $ZnOIn_2Te_4$. (Right-top) PDOS of Zn d & Te p and In s & O p for $ZnOIn_2Te_4$. (Bottom) TDOS for spin up and spin down states of $ZnMnIn_2Te_4$.

0.16 and 0.91 eV respectively. The upper subband is formed due to the contribution of Te p, O p, In s and In p states with very weak contribution from Zn p and Zn s orbitals. The very narrow second subband is formed by Zn d orbitals. The lowest subband is the Te 5s orbitals. The band gap between the upper most sub-valence and the second sub-valence band is 2.16 eV whereas, between lowest and second subbands is 2.58 eV. Figure 3.30 (top-right panel) shows the admixture of oxygen p, Te p and In s states. There is very weak contribution comes from In p states to the lower conduction band. This copntribution makes this semiconductors n-type. The middle conduction band is formed due to the

admixture of In p, Te p and Zn s states. Contribution to the upper conduction band comes from the Zn p orbitals. The conduction band width is 12.16 eV.

Figure 3.30 (bottom panel) shows that the spin up and spin down DOS are not identical in the case of $ZnMnIn_2Te_4$. These calculations are carried out taking magnetic moment 4.36μB [108]. We calculate the total density of states for the ferromagnetic phase of $ZnMnIn_2Te_4$. This figure shows that there are four and three subvalence bands respectively for spin up and spin down states. The spin down states makes $ZnMnIn_2Te_4$ n-type.

XIII. Cu_2InXSe_4 (X = Al, Ga) chalcopyrite semiconductor :

(i) $Cu_2InAlSe_4$: Figure 3.31 (left panel) shows four sub valence bands.The first two

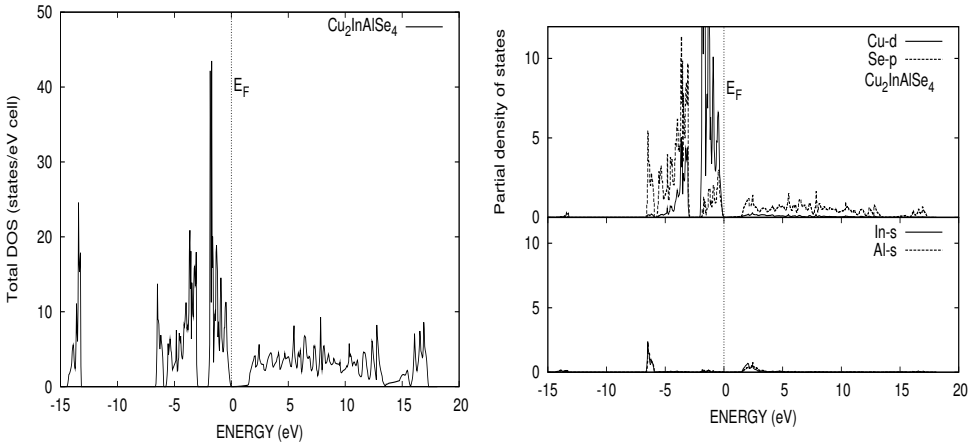

Figure 3.31: $Cu_2InAlSe_4$: (Left panel) TDOS and (Right panel) PDOS.

subbands have band widths 2.00 and 2.80 eV respectively. They are separated by band gap of 0.90 eV. The third subband has band widths 0.80 eV. It is separated by a narrow band gap of 0.20 eV from the second subvalence band. The lowest subband has band width 1.20 eV. It is formed mainly due to the contribution of Se 4s states. There is a wide

band gap of 6.60 eV between the lowest and the third subbands. Figure 3.31 (right panel) shows that the major contribution to the upper most subvalence band comes from Cu d and Se p states. There is very weak contribution of Se d and Cu p states to this subband. The major contribution to the second subvalence band comes from Se p and Cu-d states. There is very weak contribution of Al p and In p to this subband. The third subband is formed due to the admixture of Se p and Al s states. The main contribution to conduction band is due to Al p, Al s, Cu p, In p and Se p states. Very weak contribution to the conduction band is due to Cu s, Se d and In s states. The conduction band width is $\simeq$ 16.00 eV.

(ii) $Cu_2InGaSe_4$: Figure 3.32 (left panel) shows five sub valence bands.The first two sub-

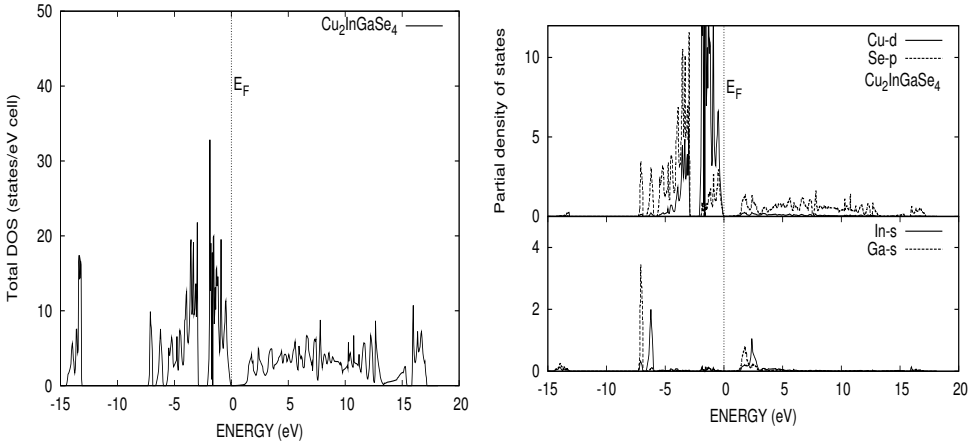

Figure 3.32: $Cu_2InGaSe_4$: (Left panel) TDOS and (Right panel) PDOS.

bands have band widths 2.07 and 2.83 eV respectively. They are separated by a band gap of 0.75 eV. The third subband havs band width 0.75 eV. It is separated by band gap of 0.28 eV from the second subvalence band. The fourth subband of band width 0.37 eV is separated by band gap 0.18 eV from the third subband. The lowest subband has band width 1.32 eV. It is formed mainly due to the contribution of Se 4s states. There is a very wide band gap of 5.84 eV between the lowest and the fourth subband. Figure 3.32 (right

panel) shows that the major contribution to the upper most subvalence band comes form Cu d and Se p states. There is very weak contribution of Se d and Cu p states to this subband. The major contribution to the second subvalence band comes from Se p and Cu d staes. There is very weak contribution of Ga p and In p to this subband. The third subband is formed due to the admixture of Se p and In s states. The fourth subband is formed due to the admixture of Se p and Ga s states. The main contribution to conduction band comes from Ga p, Ga s, Cu p, In p and Se p states. Very weak contribution to the conduction band is due to Cu s, Se d and In s states. The conduction band width is $\simeq$ 16.03 eV.

In all the chalcopyrite semiconductors the valence band maximum (VBM) and conduction band minimum (CBM) are located at the center of Brillouin zone denoted as 'G' (Γ point). This indicates that they are all direct band gap compounds. Our calculated band gaps with the available experimental and other results are listed in table 3.8 for comparison. We mention here others result only for those systems which are available in literature.

It is known that LDA underestimates band gap by 30-50% [204]. If we correct this error, our results are in good agreement with the available experimental band gaps. Jaffe [36] and Pasemann [198] calculated the band gaps of $CuInSe_2$ and $ZnSnP_2$ & $ZnSnAs_2$ respectively. But in case of $CuInSe_2$ [36], their calculated band gap underestimates the experimental result whereas the band gap of $ZnSnP_2$ & $ZnSnAs_2$ [198] overestimates the experimental band gap value. Jiang et.al. [141] have made a correction to LDA using scisser effect for a series of defect chalcopyrites by raising the energy at symmetric points in the band structure. But the correction overestimates the experimental band gaps for $ZnAl_2Se_4$, $CdAl_2Se_4$, $CdGa_2Se_4$,$CdGa_2Te_4$ and $CuIn_2S_4$.

Table 3.8: Energy band gap E_g (eV) of chalcopyrite semiconductors. E_g^{exp} : experimental result, E_g^{other} : other calculation method.

Systems	E_g (eV)	E_g^{exp} (eV)	E_g^{other} (eV)	Systems	E_g (eV)	E_g^{exp} (eV)	E_g^{other} (eV
$AgAlS_2$	1.98	3.13[a]	-	$CdGa_2Se_4$	1.75	2.57[j]	2.76[i]
$AgAlSe_2$	1.59	2.55[a]	-	$CdGa_2Te_4$	1.25	1.50[j]	1.90[i]
$AgAlTe_2$	1.36	2.27[b]	-	$CdIn_2Te_4$	1.03	1.25[j]	1.80[i]
$CuInSe_2$	0.79	1.04[c]	-0.2[d]	$CuIn_2S_4$	1.96$*$	1.53-1.62[j]	1.77
$ZnSnP_2$	1.23	1.47[e]	1.70[f]	Cu_2InSe_4	1.77$*$	-	-
$ZnSnAs_2$	0.68	0.70[g]	0.90[f]	$CdAgGa_2S_4$	0.77$**$	-	-
$ZnSnSb_2$	0.19	0.40[h]	-	$CdAlGa_2S_4$	2.00$**$	-	-
$AgAl_2Se_4$	2.40$*$	-	2.16[i]	$CuLiIn_2Se_4$	1.08	1.50[n]	-
$CuAl_2Se_4$	2.50$*$	2.65-3.02[j]	2.49[i]	$CuNaIn_2S_4$	1.13	-	-
$CdAl_2Se_4$	2.46	3.07[k]	3.54[i]	$ZnOIn_2Te_4$	0.68$**$	-	-
$ZnAl_2Se_4$	2.82	3.52[l]	3.65[i]	$ZnMnIn_2Te_4$	1.3$**$	-	-
$CuIn_2Se_4$	1.50$*$	1.04-1.27[j]	0.50[m]	$Cu_2InAlSe_4$	1.11	1.16[o]	-
$CdGa_2S_4$	2.19	3.25-3.44[j]	3.30[i]	$Cu_2InGaSe_4$	0.79	1.12[p]	-

$*$ p-type direct band gap semiconductors

$**$ n-type direct band gap semiconductor

[a] Ref.[41],[b] Ref.[42],[c] Ref.[2],[d] Ref.[36],[e] Ref.[197], [f] Ref.[198], [g] Ref.[199], [h] Ref.[200], [i] Ref.[141], [j] Ref.[193], [k] Ref.[201], [l] Ref.[33], [m] Ref.[192], [n] Ref.[195], [o] Ref.[202], [p] Ref.[203]

3.2.2 Effect of p-d hybridization

In $A^I B^{III} C_2^{VI}$ ternary chalcopyrite semiconductor, 'A' atoms belong to the group I transition metals like Cu, Ag. Therefore the d orbital of these transition metal also participate in forming valence bands. Partial density of states for all the Cu and Ag based chalcopyrite semiconductors show that the main contribution to upper valence band near Fermi level comes from Cu/Ag d and anion p orbitals. Therefore we expect significant effect of Cu/Ag d & anion p hybridization on the band formation. This effect is small in binary II-VI and III-V compounds where the cation d orbitals (Zn, Cd, Ga, In) are considerably deeper than the anion p orbitals and hence there is strong s-p hybridization in these cases. The detail theory of p-d hybridization is discussed by Jaffe and Zunger [36]. This can be interpreted on the basis of simple molecular orbital considerations. The outer valence p orbitals of anion possess three fold degenerate state, Γ_{15}(p) in a cubic field. The five fold degenerate d orbitals of the cation in a cubic field splits into a three fold degenerate state, Γ_{15}(d) and a two fold degenerate state Γ_{12}(d). The five fold degenerate d orbitals of the cation is separated by an energy $\Delta\epsilon_{pd}$ from the anion p states. The states having same symmetry Γ_{15}(p) and Γ_{15}(d) hybridize. This hybridization forms a lower bonding state and an upper antibonding state. The antibonding state that constitutes the top of the valence band is predominantly formed by higher energy anion p-states and bonding state is constituted by the lower energy cation d-states. Perturbation theory [11] suggests that the two states $\Gamma_{15}(p)$ and Γ_{15}(d) will repel each other by an amount inversely proportional to the energy difference between p and d states ($\Delta\epsilon_{pd}$) and directly proportional to the p-d coupling matrix elements $|\langle p|V|d\rangle|^2$.

In the case of binary semiconductors, since the cation has only deep, core like d states,

therefore, the separation energy $\Delta\epsilon_{pd}$ is large and the p-d coupling matrix element is very small. Therefore, p-d hybridization is negligible.

However, in semiconductor having transition metal as cation, $\Delta\epsilon_{pd}$ is small and there is a reduction in $\Delta E_g^d \approx |\langle p|V|d\rangle|^2/\Delta\epsilon_{pd}$. This is because cation d orbitals are more spread. It has been shown that this also true for non cubic crystal field like chalcopyrite semiconductors under study [36] .

Several studies have been carried to show the p-d hybridization effect on band gap. Jaffe and Zunger [36] have carried out a qualitative study of p-d hybridization effect on band gap. Shay and Kasper [110] have shown that for Cu-based chalcopyrite, the reduction in the band gaps relative to their binary analogous is co-related with the existence of anion p and Cu d hybridization.

In our study we have made an attempt to see the quantitative effect of p-d hybridization in chalcopyrite systems. To carry out such quantitative study we freeze d orbitals and treat these orbitals as core orbitals like in binary semiconductors. Then we compare the band gap of these d frozen systems with the actual d orbital participated chalcopyrite systems as studied in previous subsection. Since there is also an effect of structural distortion, therefore, to see the effect of p-d hybridization alone we consider ideal structure for both the cases, i.e., with and without frozen d orbitals. Partial density of states are plotted to study the orbital character and the nature of hybridization. We summarize the band gaps with and without contribution of d-electrons of group I/II cations in table 3.9.

Table 3.9 shows that there is a significant reduction of band gaps due to p-d hybridization in all the systems.

p-d hybridization not only has a strong effect on band gap reduction; it also strongly affects the electronic structure in general. This is clear from the comparison of fig-

Table 3.9: % of Reduction in band gap(eV) due to hybridization for ideal case.

Systems	With hybridization	Without hybridization	Band gap reduction(%)
$AgAlS_2$	1.70	3.46	51.00
$AgAlSe_2$	1.42	2.67	47.00
$AgAlTe_2$	1.24	2.15	42.00
$CuInSe_2$	0.95	2.35	59.57
$ZnSnP_2$	1.32	1.50	12.00
$ZnSnAs_2$	0.81	0.96	15.62
$ZnSnSb_2$	0.33	0.55	40.00
$AgAl_2Se_4$	2.15	2.67	19.49
$CuAl_2Se_4$	2.44	3.10	21.29
$CdAl_2Se_4$	2.39	2.39	0.00
$ZnAl_2Se_4$	2.58	2.60	0.70
$CuIn_2S_4$	2.0	2.66	39.75
$CuIn_2Se_4$	1.65	2.16	23.61
$CuLiIn_2Se_4$	1.09	2.13	48.82
$CuNaIn_2S_4$	0.83	2.21	62.44

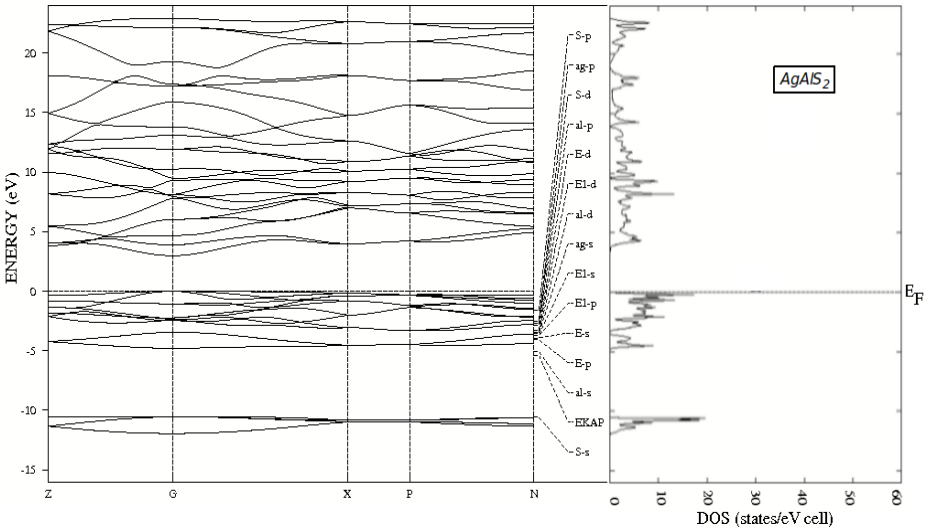

Figure 3.33: Band structure and TDOS of $AgAlS_2$ for ideal and without hybridization case.

ures 3.33- 3.35 (band structure and TDOS) with that of Figures 3.38 (TDOS) for the case of $AgAlM_2$ $(M = S, Se, Te)$.

According to Jaffe et.al. [36] p-d hybridization does not play significant role on band gap anomaly in case of $II - IV - V_2$ chalcopyrite. Here band gap anomaly means difference between the ternary band gap and its analogous binary band gap [36]. They have shown that cation-electronegativity is the dominant factor for band gap anomaly. But our explicit calculation, as shown in table 3.9, shows that there is indeed p-d hybridization effect on band gap reduction in case of $ZnSnX_2$ ($X = P, As, Sb$) which are $II-IV-V_2$ chalcopyrites. This is because these are massive compounds synthesized among all $II - IV - V_2$ semiconductors [70]. They are massive because they are composed of heavy and large atoms. Among them $ZnSnSb_2$ is the most massive compound [70]. Due to large size of atoms the ionicity of the two cations - anion bonds tends to equalize [129]. Therefore these bonds are more covalent. Covalency increases from $ZnSnP_2$ to $ZnSnSb_2$ in this series of compound [206]. Therefore, the band gap reduction is more in $ZnSnSb_2$ due to

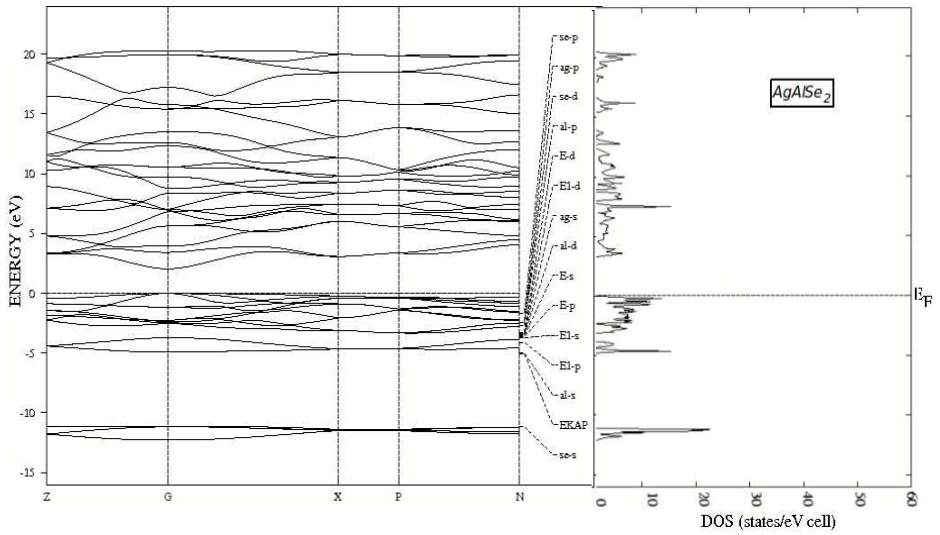

Figure 3.34: Band structure and TDOS of $AgAlSe_2$ for ideal and without hybridization case.

covalent nature of bonding in comparison to other two Zn based chalcopyrite.

Table 3.9 shows reduction in band gap due to p-d hybridization is significant in case of $AgAl_2Se_4$ and $CuAl_2Se_4$ among the series AAl_2Se_4 ($A = Ag, Cu, Cd, Zn$). Figure 3.36 shows TDOS in cases of AAl_2Se_4 for without hybridization case. In the other two cases p-d hybridization is less because Cd/Zn d orbitals do not participate significantly in p-d hybridization. Participation of p-d hybridization is also clear from the figure 3.15 and 3.18 of PDOS.

Table 3.9 shows that band gap reduction in defect system like $AgAl_2Se_4$ or $CuAl_2Se_4$ is less compared to respective pure systems, $AgAlSe_2$ / $CuAlSe_2$. This can be understood from the fact that concentration of Ag/Cu decrease by 50% in defect systems compared to their pure systems. Therefore as discussed earlier, the repulsion between Γ_{15} (p) and Γ_{15} (d) decreases and the antibonding state is depressed downwards leading to an increase in band gap in defect systems.

Table 3.9 also shows that the band gap reduction is more in case of Cu based chalcopyrite

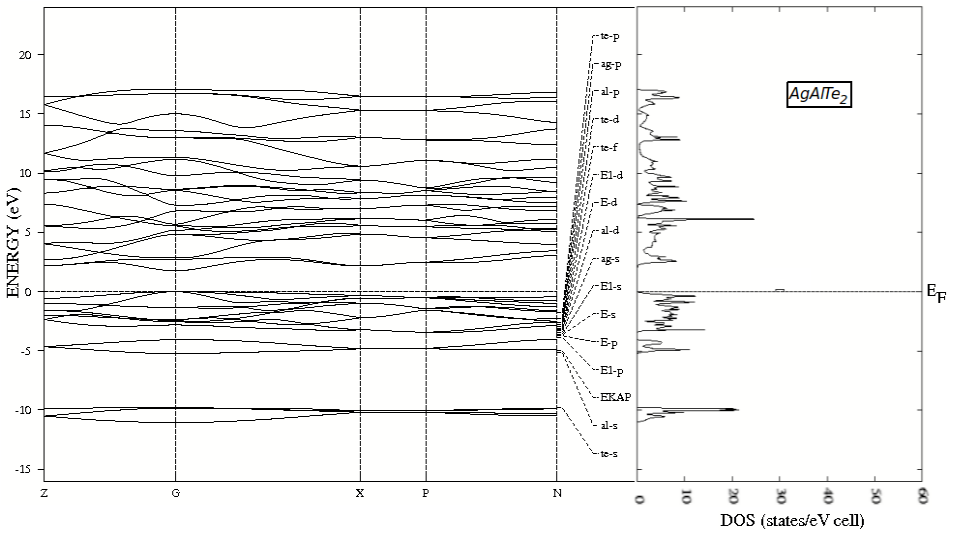

Figure 3.35: Band structure and TDOS of $AgAlTe_2$ for ideal and without hybridization case.

than Ag based.This is because when cation atomic size increases, the band gap always decreases. This is in agreement with other work of Chen [119].

When 50% Cu is substituted by Li the band gap reduction in $CuLiIn_2Se_4$ is less compared to the pure $CuInSe_2$. This is again due to reduction in Cu content and also the reduction in the symmetry of the crystal. Therefore, all the Cu deficient defect chalcopyrites have band gaps greater than that the corresponding pure chalcopyrites. Our result justifies this explanation as it is clear from table 3.8 also.

Though both $CuLiIn_2Se4$ and $CuIn_2Se_4$ have equal concentration of Cu but reduction in band gap is more in the case of Li substituted system. But our previous discussion shows that reduction should be same in these two cases. This difference can be understood from the comparison of figure 3.20 (top-right panel TDOS) and figure 3.29 (TDOS). We find from this comparison that conduction band minimum in the case of Li-substituted compound shifts significantly towards the Fermi level compared to the defect system. This shift is due to the shift of Se p orbitals towards the Fermi level as shown on fig-

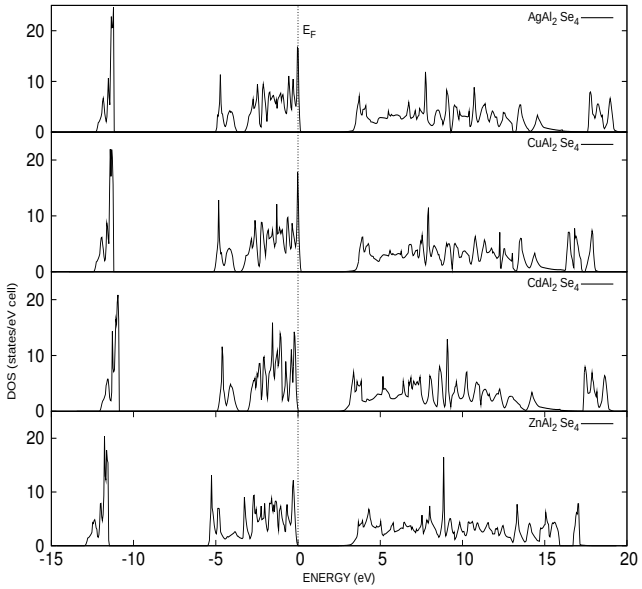

Figure 3.36: TDOS of AAl_2Se_4 (A = Ag, Cu, Cd, Zn) for ideal case without hybridization.

ure 3.20 (top-left). The valence band maximum which lies slightly above the Fermi level in $CuIn_2Se_4$, shifts at the Fermi level in Li-substituted compound. There is very negligible contribution of Li-orbitals to valence and conduction bands. Therefore, we can say Li acts as a catalyst. In $CuInSe_2$ the covalent bonding character of the Cu-Se bonding is dominant. When covalent character dominates, Se p-Cu d hybridization plays a major role. This causes a greater narrowing down of the band gap in the case of $CuInSe_2$ compared to the other two compounds. This is because there are 50% less Cu-Se bonds in defect and Li-substituted $CuInSe_2$. The Li-Se bonding possesses an ionic character because of the large electronegativity difference between Li and Se atoms. This ionic character of bonding increases the band gap in $CuLiIn_2Se_4$ compared to the $CuInSe_2$ chalcopyrite.

In case of defect $CuIn_2S_4$ and Na substituted $CuInS_2$ ($CuNaIn_2S_4$), we observe similar type of results like in case of $CuIn_2Se_4$ and $CuLiIn_2Se_4$. We find significant effect of reduction in band gap in both $CuIn_2S_4$ and $CuNaIn_2S_4$ due to p-d hybridization ef-

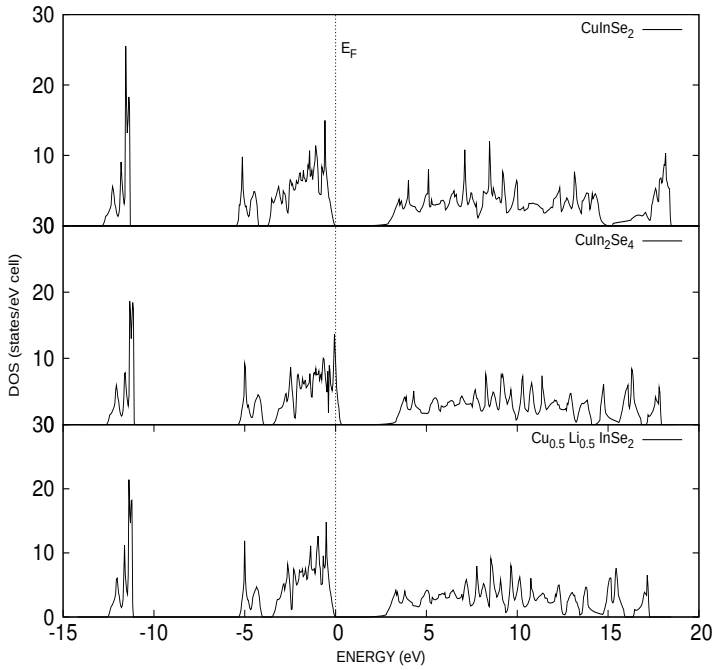

Figure 3.37: TDOS of $CuInSe_2$, $CuIn_2Se_4$ and Li substituted $CuInSe_2$ for ideal case without hybridization.

fect. In $CuNaIn_2S_4$, Na acts as a catalyst for large reduction in band gap compare to $CuIn_2S_4$.

Though we have not calculated the band gap reduction due to p-d hybridization in the case of $CdXGa_2S_4$ ($X = Ag, Al$) but from figure 3.27 we can see there is p-d hybridization in $CdAgGa_2S_4$. Therefore we can say that there is reduction in band gap in case of $CdAgGa_2S_4$ than other one. Therefore, we find a large difference of band gap of 1.23 eV between $CdAgGa_2S_4$ and $CdAlGa_2S_4$ (table 3.8).

3.2.3 Effect of structural distortion :

Structural distortion also affects the band gap of both group $I-III-VI_2$ and $II-IV-V_2$ compounds significantly [36, 110]. In our study we observe that the structural distortion like bond alternation and tetragonal distortion are important factors which controls the

band gap. The structural contribution to the band gap is mainly controlled by bond alternation and has only a small contribution from tetragonal distortion [36].

We have made our calculation for ideal and non-ideal cases. In both the cases either we have considered p-d hybridization or not. This is because we want to see the band gap reduction only due to structural distortion. Table 3.10 shows the quantitative estimation of effect of structural distortion on band gaps. Table 3.10 shows that there is increment of band gap in the case of $AgAlM_2$ (M = S, Se, Te). The increment is maximum in the case of $AgAlS_2$ because anion displacement is maximum (u = 0.265) in this system. As u increases, the hybridization between Ag d & S p decreases. Therefore the occupied valence bands are stabilized by moving down in energy and the antibonding conduction bands are destabilized by moving up in energy. This leads to band gap increment. Our study shows that structural distortion not only affects the band gap but also the overall electronic properties significantly. This is clear from figure 38 (TDOS-ideal) and figures 3,5,7 (TDOS-non-ideal) of $AgAlM_2$. A close comparison of TDOS for ideal (figure 3.38) and non-ideal (figures 3.3, 3.5 and 3.7) show distinct differences in the structure in DOS. For example a very sharp peak is found at energy -3.79 eV for non-ideal $AgAlS_2$ (figure 3.3) compared to the corresponding ideal case (figure 3.38). This is due to individual character of Ag d and S p states. Figure 3.3 also shows that second and third bands get separated due to distortion in case of $AgAlS_2$ and hence increment of band gap by 0.11 eV. Similar result is observed in case of $AgAlSe_2$ and $AgAlTe_2$ as shown in figure 3.38. For example a sharp peak at 4.64 eV which appears in ideal $AgAlTe_2$ case disappears due to distortion. This is due to weaker p-d hybridization in non-ideal case. The width of the upper most valence band in case of $AgAlTe_2$ also decreases by 0.24 eV. There are effects on conduction band also. Like in the case of $AgAlS_2$ there is a sharp peak at 5.85

Table 3.10: Effect of structural distortion on band gap (eV).

Systems	Ideal (eV)	Non-ideal (eV)	increament in band gap (%)
$AgAlS_2$	3.46	3.80	9.8
$AgAlSe_2$	2.67	2.89	8.2
$AgAlTe_2$	2.15	2.26	5.1
$AgAl_2Se_4$	2.15	2.40	11.62
$CuAl_2Se_4$	2.44	2.50	2.45
$CdAl_2Se_4$	2.39	2.46	2.92
$ZnAl_2Se_4$	2.58	2.82	9.30
Systems	Ideal	Non-ideal	decreament in band gap (%)
$ZnSnP_2$	1.68	1.44	14.48
$ZnSnAs_2$	1.08	0.96	7.40
$ZnSnSb_2$	0.60	0.50	16.66
$CuInSe_2$	0.95	0.79	16.85
$CuIn_2Se_4$	1.65	1.5	9.10
$CuLiIn_2Se_4$	1.09	1.08	0.92
$CuIn_2S_4$	2.66	2.25	15.41
$CuNaIn_2S_4$	2.21	1.99	9.95

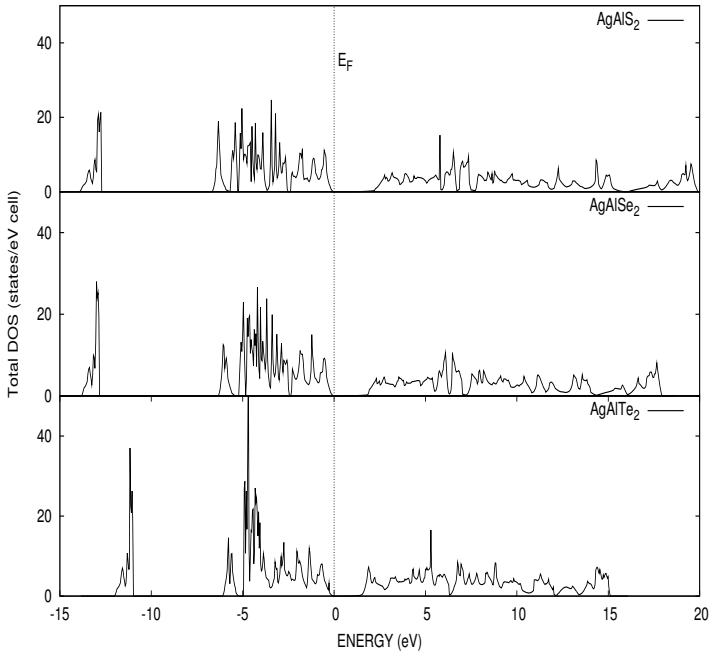

Figure 3.38: TDOS of $AgAlS_2$, $AgAlSe_2$ and $AgAlTe_2$ for ideal case with hybridization.

eV which disappears due to distortion. The conduction band width also decreases, 0.6 eV for $AgAlS_2$ and 0.36 eV for $AgAlTe_2$.

Our study on defect systems AAl_2Se_4 also gives similar result. A close comparison of

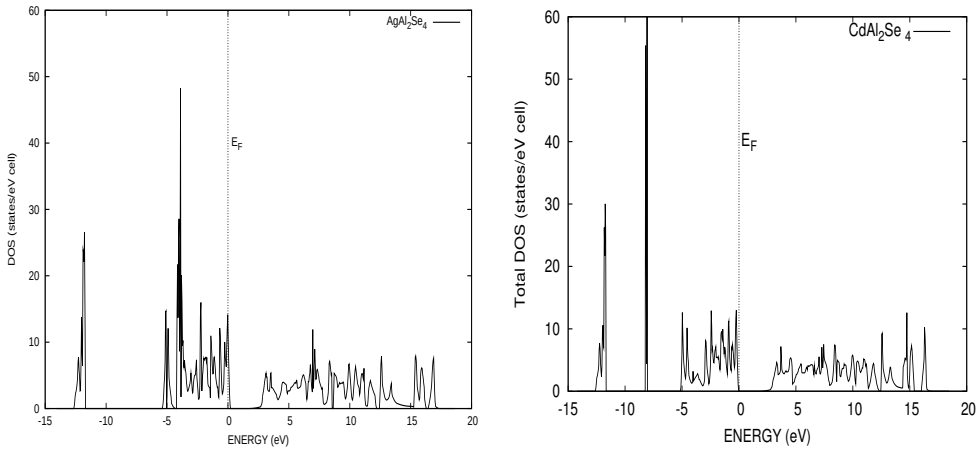

Figure 3.39: TDOS of$AgAl_2Se_4$ and $CdAl_2Se_4$ for ideal case with hybridization.

TDOS for ideal (figure 3.39 (left)) and non-ideal (figure 3.13) cases of $AgAl_2Se_4$ shows distinct differences in the structure in DOS. For example a sharp peak is found nearly at energy -4.0 eV for ideal $AgAl_2Se_4$ compared to the corresponding non-ideal case. The

sharp peak comes due to the contribution of Ag d orbitals. This shows that structural distortion not only increases the band gap but it has significant effect on overall electronic properties as well. Similar results are also found for $CuAl_2Se_4$, $CdAl_2Se_4$ and $ZnAl_2Se_4$ systems. TDOS for ideal $CdAl_2Se_4$ is plotted (figure 3.39 (right)). In these systems also the sharp peaks come due to Cu d, Cd d and Zn d orbitals respectively. There are effects on conduction band also in all four defect chalcopyrites.

Table 3.10 shows there is a reverse effect of structural distortion on band gap in case of $ZnSnX_2$ (X = P, As, Sb). That is, the band gap reduces for non-ideal structure. This is because there is no tetragonal distortion ($\eta = 1$) but there is only anion displacement in these three compounds. We find that the decrement in band gap due to structural distortion is maximum in the case of $ZnSnP_2$ because the anion displacement is maximum (u = 0.230). As u decreases, $(u < 1/4)$, excess charge is placed on the bond which is shorter i.e. on Zn-X bond and charge is depleted from the bond which is elongated i.e. on Sn-X bond. Due to this the upper valence band, which contains a majority of Zn-X mixed states, stabilizes by moving up in energy. The lower conduction band which mainly contains Sn-X mixed states is destabilized by moving down in energy. Thus there is a decrement in band gap due to structural distortion in these three cases. Like $ZnSnX_2$ chalcopyrite compounds, we also find reduction in band gap due to the structural distortion in $CuInSe_2$, $CuIn_2Se_4$ and $CuLiIn_2Se_4$. We also observe significant effect of structural distortion on TDOS and so on electronic properties in these three systems. A close comparison of TDOS for ideal (figure 3.40) and non-ideal case (figures3.9, 3.20 and 3.28) of all three compounds show distinct differences in the structure in DOS. For example a sharp peak is found at an energy -2.0 eV for nonideal $CuLiIn_2Se_4$ (figure 28) compared to the corresponding ideal case (figure 40). The sharp peak comes due to the

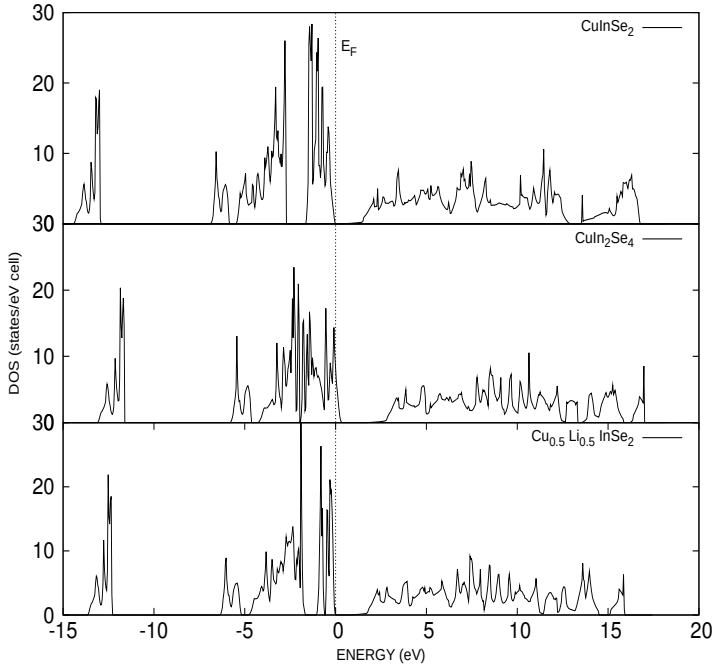

Figure 3.40: TDOS of $CuInSe_2$, $CuIn_2Se_4$ and $Cu_{0.5}Li_{0.5}InSe_2$ for ideal case with hybridization.

contribution of Se p orbitals. But in case of ideal $CuLiIn_2Se_4$, DOS is high for Cu d orbitals. There are effects on conduction band also. We also find the similar effect in the case of $CuIn_2S_4$ and $CuNaIn_2S_4$.

From the study of the effects of structural and p-d hybridization on electronic properties and band gap, we expect they would also have significant effects on optical properties.

3.2.4 Effect of Cation-Electronegativity

It is known that electro-negativity decreases the covalent nature of bonding. Therefore this should also have effect on band gap. Jaffe et.al. have shown that the cation-electronegativity contribution to the band gap anomaly is nearly equal to 0.1-0.2 eV in ternary chalcopyrites. This is very small effect. We have shown that the effect of p-d hybridization on band gap reduction is prominent in $I-III-VI_2$ where as it is in general

Table 3.11: Effect of cation-electronegativity (CE) contribution on band gap (eV).

Systems	E_g (eV)	Difference (eV)	increament in band gap (%)
$ZnSnP_2$	1.68		
$GaInP_2$	1.52	0.16	10.52
$ZnSnAs_2$	1.12		
$InGaAs_2$	1.08	0.04	3.70
$ZnSnSb_2$	0.57		
$GaInSb_2$	0.44	0.13	29.54

negligible in $II-IV-V_2$ chalcopyrite, except in $ZnSnX_2$ (X = P, As, Sb. Therefore this small effect of cation-electronegativity is significant in case of $II-IV-V_2$ compounds in comparison to the effect of p-d hybridization. Therefore it is important to study the quantitative effect of cation-electronegativity in case of $II-IV-V_2$ compounds.

We study the cation-electronegativity effect of $ZnSnX_2$ compounds in comparison to their binary analogs ($III-III-V_2$ compounds). $ZnSnX_2$ (X = P, As, Sb) are the crossed analogs of $GaInP_2$, $InGaAs_2$ and $GaInSb_2$ respectively [70]. A clear definition of a crossed analogs is given by Jaffe et.al. [36] and Brudnyi [70]. So the cation-electronegativity (CE) contribution to the band gap anomaly of $ZnSnP_2$ is the difference in band gaps of $GaInP_2$ (with chalcopyrite space group) and $ZnSnP_2$. Similar study has been carried out by Martins et.al. [130] for $MgSiP_2$ with its binary analogs AlP.

To estimate the quantitative effect of CE in $ZnSnX_2$, we freeze the d orbitals of Ga in $GaInP_2$ and $GaInSb_2$ and d orbitals of In in $InGaAs_2$. To exclude the structural effect on band gap, we use the lattice parameters of $GaInP_2$, $InGaAs_2$ and $GaInSb_2$ for

$ZnSnX_2$ (X = P, As, Sb) respectively. The whole calculation is carried out considering the ideal structure of $ZnSnX_2$. From table 3.11 we observe that CE effect is responsible for increasing the band gap of $ZnSnX_2$ relative to their binary analogs.

Chapter 4

Theory of Optical Properties

The various ways in which light interacts with matter are absorption, transmission, reflection, scattering or emission. These properties are energy dependent. The study of optical properties of solids is a powerful tool to understand the electronic properties of materials because the energy dependence of the above optical properties is related to the band structure. Therefore informations on energy eigen values and energy eigen function are needed to calculate the frequency/energy dependent optical properties.

When light of sufficient energy shines on a material, it induces transitions of electrons from occupied states (below E_F) to the unoccupied states (above E_F). The quantitative study of these transitions provides some understanding of the position of the initial and final energy bands and symmetry of their associated wavefunctions.

The dielectric function $\varepsilon(\omega, q)$, with its strong dependence on frequency and wavevector, has significant consequences for physical properties of solids. The dielectric function depends sensitively on the electronic band structure of a crystal. Studies of dielectric function by optical spectroscopy are very useful in determination of the overall band structure of the crystal.

In the infrared, visible and ultraviolet spectra regions, the wavevector of the radiation is very small as compared to the shortest reciprocal lattice vector and therefore it is taken to be zero. We are concerned with the real ($\varepsilon_1(\omega)$) and imaginary ($\varepsilon_2(\omega)$) parts of the dielectric function.

$$\varepsilon(\omega) = \varepsilon_1(\omega) + i\varepsilon_2(\omega) \tag{4.1}$$

The $\varepsilon(\omega)$ has contribution from interband and intra band transitions.

4.1 Intraband and Interband Transitions

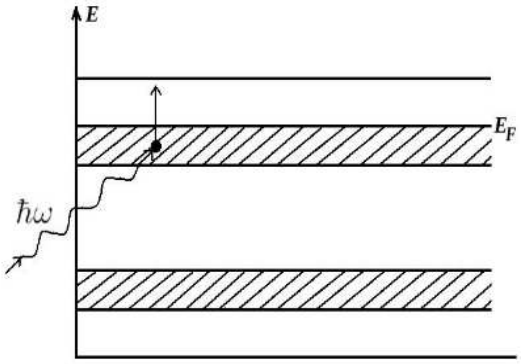

Figure 4.1: Intraband transition in metal.

When an electron in a partly filled band is excited to an empty state within the same band, then such excitations are called intraband transitions. This process is shown in figure 4.1. If only the electron-photon interaction is considered, the real intraband transitions are not possible. It is because the necessary momentum change in going to different state in the same band can not be provided by the photon. It becomes possible only by simultaneous scattering of mobile carrier by phonons or impurities. The theory for such an absorption process was first given by Drude and the model is known as the Drude

model [207]. In this model, Drude used a classical approach. The basic assumption was that the optical conductivity and the dielectric function could be determined by considering the motion of quasi free electrons under the influence of the oscillating electric field vector of the electromagnetic wave. But the optical spectrum of a real crystal of a metal, a semiconductor or a disorderd systems usually has more structures in the visible region to the far UV region (10 eV) than those arising from Drude absorption and the occurance of plasma oscillations of free electron accelerated by the electric field of the light wave. These structures are seen in the form of peaks, edges etc in the absorption versus frequency curve. These structures arise due to the interaction of the electrons only with the electromagnetic radiation i.e. with photons. Then the electron is directly excited from one electronic band to another band. This process is called interband transitions. This

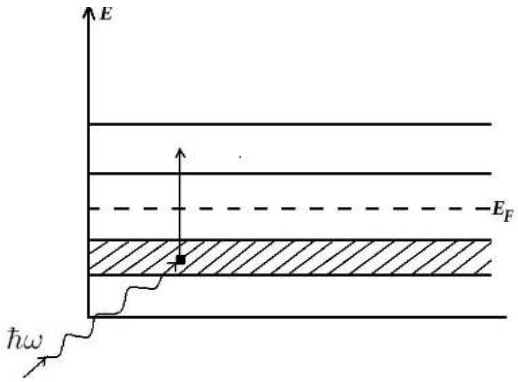

Figure 4.2: Interband transition in semiconductor

process is shown in figure 4.2. In materials like insulators, semiconductors or alloys of these, this is the only kind of absorption that takes place because in such materials the conduction band is completely unfilled. So the excitation of electrons take place from the completely filled valence band to the completely unfilled conduction band. So Drude absorption is not possible for these cases. To understand these process, one need to go beyond the classical approach and develope a quantum transport theory. In such a theory

the electon-photon interaction is considered to be the exciting part of the Hamiltonian. A time dependent perturbation formalism is applied to obtain expression for the optical responce functions of the system. Such a linear responce theory was first suggested by Kubo [208].

4.2 Optical Response Functions

In this section, we shall study the linear response of electrons in a solid to extenal electromagnetic radiation from the IR to the UV region (0.1-10 eV).

In particular we shall describe the dielectric function $\varepsilon(\omega)$, optical conductivity $\sigma(\omega)$ and permeability $\mu(\omega)$ as the main properties usually studied experimentally. Here ω is the angular frequency of the external electromagnetic radiations. In the optical region (IR-UV) we shall choose non-magnetic systems where $\mu(\omega) \simeq 1$. The dielectric function $\varepsilon(\omega)$, conductivity function $\sigma(\omega)$ and permeability function $\mu(\omega)$ are defined through the following relations.

$$\mathbf{D}(\omega) = \varepsilon(\omega)\mathbf{E}(\omega) \tag{4.2}$$

$$\mathbf{J}(\omega) = \sigma(\omega)\mathbf{E}(\omega) \tag{4.3}$$

$$\mathbf{H}(\omega) = \frac{1}{\mu(\omega)}\mathbf{B}(\omega) \tag{4.4}$$

respectively. Here $\mathbf{D}$, $\mathbf{E}$, $\mathbf{J}$, $\mathbf{H}$ and $\mathbf{E}$ are the displacement field, the electric field, the current density, the magnetic field and the magnetic induction vectors respectively. A related response is the refractive index function $n(\omega)$ which is related to $\varepsilon(\omega)$ through

$$n(\omega) = \sqrt{\varepsilon(\omega)} \tag{4.5}$$

Another response function related to the refractive index is reflectance R. It is given by

$$R = \left|\frac{1-n}{1+n}\right|^2 \tag{4.6}$$

The absorption function $\alpha(\omega)$ is defined as the fraction of energy absorbed in passing through the unit length of the material.

Electromagnetic waves are the solution of Maxwell's equations. For the linear and homogeneous medium, these equations are given below

$$\nabla \times \mathbf{H} = \frac{1}{c}\frac{\partial \mathbf{D}}{\partial t} + \frac{4\pi}{c}\mathbf{J} \tag{4.7}$$

$$\nabla.\mathbf{D} = 0 \tag{4.8}$$

$$\nabla \times \mathbf{E} = -\frac{1}{c}\frac{\partial \mathbf{H}}{\partial t} \tag{4.9}$$

$$\nabla.\mathbf{H} = 0 \tag{4.10}$$

The wave equation in which only the electric field is involved is

$$\nabla^2\mathbf{E} = \frac{\varepsilon}{c^2}\frac{\partial^2\mathbf{E}}{\partial t^2} + \frac{4\pi\sigma}{c^2}\frac{\partial \mathbf{E}}{\partial t} \tag{4.11}$$

The second part in the above equation is due to damping and the whole equation repre-

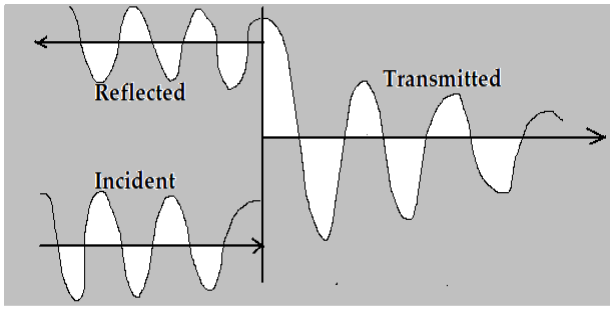

Figure 4.3: Damping of electromagnetic waves in solids.

sents the electromagnetic wave propagating in the solid with damping (figure 4.3). The wavelike solution of the previous equation is

$$\mathbf{E} = \mathbf{E_0}\ exp\left(i(\mathbf{q}.\mathbf{r} - \omega t)\right) \tag{4.12}$$

Solving the equation finally we will get

$$-q^2 = -\varepsilon\frac{\omega^2}{c^2} - \frac{4\pi\sigma i\omega}{c^2}$$

$$\Rightarrow q = \frac{\omega}{c}\left[\varepsilon + i\frac{4\pi\sigma}{\omega}\right] \tag{4.13}$$

In general, q is a complex propagation vector. In free space,

$$q = \frac{\omega}{c} \tag{4.14}$$

for ordinary light. In any medium, the wave is travelling with the modified velocity v and $v = c/n$ where n is the refractive index of the medium. So

$$q = \frac{\omega}{v}$$

$$\Rightarrow q = \frac{\omega}{c}\,\tilde{n} \tag{4.15}$$

Comparing the relations between 4.13 and 4.15 we have

$$\tilde{n} = \left[\varepsilon + i\frac{4\pi\sigma}{\omega}\right]^{1/2} \tag{4.16}$$

So the complex dielectric function $\varepsilon(\omega)$ is defined as

$$\tilde{\varepsilon}(\omega) = \varepsilon(\omega) + i\frac{4\pi\sigma(\omega)}{\omega} \tag{4.17}$$

The real part of the complex dielectric function is the measured dielectric response of the medium and the imaginary part is related to optical conductivity or optical absorption co-effecient α. The complex refractive index can be written as

$$\tilde{n}(\omega) = n(\omega) + in_z(\omega) \tag{4.18}$$

$n(\omega)$ is the measured refractive index.

$$q\hat{e}_\gamma = \frac{\omega}{c}\left[n(\omega) + in_z(\omega)\right]\hat{e}_\gamma \tag{4.19}$$

where $\hat{e}_\gamma$ is the direction of polarization of electromagnetic wave. So the equation 4.12 becomes

$$\mathbf{E} = \mathbf{E_0} exp\left[i\omega\left(\frac{n\hat{e}_\gamma.\mathbf{r}}{c} - t\right)\right] exp\left[\frac{-n_z\omega\hat{e}_\gamma.\mathbf{r}}{c}\right] \tag{4.20}$$

Inside the medium, the velocity of the propagation is c/n and the wave is damped as it progresses. The damping of wave associated with absorption of electromagnetic energy. The absorption co-efficient $\alpha(\omega)$ is given by

$$\alpha(\omega) = \frac{4\pi\sigma(\omega)}{n(\omega)} \tag{4.21}$$

Experimentally it is measured as follows. When a beam of light of intensity I_0 goes normally through a slab of a medium of thickness x, the beam of light attenuates in accordance with the exponential law $I = I_0 exp(-\alpha x)$. α can be then simply obtained by measuring I_0/I of the intensities impinging and emerging from sample.

It is seen that the whole optical properties can be described by the complex dielectric function. The real and imaginary parts are dependent. The analytical properties of complex dielectric function leads to the Kramers-Kronig ralation

$$\varepsilon(\omega) = 1 + \frac{2}{\pi}\int_0^\infty \frac{(\omega' - \omega)\varepsilon_z(\omega')}{\omega'^2 - \omega^2} d\omega' \tag{4.22}$$

and the optical sum rules

$$\int_0^\infty \omega\varepsilon_z(\omega) d\omega = \frac{1}{2}\pi\omega_p^2 \tag{4.23}$$

$$-\int_0^\infty \omega Im\tilde{\varepsilon}^{-1}(\omega) d\omega = \frac{1}{2}\pi\omega_p^2 \tag{4.24}$$

where $\tilde{\varepsilon} = \varepsilon + i\varepsilon_z$ and ω_p is the plasma frequency.

4.2.1 Interband : Direct and Indirect Transitions

As we discussed before, the intraband transition is possible only in metals where as interband transition is possible for all materials. Interband transition takes place in the range of frequency $\omega_0 \leq \omega < \omega_p$, where ω_0 is the threshold value for interband transition lies in the visible region and ω_p is the plasma frequency lies in the far UV region.

The quantum trasport theory for interband transition can be developed for two different cases. First at the temperature 0^0 K and onther, at some finite temperature. The nature of interband electronic transition, in these two cases, is very different from each other. At 0^0 K there is negligible number of phonons present. So the electrons absorb only photon energy. The momentum conservation requires

$$\hbar\mathbf{k_f} = \hbar\mathbf{k_i} + \hbar\mathbf{Q} \tag{4.25}$$

where $\mathbf{k_f}$ and $\mathbf{k_i}$ are the final and initial wave vectors of the electron and $\mathbf{Q}$ is the wave vector of the photon. Basically we are considering here only the region of IR to UV light for which wavelength is much large compared to the lattice constant. Therefore $\mathbf{Q}$ is much smaller than the $\mathbf{k}$'s. Thus the momentum of the photon may be neglected and finally we get

$$\hbar\mathbf{k_f} = \hbar\mathbf{k_i} \Rightarrow \mathbf{k_f} = \mathbf{k_i} \tag{4.26}$$

This shows that transition takes place vertically upward in the reduced Brillouin zone scheme. It is shown in figure 4.4. This kind of interband transition is called direct transition. The other kind of interband transition is the indirect transition. This kind of transition process is observed in the higher temperature region. At finite temperatures there are sufficient phonon present. Therefore electron absorbs phonon energy as well as

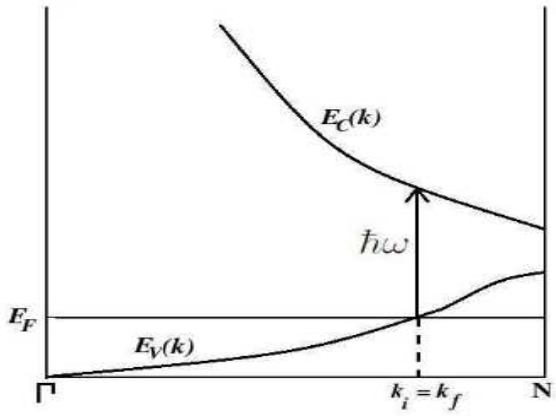

Figure 4.4: Interband : Direct transition

photon energy. So in this case, the conservation of momentum gives

$$\hbar\mathbf{k_f} = \hbar\mathbf{k_i} + \hbar\mathbf{Q} + \hbar\mathbf{q} \tag{4.27}$$

where $\mathbf{q}$ is the phonon wave vector. Since $\hbar\mathbf{Q} \simeq 0$, therefore $\mathbf{k_f} = \mathbf{k_i} + \mathbf{q}$. Hence

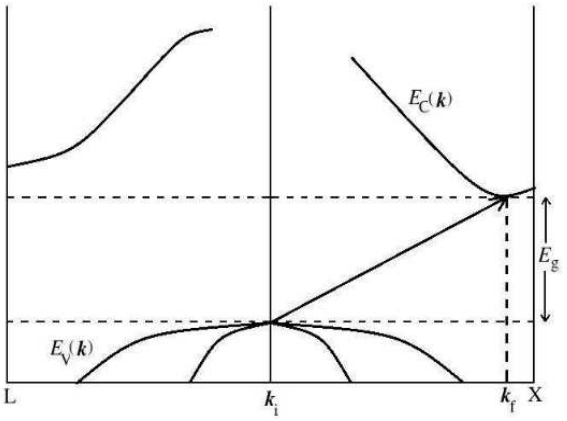

Figure 4.5: Interband : Indirect transition

$\mathbf{k_f} \neq \mathbf{k_i}$. So in this case the transition is not vertical in the reduced zone scheme. This process is shown in figure 4.5.

4.2.2 Basic Formula for Optical Conductivity

The fundamental expression for optical conductivity can be derived from 1^{st} order time dependent perturbation theory. The crystal Hamiltonian is treated as the unperturbed Hamiltonian and the eigenfunctions of this Hamiltonian as the unperturbed eigenfunctions. The one electron Schrodinger equation for such unperturbed system is given by

$$\mathbf{H}_0\psi^0_{\mathbf{k}} = \left[\frac{-\hbar^2}{2m^*}\nabla^2 + V(\mathbf{r})\right]\psi^0_{\mathbf{k}} = E_{\mathbf{k}}\psi^0_{\mathbf{k}} \tag{4.28}$$

where $\mathbf{H}_0$: crystal Hamiltonian, $V(\mathbf{r})$: crystal potential, $\psi^0_{\mathbf{k}}(\mathbf{r})$: eigenfunctions of $\mathbf{H_0}$, m^* : the effective mass of the electron in the solid.

When electromagnetic radiation falls on the material, the photons interact with the electrons in solids. This electromagnetic wave usually carries a weak electromagnetic field. The electromagnetic radiation adds on extra potential to the crystal Hamiltonian during interaction. This weak, time dependent potential is treated as the perturbation. Then the total Hamiltonian is given by

$$\mathbf{H} = \mathbf{H_0} + \mathbf{H_1} \tag{4.29}$$

In general the Hamiltonian associates with an electron in an electromagnetic field is

$$\mathbf{H}' = \frac{1}{2m^*}\left(\mathbf{p} - \frac{e}{c}\mathbf{A}\right)^2 + e\phi \tag{4.30}$$

where $\mathbf{p} = \frac{\hbar}{i}\nabla$ is the momentum operator, $\mathbf{A}(\mathbf{r},\mathbf{t})$: vector potential associated with the electromagnetic field, $\phi(\mathbf{r},\mathbf{t})$: scalar potential associated with the electromagnetic field. When free charges are absent we can choose

$$\phi(\mathbf{r},\mathbf{t}) = \mathbf{0} \tag{4.31}$$

So H' reduces to

$$H' = \frac{1}{2m^*}\left(\mathbf{p} - \frac{e}{c}\mathbf{A}\right)^2 \tag{4.32}$$

$$\Rightarrow H' = \frac{1}{2m^*}\left(\mathbf{p}.\mathbf{p} + \frac{e^2}{c^2}\mathbf{A}.\mathbf{A} - \frac{e}{c}\mathbf{p}.\mathbf{A} - \frac{e}{c}\mathbf{A}.\mathbf{p}\right) \tag{4.33}$$

Since electromagnetic radiation interacting with the matter, is weak, $\mathbf{A}(\mathbf{r},\mathbf{t})$ is a weak potential. So we can neglect the higher terms. So equation 4.33 reduces to

$$\begin{aligned} H' &= \frac{1}{2m^*}\left(\mathbf{p}.\mathbf{p} - \frac{e}{c}(\mathbf{p}.\mathbf{A} + \mathbf{A}.\mathbf{p})\right) \\ &= \frac{p^2}{2m^*} - \frac{e}{2m^*c}(\mathbf{p}.\mathbf{A} + \mathbf{A}.\mathbf{p}) \end{aligned} \tag{4.34}$$

So we can write

$$H_1 = -\frac{e}{2m^*c}(\mathbf{p}.\mathbf{A} + \mathbf{A}.\mathbf{p}) \tag{4.35}$$

In the absence of free charges

$$\nabla.A = 0 \tag{4.36}$$

Again, $[\mathbf{A},\mathbf{p}] = \mathbf{i}\hbar\nabla.\mathbf{A} \Rightarrow [\mathbf{A},\mathbf{p}] = \mathbf{0}$ i.e. it commutes. Therefore $\mathbf{p}.\mathbf{A} = \mathbf{A}.\mathbf{p}$. So putting this in equation 4.35

$$H_1 = -\frac{e}{m^*c}(\mathbf{A}.\mathbf{p}) \tag{4.37}$$

The vector potential $\mathbf{A}$ that varries with time can be writen as

$$\mathbf{A} = \mathbf{A}_0 exp[i(\omega t)] \tag{4.38}$$

This extra term is introduced to the zeroth order Hamiltonian. This term $(\mathbf{H_1})$ is responsible for excitations of electrons. Electrons in an unperturbed staes $\psi_i^0(\mathbf{r})$ at a time $t = 0$ will have a wavefunction $\psi_f(\mathbf{r},\mathbf{t})$ at time t. This wavefunction is be composed of complete set of eigen states, $\{\psi_i^0(\mathbf{r})\}$ of $\mathbf{H_0}$. Here $\psi_i^0(\mathbf{r})$ is the initial state i.e. the state before the transition and $\psi_f(\mathbf{r})$ is the final state i.e. state after transition.

We are interested to calculate the transition rate between an occupied state ψ_i and unoccupied state ψ_f. This can be calculated by solving the equation for $\psi(\mathbf{r},\mathbf{t})$ by the standard

first order time dependent perturbation theory.

The rate of transition accompanied by the absorption of a photon of frequency ω from the radiation field is

$$Q_{\mathbf{k_f k_i}} = \frac{2\pi}{\hbar}|\langle\psi_f|\mathbf{H_1}|\psi_i\rangle|^2\delta(E_f - E_i - \hbar\omega) \tag{4.39}$$

The delta function appears due to conservation of energy.

Due to this transition, the energy absorbed per unit volume per unit time is $\frac{\hbar\omega}{\Omega}Q_{\mathbf{k_f k_i}}$. Ω is the volume of the sample. We can find the total rate of energy loss by summing this over initial and final states of the electrons in the systems. A factor $f_i(1-f_f)$ should be introduced in the equation 4.39 for this purpose. Here f_i is the probability of occupation of the states $\psi_i(\mathbf{r})$ and f_i is the probability of occupation of the states $\psi_f(\mathbf{r},\mathbf{t})$. Then the total rate of energy loss is

$$\frac{1}{\Omega}\sum_i\sum_f f_i(1-f_f)\hbar\omega Q_{\mathbf{k_f k_i}}$$

$$= \frac{1}{\Omega}\sum_i\sum_f f_i(1-f_f)\hbar\omega\left(\frac{2\pi}{\hbar}\mid\langle\psi_f\mid\mathbf{H_1}\mid\psi_i\rangle\mid^2\delta(E_f-E_i-\hbar\omega)\right)$$

$$= \frac{\hbar\omega}{\Omega}\frac{2\pi}{\hbar}\sum_i\sum_f f_i(1-f_f)\left|\left\langle\psi_f\left|\left(-\frac{e}{m^*c}\mathbf{A}.\mathbf{p}\right)\right|\psi_i\right\rangle\right|^2\delta(E_f-E_i-\hbar\omega)$$

$$= -\frac{2\pi\omega e^2}{m^{*2}c^2\Omega}\sum_i\sum_f f_i(1-f_f)\left|\langle\psi_f\left|\mathbf{A}.\mathbf{p}\right)\right|\psi_i\rangle\right|^2\delta(E_f-E_i-\hbar\omega) \tag{4.40}$$

This total rate of energy loss is equal to the joule heat loss due to the mobile electrons i.e. $\mathbf{J}.\mathbf{E}$. For linear and isotropic medium $\mathbf{J}=\sigma\mathbf{E}\Rightarrow\mathbf{J}.\mathbf{E}=\sigma\mathbf{E}.\mathbf{E}$. Here the electric field $\mathbf{E}=\frac{i\omega}{c}\mathbf{A}$

$$\mathbf{J}.\mathbf{E}=\sigma\mathbf{E}.\mathbf{E}=\sigma\left(\frac{i\omega}{c}\right)^2\mathbf{A}.\mathbf{A}$$

$$\mathbf{J}.\mathbf{E}=-\sigma\left(\frac{\omega}{c}\right)^2\mathbf{A}.\mathbf{A} \tag{4.41}$$

Equating equation 4.40 and 4.41, we get

$$-\sigma\left(\frac{\omega}{c}\right)^2 \mathbf{A}.\mathbf{A} = -\frac{2\pi\omega e^2}{m^{*2}c^2\Omega}\sum_i\sum_f f_i(1-f_f)\left|\langle\psi_f\left|(\mathbf{A}.\mathbf{p})\right|\psi_i\rangle\right|^2\delta(E_f-E_i-\hbar\omega)$$

Again $\mathbf{A} = A\hat{e}_\gamma$ where $\hat{e}_\gamma$ is the polarization direction of the electric field vector $\mathbf{E}$. The above equation becomes

$$\sigma(\omega) = -\frac{2\pi e^2}{m^{*2}c^2\omega}\sum_i\sum_f f_i(1-f_f)\left|\langle\psi_f\left|(\hat{e}_\gamma.\mathbf{p})\right|\psi_i\rangle\right|^2\delta(E_f-E_i-\hbar\omega) \qquad (4.42)$$

This is the basic formula for the opical conductivity of a solid due to interband transition. This formula can be applied to any kind of materials like metals, semiconductors or insulators etc for direct interband transitions.

4.2.3 Analysis of the Conductivity Formula

The Kubo formula for optical conductivity (eq. 42) has two important factors

(i) Conservation of energy i.e. $\delta(E_f - E_i - \hbar\omega)$

(ii) Square of the optical matrix elements i.e. $\left|\langle\psi_f\left|(\hat{e}_\gamma.\mathbf{p})\right|\psi_i\rangle\right|^2$

1. Conservation of energy i.e. $\delta(E_f - E_i - \hbar\omega)$: We know that the electon density of states i.e. number of allowed energy levels per unit energy range and per unit volume is given by

$$n(E) = \frac{2}{\Omega}\sum_n \delta(E-E_n) \qquad (4.43)$$

Here Ω is the volume of the sample. In the above equation the summation is taken over the two spin orientation. So 2 is multiplied. According to the properties of Dirac δ function.

$$\int \delta(E-E_i)\delta(E_f-E)dE = \delta(E_f-E_i) \qquad (4.44)$$

We have

$$\delta(E_f - E_i - \hbar\omega) = \int_0^{E_f^{max}} \delta(E - E_f)\delta(E - E_i - \hbar\omega)dE \tag{4.45}$$

where E_f^{max} is the upper limit of conduction band. We can write 45

$$\sum_f \sum_i \delta(E_f - E_i - \hbar\omega) = \int_0^{E_f^{max}} \delta(E - E_f)\delta(E - E_i - \hbar\omega)dE$$

$$\Rightarrow \sum_f \sum_i \delta(E_f - E_i - \hbar\omega) = \int_0^{E_f^{max}} \sum_f \delta(E - E_f) \sum_i \delta(E - E_i - \hbar\omega)dE \tag{4.46}$$

Using the definition 43, the right hand side of equation 4.46 can be written in terms of conduction band density of states $n_f(E)$ and valence band density of states $n_i(E)$

$$\sum_f \sum_i \delta(E_f - E_i - \hbar\omega) = \frac{\Omega^2}{4} \int_0^{max} n_f(E) n_i(E - \hbar\omega)dE \tag{4.47}$$

We can write $n_f(E)n_i(E - \hbar\omega) = J_{fi}(E, \omega)$. $J_{fi}(E, \omega)$ is the joint density of states. So eq. 47 can be written as

$$\sum_f \sum_i \delta(E_f - E_i - \hbar\omega) = \frac{\Omega^2}{4} \int_0^{max} J_{fi}(E, \omega)dE \tag{4.48}$$

We know that for an ordered or periodic system, the crystal potential is periodic and the wave-function is described by Bloch's function. If the optical matrix element is a very slowly varying function of energy, it can be replaced by its **K** average. This was the usual assumption in the early works [209]. Let the optical matrix elements are denoted by $g_{if\gamma}$. Then $|g_{if\gamma}|^2$ may be replaced by its **k** average,$\overline{|\ g_{if\gamma}\ |}^2$. So $\overline{|\ g_{if\gamma}\ |}^2$ can be taken out of the integral. With this approximation, eq. 42 becomes

$$\sigma(\omega) = -\frac{2\pi e^2}{m^{*2}c}\frac{1}{\omega}\overline{|\ g_{if\gamma}\ |}^2 \sum_i \sum_f f_i(1 - f_f)\delta(E_f - E_i - \hbar\omega) \tag{4.49}$$

For semiconductor, at $T = 0^0K$, $f_i = 1$ and $f_f = 0$. So using this, equation 4.49 reduces to

$$\sigma(\omega) = -\frac{2\pi e^2}{m^{*2}c}\frac{1}{\omega}\overline{|\ g_{if\gamma}\ |}^2 \sum_i \sum_f \delta(E_f - E_i - \hbar\omega) \tag{4.50}$$

Using equation 4.48 in 4.50, we have

$$\sigma(\omega) = -\frac{2\pi e^2}{m^{*2}c}\frac{1}{\omega}\overline{\mid g_{if\gamma} \mid}^2 \frac{\Omega^2}{4}\int_0^{E_{max}} J_{fi}(E,\omega)dE \tag{4.51}$$

So we can say that for a fixed value of ω, we have

$$\omega\sigma(\omega) \propto \int J_{fi}(E,\omega)dE \tag{4.52}$$

Therefore, the optical properties of any ordered system is directly propertional to the integrated joint density of states. But in general the square of optical matrix elements may depend strongly on energy and so on crystal potential. In that case the assumption taken above is not valid. Therefore one has to carry out the full integration.

The optical conductivity is related to the imaginary part of the dielectric function $\varepsilon_2(\omega)$ by the relation $\sigma(\omega) = \frac{\omega\varepsilon_2(\omega)}{4\pi}$. If we know $\varepsilon_2(\omega)$ then the real part of dielectric function $\varepsilon_1(\omega)$ can be determined by Kramer-Kronig relation as discussed before and hence the total optical properties can be known. This is the general theory to study the optical properties of different materials.

During 1980s, a number of methods have been proposed to calculate the optical properties of both metals [210, 211] and semiconductors [212, 213] within the frame work of LMTO theory [210–213]. It is seen that at high symmetry points and for allowed transitions, the optical properties can be described in terms of a contribution from the strength of matrix elements calculated at the high symmetry points and a contribution from the joint density of states.

Many calculations are performed to determine the momentum matrix elements by using gradient operator [210–213]. But Hobbs et.al. [214] has constructed momentum matrix elements using a gauge independent formalism. This formalism avoids

the determination of the gradient operator and allows for the inclusion of non-local potential in the Hamiltonian. Hobbs et.al. have employed green's second identity and the commutation relation between the position and the Hamiltonian operators. They have also shown how the momentum matrices can be written in terms of a sum over Gaunt co-efficients [215] and potential parameters [173, 216]. These potential parameters are defined within the TB-LMTO method. We here discuss the details of the evaluation of optical matrix elements within the TB-LMTO basis as discussed by Hobbs et.al. [214].

2. The Momentum Matrix : In the first step, the momentum operator can be defined by the commutation relation within the gauge-independent formalism.

$$\mathbf{p} = m_e \mathbf{v}, \;\; where \;\; v = \frac{1}{i\hbar}[\mathbf{r}, \mathbf{H}] \tag{4.53}$$

In the next step, we need to determine the one-electron wavefunction and this has been defined within LMTO theory [172, 177].

The L-decomposed wavefunction can be written as a linear combination of the energy independent basis function

$$\psi_L^{jk}(\mathbf{r}) = A_L^{jk}\phi_{\nu L}(\mathbf{r}) + B_L^{jk}\dot{\phi}_{\nu L}(\mathbf{r}) \tag{4.54}$$

The co-efficients A and B can be defined in terms of the potential parameters and the canonical structure constants [177].

The optical matrix elements then can be given by

$$\langle \psi^{j'k} \mid \mathbf{p} \mid \psi^{jk} \rangle = m_e \sum_{L'L} \langle \psi_{L'}^{j'k} \mid \mathbf{v} \mid \psi_L^{jk} \rangle \tag{4.55}$$

The optical matrix elements can be expanded in terms of the L-decomposed wave-

function.

$$\langle \psi^{j'k} \mid \mathbf{p} \mid \psi^{jk} \rangle = m_e \sum_{L'L} \langle A_{L'}^{j'k} \phi_{\nu L'}(\mathbf{r}) + B_{L'}^{j'k} \dot{\phi}_{\nu L'}(\mathbf{r}) \mid v \mid A_L^{jk} \phi_{\nu L}(\mathbf{r}) + B_L^{jk} \dot{\phi}_{\nu L}(\mathbf{r}) \tag{4.56}$$

$$\langle \psi^{j'k} \mid \mathbf{p} \mid \psi^{jk} \rangle = m_e \sum_{L'L} A_{L'}^{j'k^*} A_L^{jk} \langle \phi_{\nu L'}(\mathbf{r}) \mid v \mid \phi_{\nu L}(\mathbf{r}) \rangle$$

$$+ m_e \sum_{L'L} A_{L'}^{j'k^*} B_L^{jk} \langle \phi_{\nu L'}(\mathbf{r}) \mid v \mid \dot{\phi}_{\nu L}(\mathbf{r}) \rangle + m_e \sum_{L'L} B_{L'}^{j'k^*} A_L^{jk} \langle \dot{\phi}_{\nu L'}(\mathbf{r}) \mid v \mid \phi_{\nu L}(\mathbf{r}) \rangle$$

$$+ m_e \sum_{L'L} B_{L'}^{j'k^*} B_L^{jk} \langle \dot{\phi}_{\nu L'}(\mathbf{r}) \mid v \mid \dot{\phi}_{\nu L}(\mathbf{r}) \rangle \tag{4.57}$$

Using eq. 53, the 1st term of eq.57 becomes

$$\langle \phi_{\nu L'}(\mathbf{r}) \mid v \mid \phi_{\nu L}(\mathbf{r}) \rangle = \langle \phi_{\nu L'}(\mathbf{r}) \mid \frac{1}{i\hbar}[\mathbf{r}, H] \mid \phi_{\nu L}(\mathbf{r}) \rangle = \frac{1}{i\hbar} \langle \phi_{\nu L'}(\mathbf{r}) \mid \mathbf{rH} - \mathbf{Hr} \mid \phi_{\nu \mathbf{L}}(\mathbf{r}) \rangle$$

$$= \frac{1}{i\hbar} \int \phi^*_{\nu L'}(\mathbf{r}) \mathbf{r} H \phi_{\nu L}(\mathbf{r}) d^3r - \frac{1}{i\hbar} \int_{\nu L'}^{*} (\mathbf{r}) H r \phi_{\nu L} \phi_{\nu} L(\mathbf{r}) d^3r \tag{4.58}$$

Using

$$H\phi_{\nu L}(\mathbf{r}) = \varepsilon_{\nu tl} \phi_{\nu L}(\mathbf{r}) \tag{4.59}$$

and

$$H\dot{\phi}_{\nu L}(\mathbf{r}) = \frac{\partial(\varepsilon_{\nu tL} \phi_{\nu L}(\mathbf{r}))}{\partial E} \Rightarrow H\dot{\phi}_{\nu L}(\mathbf{r}) = \varepsilon_{\nu tL} \frac{\partial \phi_{\nu L}(\mathbf{r})}{\partial E} + \phi_{\nu L}(\mathbf{r}) \frac{\partial \varepsilon_{\nu tL}}{\partial E}$$

$$\Rightarrow H\dot{\phi}_{\nu L}(\mathbf{r}) = \varepsilon_{\nu tL} \dot{\phi}_{\nu L}(\mathbf{r}) + \phi_{\nu L}(\mathbf{r}) \tag{4.60}$$

Using the definition of the partial wave and its energy derivatives, the first integral term in equation 4.58 can be expanded as

$$\frac{1}{i\hbar} \int \phi^*_{\nu L'}(\mathbf{r}) \mathbf{r} H \phi_{\nu L}(\mathbf{r}) d^3r = \frac{1}{i\hbar} \varepsilon_{\nu tl} i^{-l'} i^l \sqrt{\frac{4\pi}{3}} G \int_0^{S_t} \phi^*_{\nu tl}(x) x \phi_{\nu tl}(x) x^2 dx \tag{4.61}$$

Here G is the product of three spherical harmonics

$$G = \left[\sqrt{\frac{1}{2}} \int Y_{l'}^{m'^*} Y_l^{-1} Y_l^m d\omega - \sqrt{\frac{1}{2}} \int Y_{l'}^{m'^*} Y_l^1 Y_l^m d\omega \right] x$$

$$+i\left[\sqrt{\frac{1}{2}}\int Y_{l'}^{m'*}Y_l^1Y_l^m d\omega - i\sqrt{\frac{1}{2}}\int Y_{l'}^{m'*}Y_l^{-1}Y_l^m d\omega\right]y$$

$$+\left[\int Y_{l'}^{m'*}Y_l^0Y_l^m d\omega\right]z \tag{4.62}$$

here x, y, z are the unit vectors of the cartesian co-ordinate system. Here $\mathbf{r}$ can be defined as

$$\mathbf{r} = \sqrt{\frac{4\pi}{3}}\left[\sqrt{\frac{1}{2}}(-Y_l^1 + Y_l^{-l})x + \sqrt{\frac{1}{2}}i(Y_l^1 + Y_1^{-1})y + Y_1^0 z\right]r \tag{4.63}$$

The second integral term of eq. 58 can be evaluated by using Green's second identity [218].

$$\int_{volume}\left[F_\alpha(\mathbf{r})\nabla^2\phi^*_{\nu L'}(\mathbf{r}) - \phi^*_{\nu L'}(\mathbf{r})\nabla^2 F_\alpha(\mathbf{r})\right]d^3r$$

$$= \iint_{surface}\left[F_\alpha(\mathbf{r})\mathbf{r}.\nabla\phi^*_{\nu L'}(\mathbf{r}) - \phi^*_{\nu L'}(\mathbf{r})\mathbf{r}.\nabla F_\alpha(\mathbf{r})\right]S_t^2 d\omega \tag{4.64}$$

Here $F_\alpha(\mathbf{r})$ is equal to the alpha component of $\mathbf{r}\phi_{\nu L}(\mathbf{r})$. The second part of equation 4.58 can be written by arranging Green's second identity and expanding in terms of the partial wave and its energy derivative. Then the second term reduces to a contribution from the integration over the spheres and a surface integral contribution i.e.

$$\frac{1}{i\hbar}\int \phi^*_{\nu L'}(\mathbf{r})H\mathbf{r}\phi_{\nu L}(\mathbf{r})d^3r$$

$$= \frac{1}{i\hbar}\left[\frac{-\hbar^2}{2m_e}\int \phi^*_{\nu L'}(\mathbf{r})\nabla^2 F(\mathbf{r})d^3r + \int \phi^*_{\nu L'}(\mathbf{r})v(\mathbf{r})F(\mathbf{r})d^3r\right] \tag{4.65}$$

Then substitution in Green's second identity gives

$$\frac{1}{i\hbar}\phi^*_{\nu L'}(\mathbf{r})H\mathbf{r}\phi_{\nu L}(\mathbf{r})d^3r$$

$$= \frac{1}{i\hbar}\left[\frac{-\hbar^2}{2m_e}\int F(\mathbf{r})\nabla^2\phi^*_{\nu L'}(\mathbf{r})d^3r + \int \phi^*_{\nu L'}(\mathbf{r})v(\mathbf{r})F(\mathbf{r})d^3r\right]$$

$$+\frac{i^{-1}\hbar}{2m_e}\iint_{surface}\left[F(\mathbf{r})\mathbf{r}.\nabla\phi^*_{\nu L'}(\mathbf{r})-\phi^*_{\nu L'}(\mathbf{r})\mathbf{r}.\nabla F(\mathbf{r})\right]S_t^2 d\omega \tag{4.66}$$

Finally by expanding in terms of the partial wave and its energy derivative and considering ϕ and $\dot{\phi}$ are real. The final result is

$$\frac{1}{i\hbar}\int\phi^*_{\nu L'}(\mathbf{r})H\mathbf{r}\phi_{\nu L}(\mathbf{r})d^3r$$

$$=\frac{i^{l-l'-1}}{\hbar}\varepsilon_{\nu tl'}\sqrt{\frac{4\pi}{3}}G\int_0^{S_t}\phi_{\nu tl}(x)x\phi_{\nu tl'}(x)x^2dx+\frac{\hbar i^{l-l'-1}}{2m_e}\sqrt{\frac{4\pi}{3}}S_t^2$$

$$[S_t\phi_{\nu tl}(S_t)\phi'_{\nu tl'}(S_t)-S_t\phi_{\nu tl'}(S_t)\phi_{\nu tl}(S_t)-\phi_{\nu tl'}(S_t)\phi_{\nu tl}(S_t)]G \tag{4.67}$$

The result is expressed in terms of an integral over the sphere and the potential parameters. The other three terms in equation 4.57 can be derived similarlly. So the 4th terms of matrix elements of the velocity operator are as follows.

$$\langle\phi_{\nu L'}(\mathbf{r})\mid v\mid\phi_{\nu L}(\mathbf{r})\rangle=\frac{i^{l-l'-1}}{\hbar}\sqrt{\frac{4\pi}{3}}$$

$$\left[(\varepsilon_{\nu tl}-\varepsilon_{\nu tl'})\int_0^{S_t}\phi_{\nu tl'}(x)x\phi_{\nu tl}(x)x^2dx\right]G$$

$$-\frac{\hbar^2}{2m_e}S_t^2\left[S_t\phi_{\nu tl}(S_t)\phi'_{\nu tl'}(S_t)-S_t\phi_{\nu tl'}(S_t)\phi'_{\nu tl}(S_t)-\phi_{\nu tl'}(S_t)\phi_{\nu tl}(S_t)\right]G \tag{4.68}$$

$$\langle\phi_{\nu L'}(\mathbf{r})\mid v\mid\dot{\phi}_{\nu L}(\mathbf{r})\rangle=\frac{i^{l-l'-1}}{\hbar}\sqrt{\frac{4\pi}{3}}\times$$

$$\left[\int_0^{S_t}\phi_{\nu tl'}(x)x\phi_{\nu tl}(x)x^2dx+(\varepsilon_{\nu tl}-\varepsilon_{\nu tl'})\int_0^{S_t}\phi_{\nu tl'}(x)x\dot{\phi}_{\nu tl}(x)x^2dx\right]G$$

$$-\frac{\hbar^2}{2m_e}S_t^2\left[S_t\dot{\phi}_{\nu tl}(S_t)\phi'_{\nu tl'}(S_t)-S_t\phi_{\nu tl'}(S_t)\dot{\phi}'_{\nu tl}(S_t)-\phi_{\nu tl'}(S_t)\dot{\phi}_{\nu tl}(S_t)\right]G \tag{4.69}$$

$$\langle\dot{\phi}_{\nu L'}(\mathbf{r})\mid v\mid\phi_{\nu L}(\mathbf{r})\rangle=\frac{i^{l-l'-1}}{\hbar}\sqrt{\frac{4\pi}{3}}\times$$

$$\left[(\varepsilon_{\nu tl}-\varepsilon_{\nu tl'})\int_0^{S_t}\dot{\phi}_{\nu tl'}(x)x\phi_{\nu tl}(x)x^2dx-\int_0^{S_t}\phi_{\nu tl'}(x)x\phi_{\nu tl}(x)x^2dx\right]G$$

$$-\frac{\hbar^2}{2m_e}S_t^2\left[S_t\phi_{\nu tl}(S_t)\dot{\phi}'_{\nu tl'}(S_t)-S_t\dot{\phi}_{\nu tl'}(S_t)\phi'_{\nu tl}(S_t)-\dot{\phi}_{\nu tl'}(S_t)\phi_{\nu tl}(S_t)\right]G \quad (4.70)$$

$$\langle\dot{\phi}_{\nu L'}(\mathbf{r})\mid v\mid\dot{\phi}_{\nu L}(\mathbf{r})\rangle=\frac{i^{l-l'-1}}{\hbar}\sqrt{\frac{4\pi}{3}}\times$$

$$\left[\int_0^{S_t}\dot{\phi}_{\nu tl'}(x)x\phi_{\nu tl}(x)-\int_0^{S_t}\phi_{\nu tl'}(x)x\dot{\phi}_{\nu tl}(x)+(\varepsilon_{\nu tl}-\varepsilon_{\nu tl'})\int_0^{S_t}\dot{\phi}_{\nu tl'}(x)x\dot{\phi}_{\nu tl}(x)\right]x^2dxG$$

$$-\frac{\hbar^2}{2m_e}S_t^2\left[S_t\dot{\phi}_{\nu tl}(S_t)\dot{\phi}'_{\nu tl'}(S_t)-S_t\dot{\phi}_{\nu tl'}(S_t)\dot{\phi}'_{\nu tl}(S_t)-\dot{\phi}_{\nu tl'}(S_t)\dot{\phi}_{\nu tl}(S_t)\right]G \quad (4.71)$$

So by solving the above equations, the optical matrix elements can be found.

Chapter 5

Optical Properties

5.1 Introduction

There are two important factors in the Kubo formula for imaginary part of dielectric function $\epsilon_2(\omega)$. One is joint density of states,

$$N(E,\omega) = N_v(E)N_c(\hbar\omega + E) \tag{5.1}$$

This is related to

$$\int d\bar{k}\delta(E_c - E_v - \hbar\omega) = \int \frac{d\mathbf{S}}{|\bar{\nabla}(E_c - E_v)|} \tag{5.2}$$

The various peaks in $\epsilon_2(\omega)$ comes from the joint density of states for values of E_c & E_v at which slopes of valence band and conduction band are equal (Von Hove singularities). This occurs at high symmetry points in the Brillounin zone. For other values where slope $\nabla E_c \neq \nabla E_v$, transitions may occur at any general points in Brillouin zones.

The other factor is the "square of the optical matrix elements" (transition probabilities or electron photon interaction matrix elements). This is a difficult factor to be interpreted accurately. This quantity depends on the many body wavefunction and so, many body po-

tentials. For alkali metals, this accounts for about one-half of the strength of the interband absorption [219]. The other one half of the absorption accounts for many-electron effects [220]. In almost all the works/literature, there is no explicit calculation of this quantity to see its effect on optical absorption of chalcopyrite semiconductors. The observed or calculated absorption co-efficient/imaginary part of the dielectric function are generally interpreted as transition from various critical points. Therefore majority of the work correlate ϵ_2 with joint density of states.

Hobbs et.al. [214] have explicitely given a theory for the calculation of ϵ_2 within the frame work of TB-LMTO. They have defined the expression for optical matrix elements (OME) in terms of TB-LMTO orbitals. We have applied this formulation to calculate the optical matrix elements explicitly for the systems under study. The optical matrix elements depend also on the polarization of incoming photon. Since chalcopyrite system shows anisotropic nature because of its tetragonal structure, we expect optical properties to be different along the c-axis and $\perp$ to c-axis. This variation purely comes from the optical matrix elements. Thus to show the anisotropic nature, it is necessary to calculate OME parallel and perpendicular to c-axis. We have carried out such analysis for few systems.

We have shown and discussed in detail in chapter III that the chalcopyrite semiconductor's electronic properties strongly depend on p-d hybridization and structural distortion in comparison to their binary analogs. We have seen that not only there is change in band gap, but the overall density of states also change due to these effects. Therefore we expect the effect of p-d hybridization and structural distortion on optical properties via JDOS as well. We also expect these effects come from the OME. OME also depends on the crystal potential. Therefore we have also calculated OME with and without p-d hybridization and structural distortion for few systems.

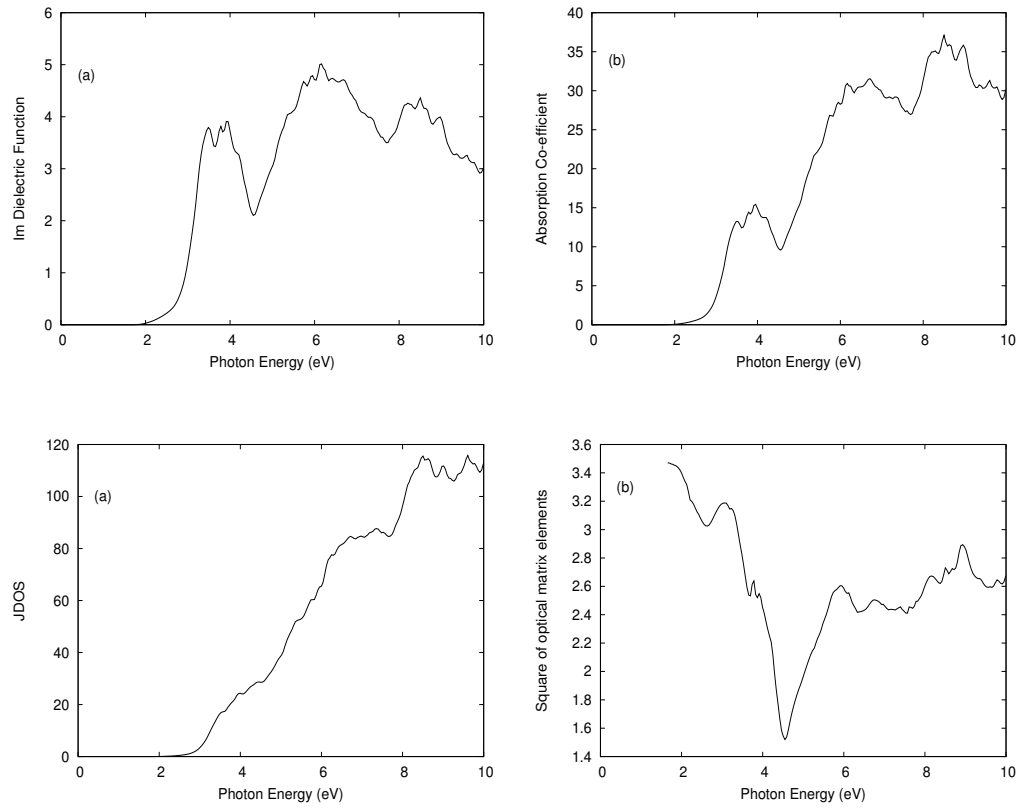

Figure 5.1: $CuIn_2S_4$: (Top panel) (a) imaginary part of the dielectric function (b) Absorption co-efficient. (Bottom panel) (a) joint density of states (JDOS) (b) Square of optical matrix elements .

For suitable applications, it is always tried to tailor the physical properties of semiconductors by suitable doping/substitutions. This kind of work and results we have presented in chapter III to show the effects on electronic properties due to substitution. Here also we have considered few defect and substituted systems to show the change in optical properties due to substitution by some particular dopants.

5.2 Effect of JDOS and OME on optical properties

The imaginary part of dielectric function, optical matrix elements and the joint density of states can be calculated by performing an integration over the Brillouin zone (k-space integration). For all these calculation, the tetrahedron method is used within TB-LMTO formalism. In this method, the dielectric function is expressed as an integral over the constant-energy surface , $E_c(k) - E_v(k)$. The eigen values and eigen vectors are then calculated on a mesh in the irreducible Brillouin zone. This zone is devided in to tetrahedra of equal volume and the mesh of k-points (maximum 512 points) defines the corners of each tetrahedron. The interpolated function is continious at the boundaries of the tetrahedra. The irreducible Brillouin zone is completely divided into tetrahedra. To calculate different necessary formulae for optical properties, the output data from the TB-LMTO band structure calculations is used.

Let us take the case of $CuIn_2S_4$. We have considered only the average values of JDOS, OME, ϵ_2 etc for this system. Figure 5.1(a) (bottom panel) shows that the structures in JDOS are reflected in ϵ_2 (figure 5.1(a) (top panel)). For example, the first peak in JDOS at around 3.5 eV has corresponding peak in ϵ_2 at the same position. But it is also clear from these figures that ϵ_2 has more structures including a valley at 4.5 eV. This valley does not appear in JDOS. The valley is due to the contribution from OME (figure 5.1(b) (bottom panel)). JDOS near the band gap is very low and increases linearly with photon energy . But ϵ_2 has a high peak at 3.5 eV then a valley at 4.5 eV. Again it has a peak at around 6.2 eV and finally another small valley and a peak at energy around 7.8 eV and 8.5 eV respectively. These structures are due to OME. Figure 5.1(b) (bottom panel) shows OME is maximum near the band edge. It drops down significantly at 4.5 eV and then oscillate

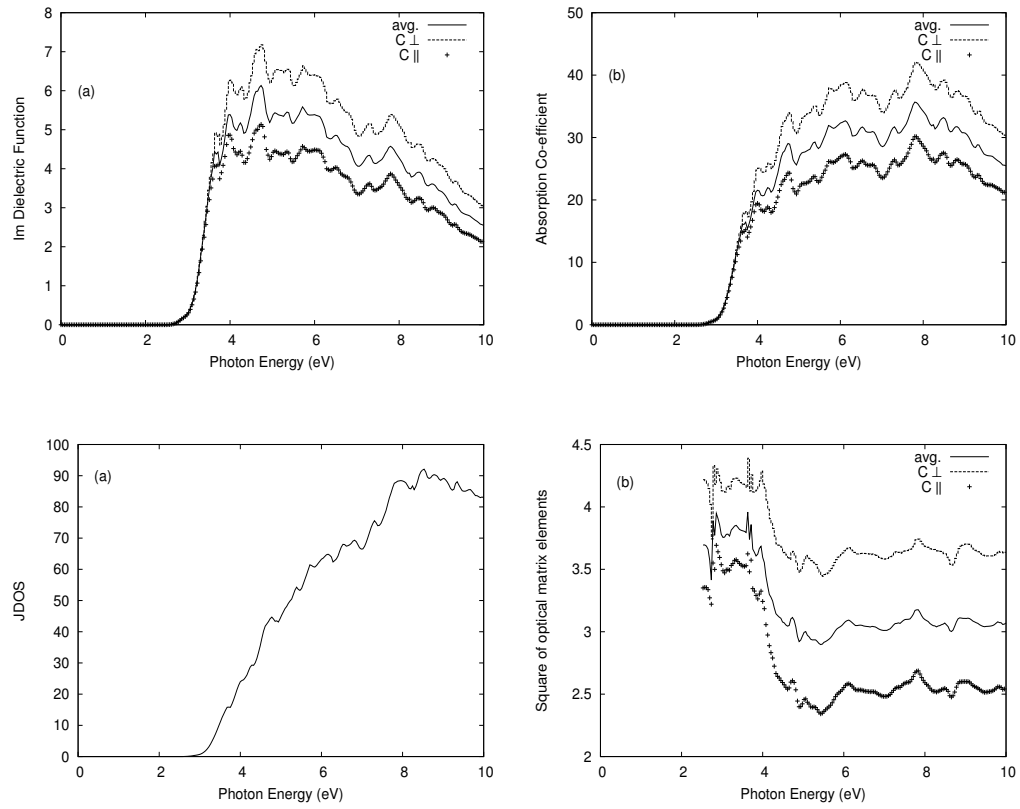

Figure 5.2: $CdAl_2Se_4$: (Top panel) (a) imaginary part of dielectric function (b) absorption co-efficient. (Bottom panel) (a) joint density of states (JDOS) (b) square of optical matrix elements

around 2.6. Thus probability of optical transition is maximum from upper valence band to the lower conduction band, though JDOS is low for such transition. Therefore first absorption peak mainly comes from OME contribution.

Figure 5.2(a) (top panel) and figure 5.3(a) (top panel) show that the higher peaks in ϵ_2 are at 4.5 eV and 3.0 eV respectively in case of CdX_2Se_4 (X = Al, Ga). There is a sharp valley in ϵ_2 at energy 4.0 eV in case of $CdGa_2Se_4$. At the same energy a sharp valley is also found in OME (figure 5.3(b) (bottom panel) in this system. But we have not found such type of structure neither in OME nor in ϵ_2 in case of $CdAl_2Se_4$. This shows the strong dependence of ϵ_2 on OME. The first peak in ϵ_2 in $CdGa_2Se_4$ (figure 5.3(a) (top

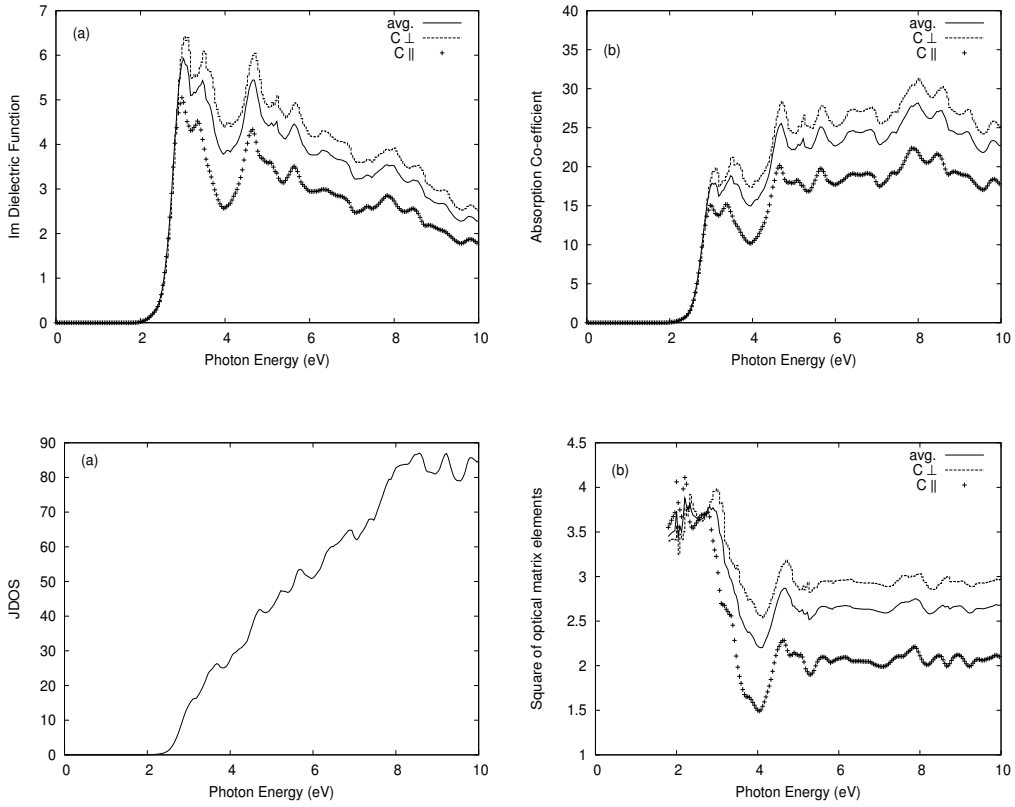

Figure 5.3: $CdGa_2Se_4$: (Top panel) (a) imaginary part of dielectric function (b) absorption co-efficient. (Bottom panel) (a) joint density of states (JDOS) (b) square of optical matrix elements

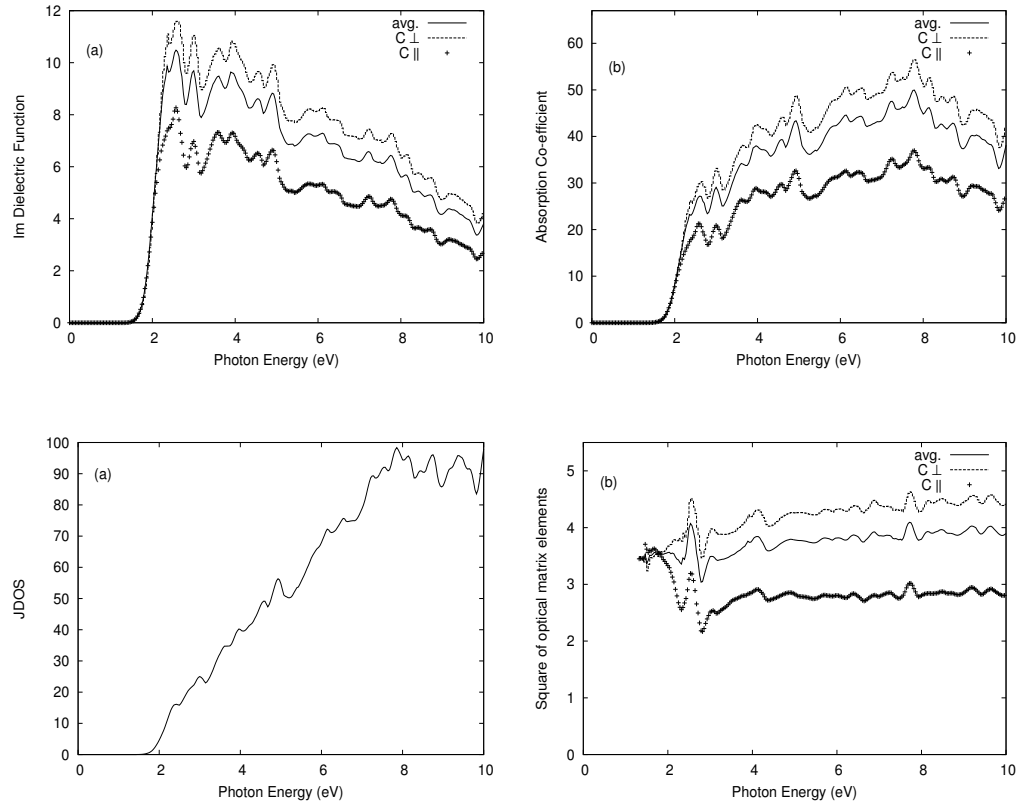

Figure 5.4: $CdGa_2Te_4$: (Top panel) (a) imaginary part of dielectric function (b) absorption co-efficient. (Bottom panel) (a) joint density of states (JDOS) (b) square of optical matrix elements.

panel)) is highest because in this case peaks in JDOS and OME are at the same energy.

Figure 5.4(a) (top panel) shows that the highest peak in ϵ_2 comes at energy 2.5 eV in the case of $CdGa_2Te_4$. A close comparison between figure 5.4(a) (top panel) and figure 5.4(b) (bottom panel) show that structures in ϵ_2 between 2.5-3.5 eV are due to similar structure in OME in the same energy range. JDOS is increasing linearly with photon energy as shown in figure 5.4(a) (bottom panel). There is a highest peak at energy 3.5 eV in ϵ_2 as shown in figure 5.5(a) (top panel) in case of $CdIn_2Te_4$. This is due to the contribution of JDOS as shown in figure 5.5(a) (bottom panel). A sudden fall

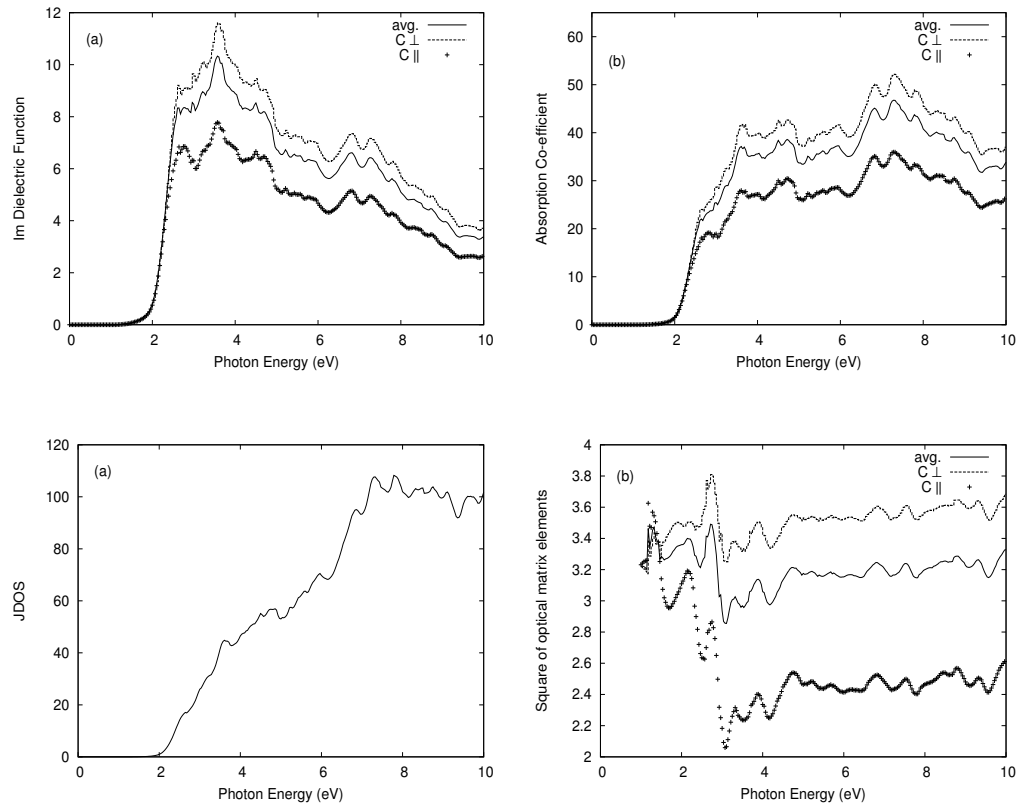

Figure 5.5: $CdIn_2Te_4$: (Top panel) (a) imaginary part of dielectric function (b) absorption co-efficient. (Bottom panel) (a) joint density of states (JDOS) (b) square of optical matrix elements.

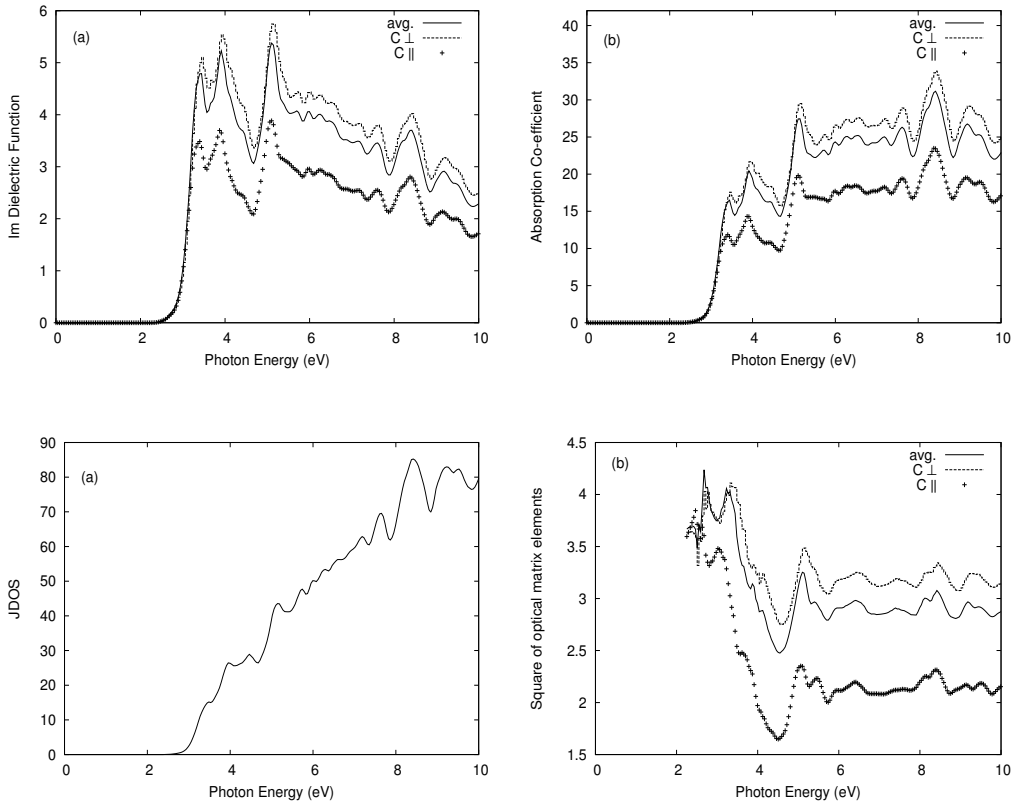

Figure 5.6: $CdGa_2S_4$: (Top panel) (a) imaginary part of dielectric function (b) absorption co-efficient. (Bottom panel) (a) joint density of states (JDOS) (b) square of optical matrix elements.

in OME is seen at 3.0 eV (figure 5.5(b) (bottom panel)). This figure shows that OME oscillates at around the value 2.4. ϵ_2 is highly dependent on JDOS in this system. Figure 5.6(a) (top panel) and figure 5.6(a)(bottom panel) show that the first two peaks in ϵ_2 and corresponding in JDOS have the same positions in the case of $CdGa_2S_4$. There is a sharp drop in ϵ_2 at energy 4.5 eV. This is because of the contribution from OME. The drop in OME, as shown in figure 5.6(b)(bottom panel) at the same energy is 3/4 times than ϵ_2. Similar picture we observe also in case of $AgAl_2Se_4$. Figure 5.7(a)(top panel) shows that the first two peaks in ϵ_2 reflect the peaks in JDOS (figure 5.7(a)(bottom panel). The figure 5.7(a)(bottom panel) shows JDOS increases almost linearly between energy

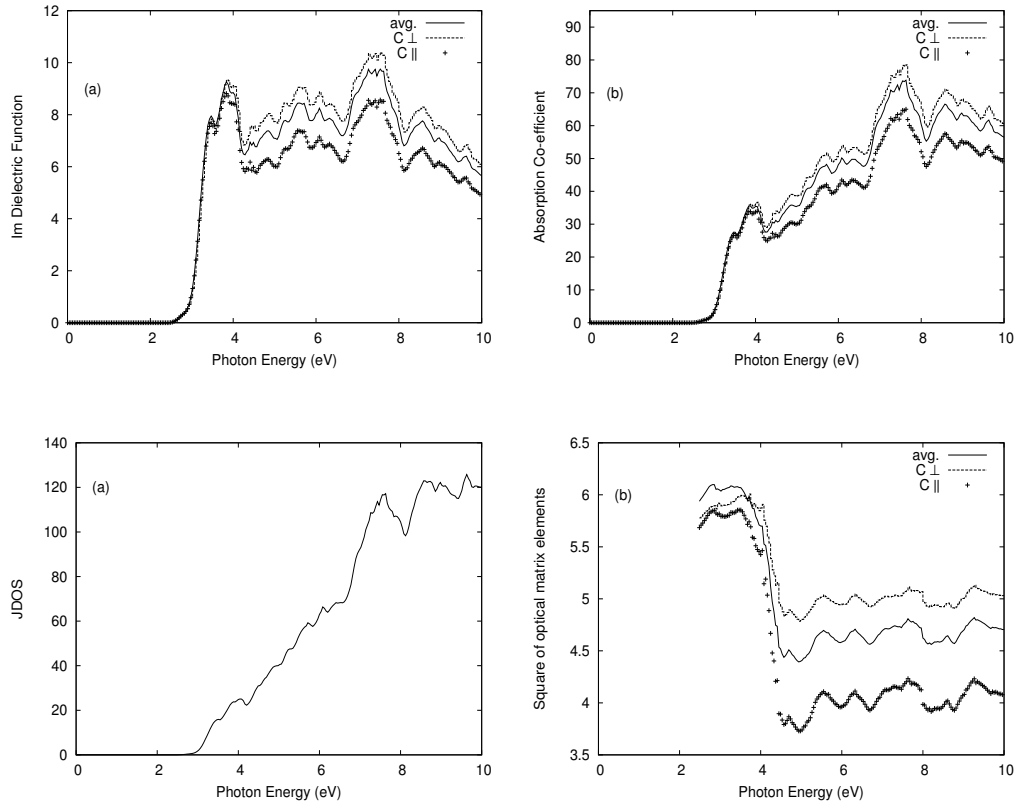

Figure 5.7: $AgAl_2Se_4$: (Top panel) (a) imaginary part of dielectric function (b) absorption co-efficient. (Bottom panel) (a) joint density of states (JDOS) (b) square of optical matrix elements.

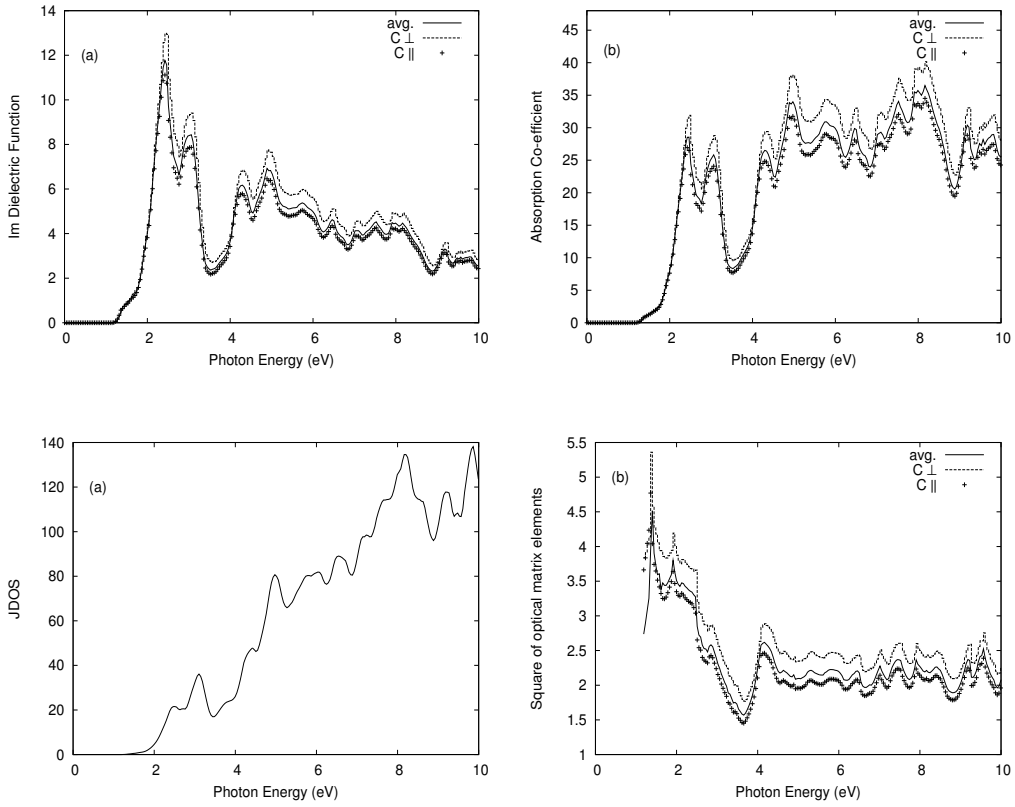

Figure 5.8: $CuNaIn_2S_4$ (Top panel) (a) imaginary part of dielectric function (b) absorption co-efficient. (Bottom panel) (a) joint density of states (JDOS) (b) square of optical matrix elements.

4.2-6.7 eV. But there are structures in ϵ_2. These structures are due to the oscillation in OME around the value 4.5 as shown in figure 5.7(b)(bottom panel). But there is a peak in ϵ_2 at energy 7.5 eV. This peak comes from the contribution of JDOS. Similar study we have also carried out for few substituted systems.

In case of $CuNaIn_2S_4$, figure 5.8(a) (bottom panel) shows a small peak at energy 2.5 eV and a relatively bigger peak at 3.0 eV in JDOS. Whereas the corresponding peaks in ϵ_2, as shown in figure 5.8(a) (top panel) are reversed. This is again due to the effect of OME. Figure 5.8(b) (bottom panel) shows that OME drastically goes down between

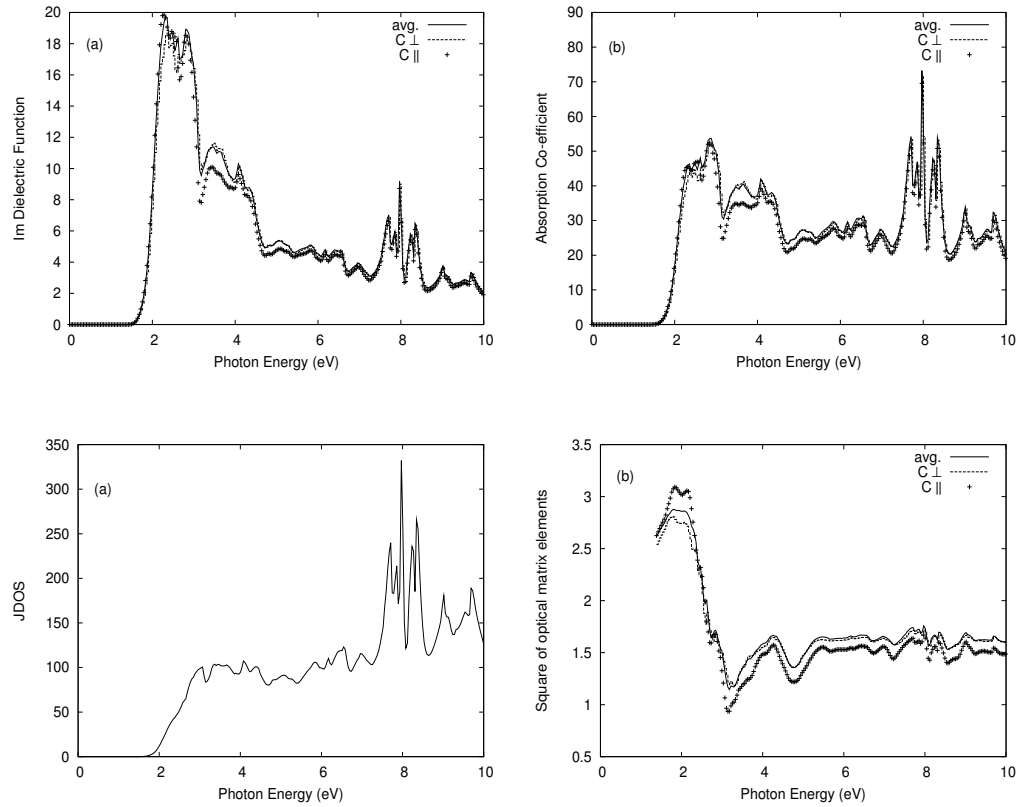

Figure 5.9: $ZnMnIn_2Te_4$: (Top panel) (a) imaginary part of dielectric function (b) absorption co-efficient. (Bottom panel) (a) joint density of states (JDOS) (b) square of optical matrix elements.

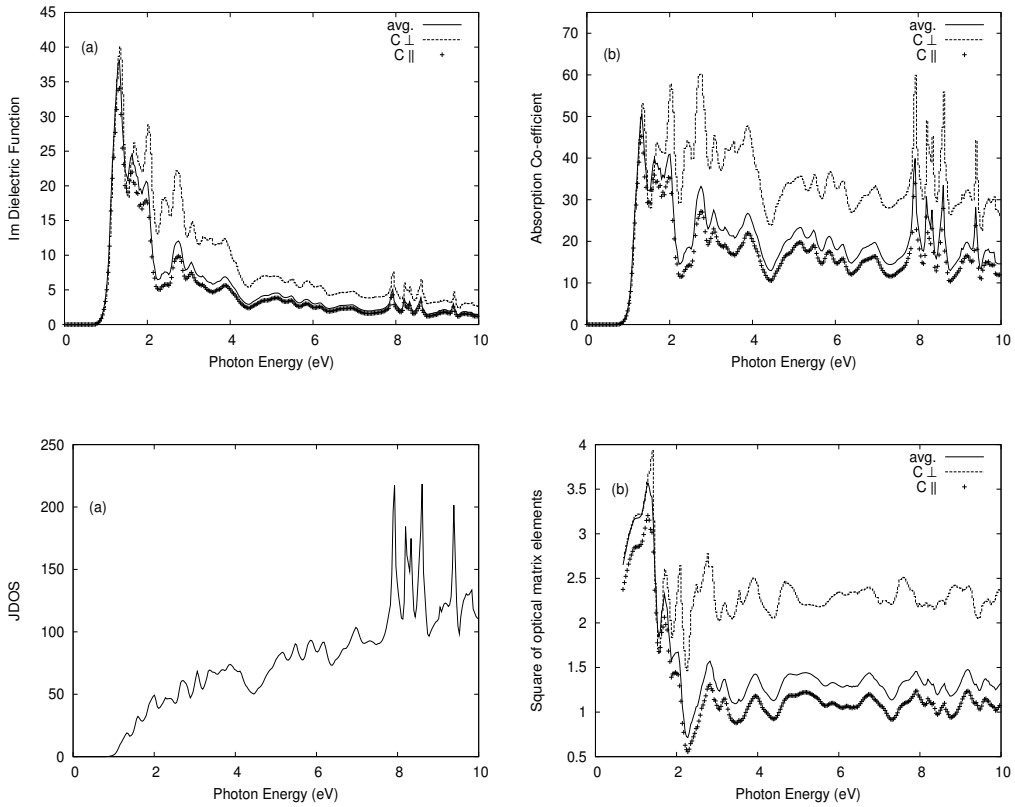

Figure 5.10: $ZnOIn_2Te_4$: (Top panel) (a) imaginary part of dielectric function (b) absorption co-efficient. (Bottom panel) (a) joint density of states (JDOS) (b) square of optical matrix elements

2.0 to 4.0 eV. It is lowest at energy 3.5 eV. A deep valley is observed in ϵ_2 at the same energy. Two small peaks are seen in ϵ_2 at 4.2 and 5.0 eV. The first small peak comes from the contribution of both JDOS and OME. The second one comes from JDOS only. Figure 5.8(b) (bottom panel) shows OME oscillates about the value 2 after energy 5.0 eV

.

Figure 5.9(a) (top panel)) shows the first peak in ϵ_2 comes from the contribution of OME (figure 5.9(b) (bottom panel)). The second peak is due to JDOS as shown in figure 5.9(a) (bottom panel) in the case of $ZnMnIn_2Te_4$. There is a sudden fall in ϵ_2 at energy 3.1 eV. This is because of the sharp drop in JDOS and OME at the same energy. The structures between energy range 7.5-8.5 eV come from the contribution of JDOS. Figure 5.9(a) (bottom panel) shows OME is lowest at energy 3.1 eV. Like in the case of $CuNaIn_2S_4$, OME oscillates around 1.5 after energy 5.0 eV in this system also.

Figure 5.10(a) (top panel)) shows that the first two peaks in ϵ_2 come from the contribution from JDOS (figure 5.10(a) (bottom panel)) in the case of $ZnOIn_2Te_4$. There is a deep valley at energy 2.2 eV in ϵ_2. This is because similar structure of magnetude 0.5 is found in OME at the same energy as shown in figure 5.10(b) (bottom panel). The structures present in ϵ_2 between the energy range 7.5-9.0 eV are due to the contribution from JDOS. Figure 5.10(b) (bottom panel), OME oscillates around the value 1.0 after energy 3.5 eV. As the photon energy increases, $1/\omega^2$ dominates in ϵ_2 with some oscillation in all the systems. This oscillation is due to oscillations in OME around some constant value.

5.2.1 Anisotropic Nature

We have explicitely calculated the optical properties and OME for photon polarization along c and $\perp$ to c-axis as well as the avrage value $\left(\frac{\epsilon_{2x}+\epsilon_{2y}+\epsilon_{2z}}{3}\right)$ for the systems $CuIn_2S_4$, CdX_2Se_4 (X = Al. Ga), CdY_2Te_4 (Y = Ga, In), $CdGa_2S_4$, $AgAl_2Se_4$, $CuNaIn_2S_4$ and $ZnXIn_2Te_4$ (X = Mn, O). All the figures for various optical response functions show significant anisotropic nature in these properties. The properties get enhanced when photon is polarized perpendicular to c-axis. The figures of OME (figure 5.2 - 5.10(b) (bottom panel) for all the systems, show that the probability of transition is more perpendicular to c-axis.

5.2.2 Effect of Structural distortion:

To show the effect of structural distortion on optical propertoes, we have calculated the average value of ϵ_2 and OME with p-d hybridization for ideal and non-ideal structures. We have only considered three systems, namely $AgAl_2Se_4$, $CuIn_2S_4$ and $CuNaIn_2S_4$. Let us take the case of $CuIn_2S_4$. Figure 5.1(b) (bottom panel) (non-ideal) and figure 5.11(b) (top panel) show that OME increases by more than two factor in the case of non-ideal compared to ideal structure. These figures show significant differences in the structures in OME for non-ideal and ideal cases. Secondly, the depth of the valley in non-ideal case is quite large compared to the ideal one. One more difference is observed between this two cases that strudtures in OME shifts towards higher energy in ideal case compared to non-ideal case. Because of this change in OME, ϵ_2 shows two broad peaks at 4.0 eV and 6.5 eV in non-ideal structure. Whereas there are no broad peaks in ideal case but little oscillation around 1.2-1.4 value. At the same time, the magnitude of ϵ_2 is enhanced by

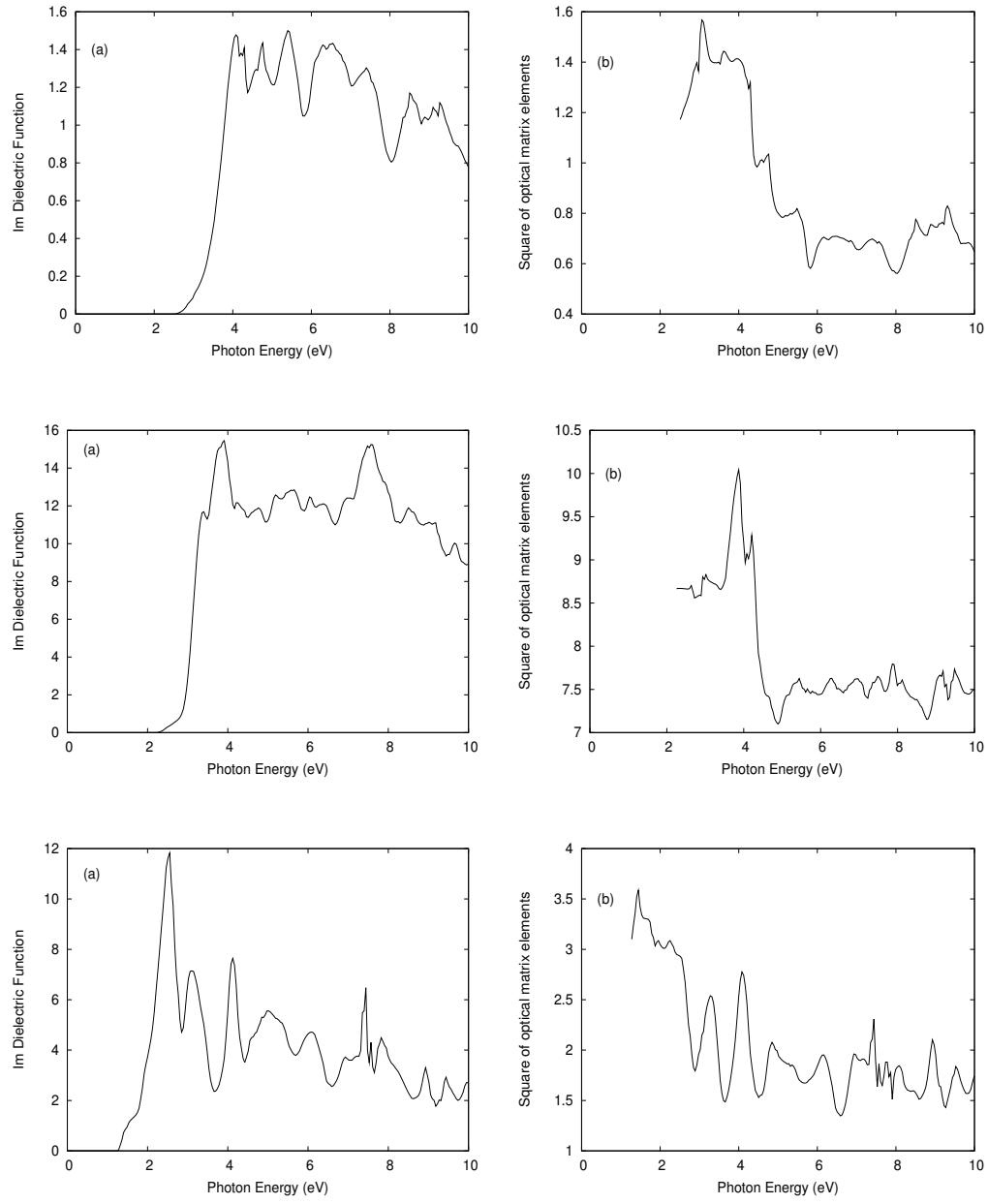

Figure 5.11: For ideal case with hybridization (a) ϵ_2 (b) OME : (top panel) $CuIn_2S_4$, (middle panel) $AgAl_2Se_4$ and (bottom panel) $CuNaIn_2S_4$.

almost 4 times due to structural distortion. As we discussed in chapter III, there is indeed change in TDOS due to structural distortion. So we expect changes in JDOS also. But main effect in ϵ_2 comes from OME.

Similar pictures arise in the case of $AgAl_2Se_4$ also. Comparing figure 5.7(a) (top panel) and figure 5.11(a) (middle panel), it is clear that the first major peak in ϵ_2 reduced from 15.5 unit to 9.5 unit due to structural distortion. This is mainly due to the reduction in OME from 10 to 6 unit which is found by comparing figure 5.7(b) (bottom panel) and figure 5.11(b) (middle panel).

All the above results shown are the effect in defect systems. If we see the effect of structural distortion in $CuNaIn_2S_4$, we find this effect is not prominent. Figures 5.8(b) (bottom panel) and 5.11(b) (bottom panel) show there is indeed changes in the structure in OME due to structural distortion. But the figure 5.8(a) (top panel) and figure 5.11 (bottom panel)) show the net effect in ϵ_2 is not prominent for lower energy (below 4eV). There is some change in ϵ_2 above 4.0 eV. This means that the changes in JDOS is such that it neutrilizes the minor effect due to OME.

5.2.3 Effect of p-d Hybridization:

In the study of electronic properties, we observed that p-d hybridization has very significant effect in reducing the band gap and in general has significant effect in TDOS. To see the quantitative effect in optical properties also we choose the same systems as we studied for structural distortion. We have considered the ideal case of the systems to eliminate any effect due to structural distortion. We have calculated optical response functions and OME with and without p-d hybridization.

Our study of DOS in chapter III shows there is appreciable change in DOS due to hy-

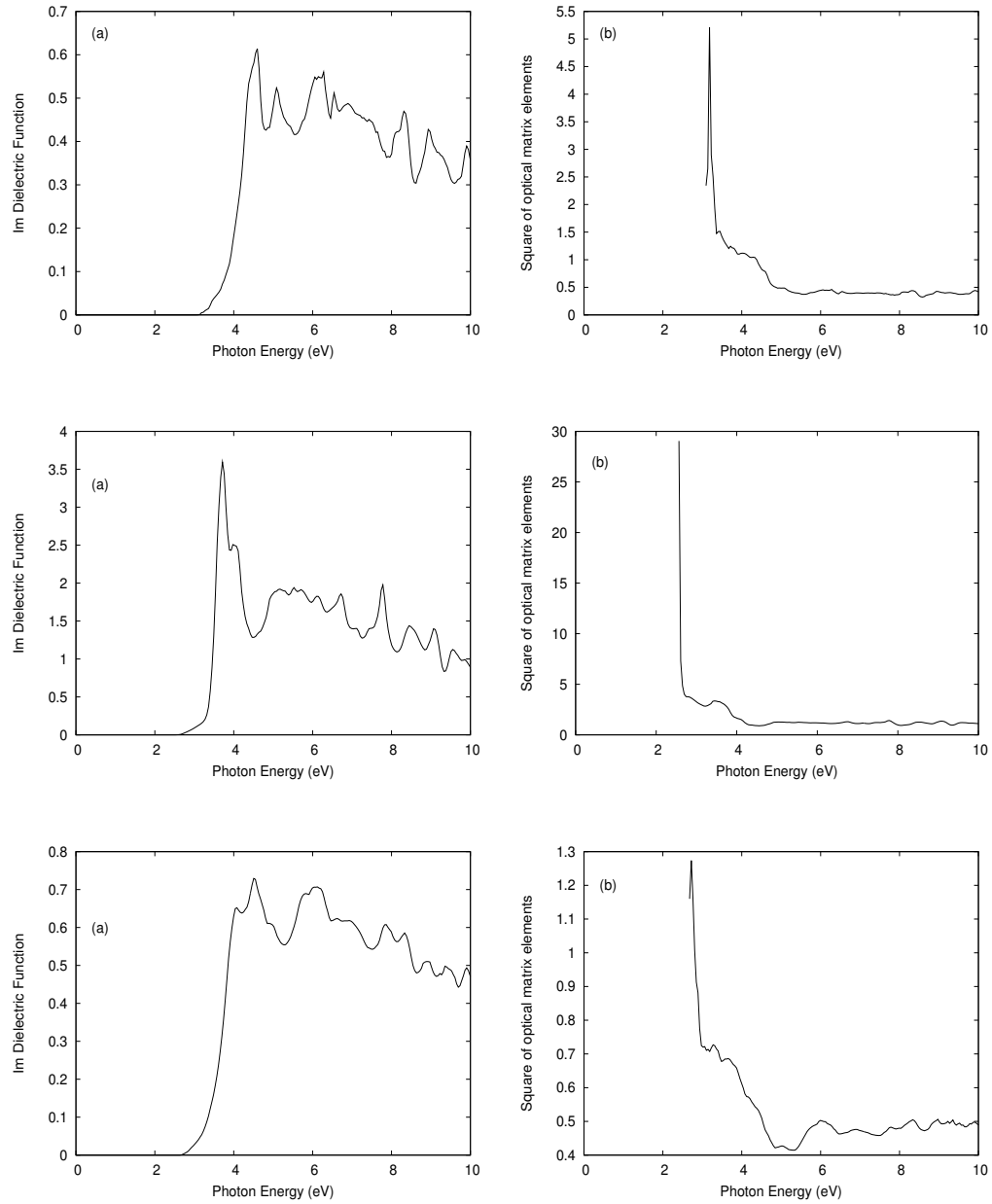

Figure 5.12: For ideal case without hybridization (a) Im dielectric function (b) square of optical matrix elements of (top panel) $CuIn_2S_4$, (middle panel) $AgAl_2Se_4$ and (bottom panel) $CuNaIn_2S_4$.

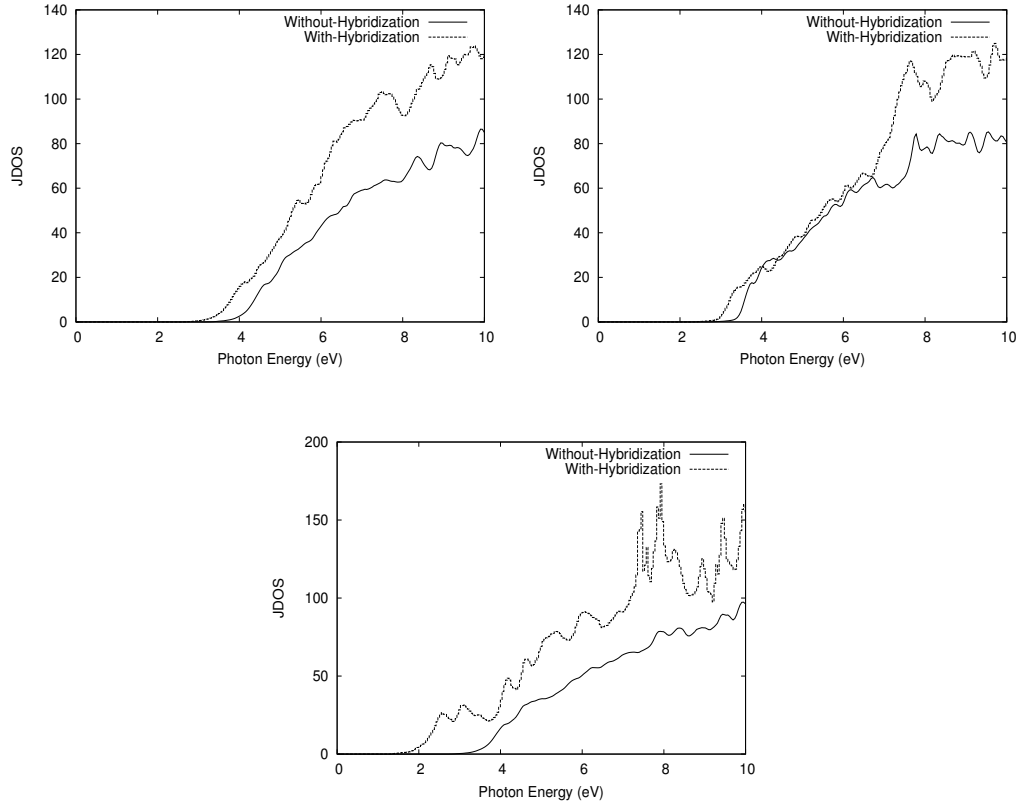

Figure 5.13: For ideal case JDOS : (left panel) $CuIn_2S_4$, (right panel) $AgAl_2Se_4$ and (bottom panel) $CuNaIn_2S_4$.

bridization. This means there is also changes in JDOS due to p-d hybridization. Our study shows even OME changes drastically. This is clear from the comparison of figures 5.12(b) (ideal without hybridization) and figure 5.11(b) (ideal with hybridization). For example figure 5.12(b)(top panel) shows there is only a delta function peak at 3 eV with a magnitude 5. But hybridization broadens this peak and many more peaks appear with reduced value (figure 5.1(b) (bottom panel)) in case of $CuIn_2S_4$. Figure 5.13 shows that the magnitude of JDOS is large due to hybridization in the case of $CuIn_2S_4$.

Comparison of the figures 5.12(b)(middle panel) and 5.11(b) (middle panel) show that the magnitude of OME is reduced by factor 3 due to hybridization in case of $AgAl_2Se_4$. Whereas there is decrement in ϵ_2 as shown in figure 5.12(a)(middle panel). This is due to the less contribution from the JDOS (figure 5.13 (right-panel)). There is a delta function peak at 2.5 eV with a magnitude 29 in this case also. But figure 5.13 shows that JDOS increases due to hybridization in case of $CuNaIn_2S_4$. Same thing is true for OME also in this case. This leads to ϵ_2 with small magnitude in the case of 'without hybridization'.

5.2.4 Other optical response functions

To calculate different optical response functions such as absorption co-efficient, refractive index etc, both imaginary and real part of dielectric functions are required. The real part of the dielectric function can be obtained from Kramers-Kronig relation [207]. Figures 5.14 and 5.16 show the real parts of dielectric function and refractive indices of AAg_2Se_4 (A = Al, Cd), $CdIn_2Te_4$ and $CdGa_2X_4$ (X = S, Se, Te) respectively. The average static dielectric constants are calculated from the figures 5.14 and 5.16. The static dielectric constant $\epsilon_1(0)$ is given by the lower energy limit of $\epsilon_1(\omega)$. The structures coming in refractive index are due to the similar structures present at the same energy in ϵ_1. The

Table 5.1: Static dielectric constant $\epsilon_1(0)$ and refractive index $n(0)$.

Systems	$\epsilon_1(0)$	$n(0)$	Systems	$\epsilon_1(0)$	$n(0)$
$AgAl_2Se_4$	9.06	3.01	$CdIn_2Te_4$	11.93	3.45
$CdAl_2Se_4$	5.82	2.41	$CuIn_2S_4$	7.30	2.70
$CdGa_2S_4$	6.85	2.61	$CuNaIn_2S_4$	8.19	2.86
$CdGa_2Se_4$	7.02	2.65	$ZnMnIn_2Te_4$	11.33	3.36
$CdGa_2Te_4$	9.87	3.14	$ZnOIn_2Te_4$	16.82	4.10

average static dielectric constants and refractive indices of the systems under study are given in table 5.1.

Figure 5.7(b)(top panel) shows that the absorption co-efficient is maximun in the energy 6.5-8.2 eV for $AgAl_2Se_4$. Figure 5.2 shows that the mangitude of absorption co-efficient is less in case of $CdAl_2Se_4$ compared to $AgAl_2Se_4$. Our calculated ϵ_1 and ϵ_2 for $CdIn_2Te_4$ agree well with the result of Ozaki et.al. [77]. We have shown their result in figure 5.15.

ϵ_1, absorption co-efficients and refractive indicies of the systems $CdGa_2X_4$ (X = S, Se, Te) are also calculated and shown in the figures 5.6(b) (top panel), 5.3(b) (top panel), 5.4(b) (top panel) and 5.16 (top panel), 5.16 (middle panel) and 5.16 (bottom panel).

We observe that the magnitude of absorption coefficient in the case of $CdGa_2Te_4$ from figure 5.4(b) (top panel) is high compared to the other two systems, $CdGa_2X_4$ (X = S, Se). Sharp vallies are found in absorption co-efficients in the case of $CdGa_2X_4$ (X = S, Se) at energy 4.6 eV and 4.0 eV respectively. But such type of structure is absent in $CdGa_2Te_4$. Ozaki et.al. [76] have carried out both theoretical and experimental study to calculate ϵ_1 and ϵ_2 for the system $CdGa_2Te_4$. Their result is shown in figure 5.17. Our

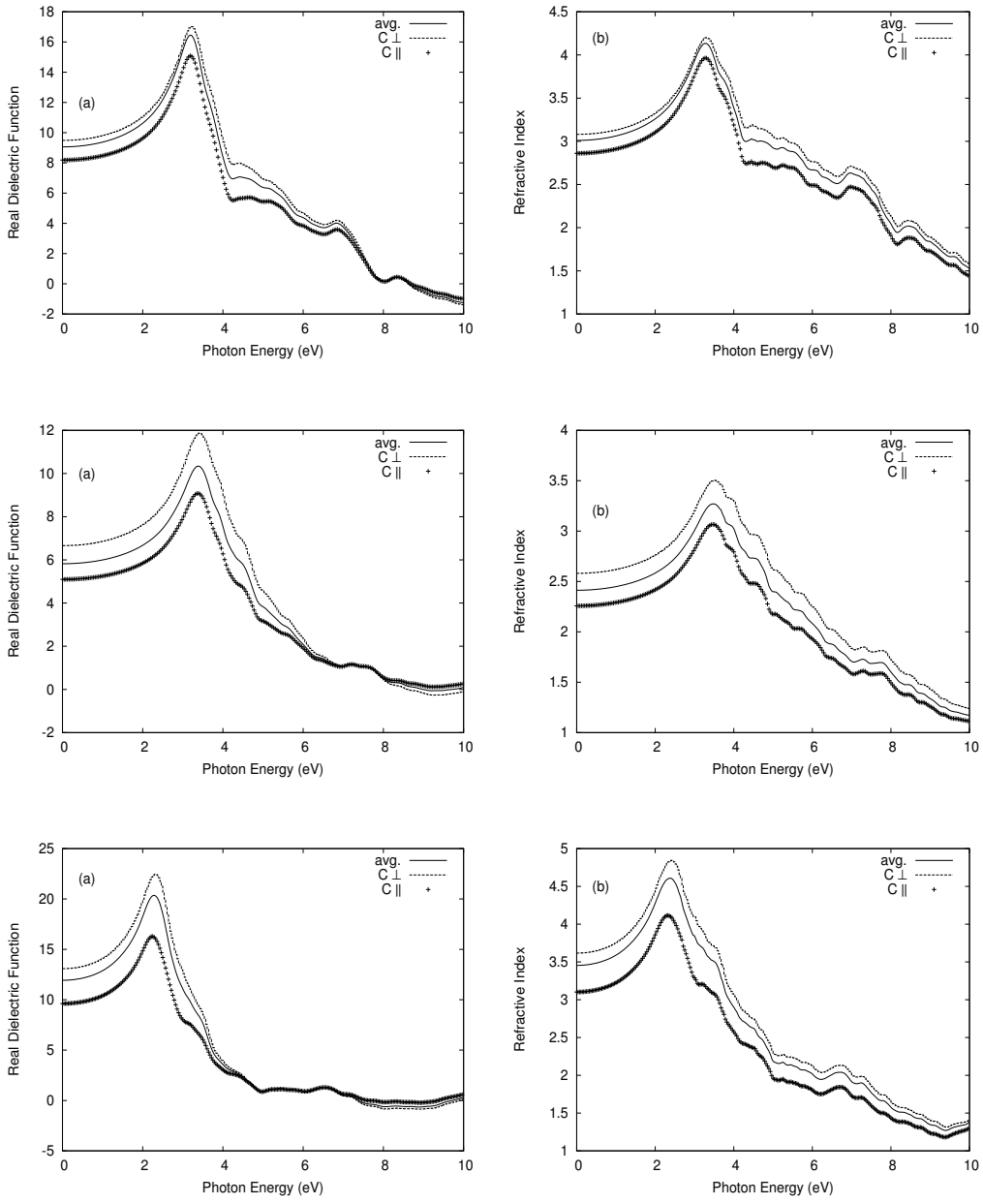

Figure 5.14: (a) real part of dielectric function (b) refractive index : (Top panel) $AgAl_2Se_4$, (middle panel) $CdAl_2Se_4$ and (bottom panel) $CdIn_2Te_4$.

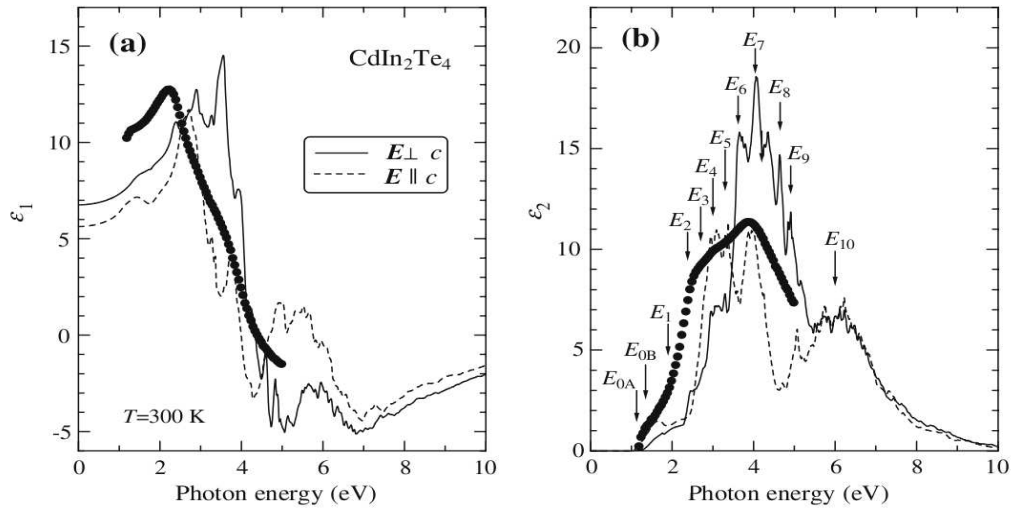

Figure 5.15: Solid circles show the experimental result (spectroscopic ellipsometry (SE)) [77] and the solid and dashed lines represent the calculated result of $CdIn_2Te_4$ [77] : (a) imaginary part of dielectric function (b) real part of dielectric function.

calculated result for this system also agrees quite well with their result.

5.2.5 Effect of substitution on optical response functions

We have already discussed in the introduction that AB_2C_4 are defect systems. They can be doped with impurities to tailor various properties. Let us consider the case of $CuNaIn_2S_4$. This is the system where Na is substituted at vacancy position in $CuIn_2S_4$. Therefore it is a good candidate whose properties can be compared with the defect system. If we compare ϵ_2 of both the systems (figure 5.1 (a) (top panel) and figure 5.8 (a) (top panel)), we observe that the first broad peak in $CuIn_2S_4$ is splitted into two sharp peaks. In $CuIn_2S_4$, all the peaks and vallies in ϵ_2 are broad and prominent whereas in case of $CuNaIn_2S_4$, it is just the reverse. This is because large number of structures are found in JDOS in the case of $CuNaIn_2S_4$ (figure 5.8(a) (bottom panel). Figure 5.1(a) (top panel)

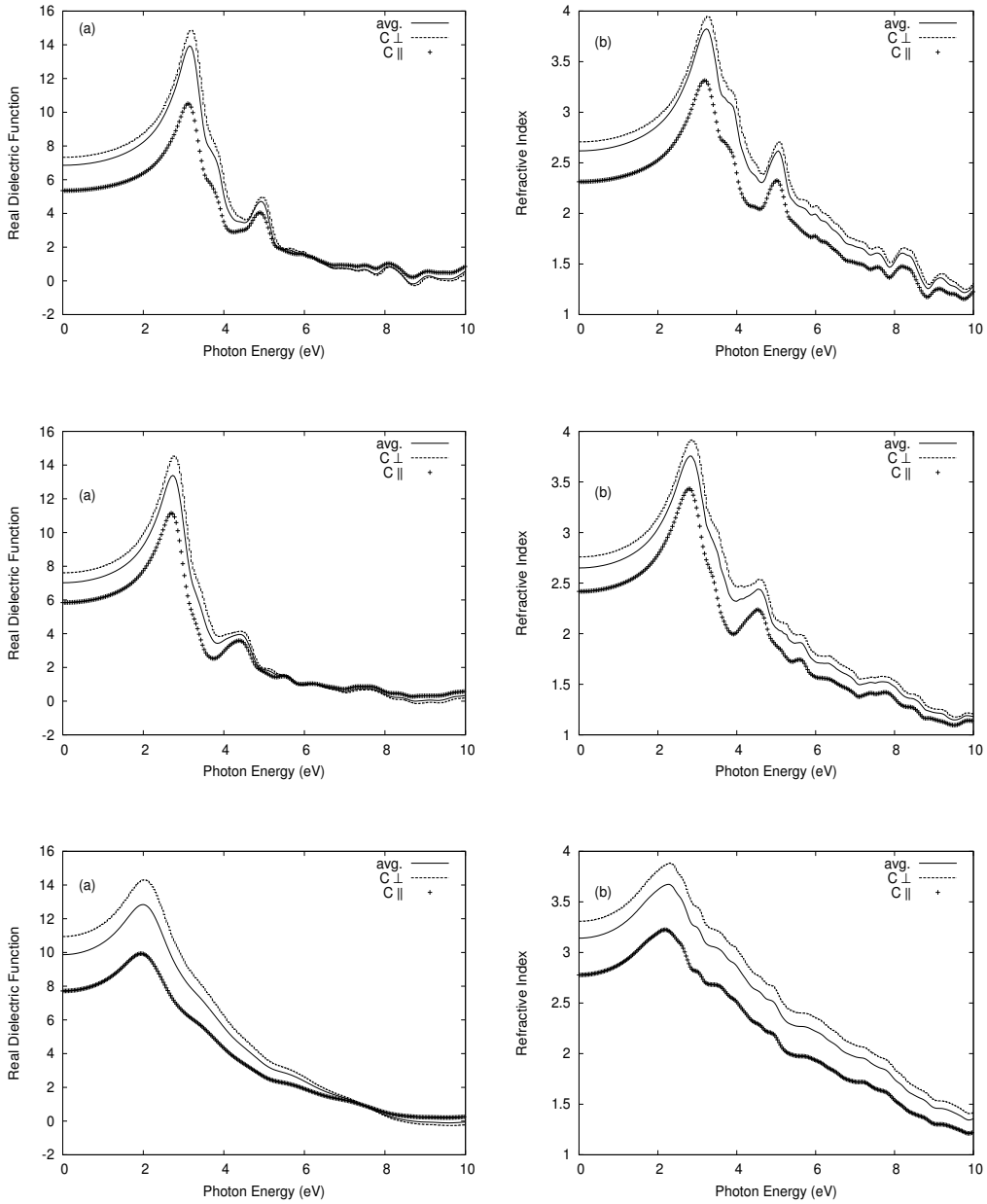

Figure 5.16: (Top panel) $CdGa_2S_4$: (a) real part of dielectric function (b) refractive index. (Middle panel) $CdGa_2Se_4$: (a) real part of dielectric function (b) refractive index. (Bottom panel) $CdGa_2Te_4$: (a) real part of dielectric function (b) refractive index.

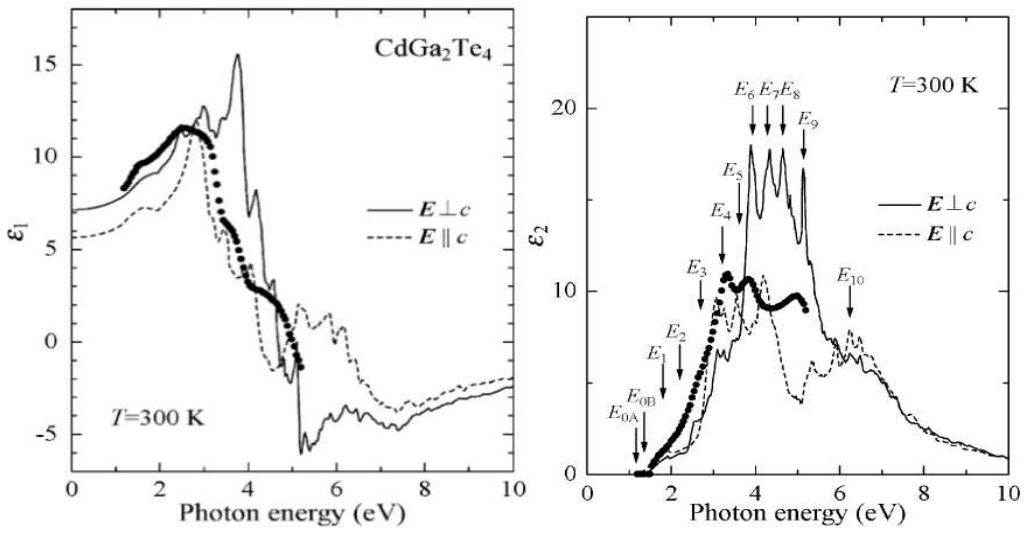

Figure 5.17: Solid circles show the experimental result (spectroscopic ellipsometry (SE)) [76] and the solid and dashed lines represent the calculated result of $CdGa_2Te_4$ [76] : (a) imaginary part of dielectric function (b) real part of dielectric function.

shows that the sharp valley found in ϵ_2 at energy 4.5 eV in the case of $CuIn_2S_4$ shifts towards the lower energy at 3.5 eV in case of $CuNaIn_2S_4$ (figure 5.8(a) (top panel)). Table 5.1 shows that there is significant differences in static dielectric constants and refractive indices between these two systems. The refractive index reaches a maximum value of about 2.85 and 2.70 at energy 2.5 and 3.5 eV in the cases of $CuNaIn_2S_4$ and $CuIn_2S_4$ respectively (figure 5.18(a)(bottom panel) and figure 5.18(a)(top panel).

Ganguli et.al. [147] have calculated the optical properties of $ZnIn_2Te_4$ defect chalcopyrite using TB-LMTO method. They have compared the imaginary part and real part of dielectric functions with the experimental result of Ozaki and his group [75] as shown in figure 5.19). Ganguli et.al. [147] have found a good agreement of their results with Ozaki et. al.[75] results. We have also used the same TB-LMTO method for our calculation of optical properties of Mn and oxygen substituted $ZnIn_2Te_4$. Therefore we

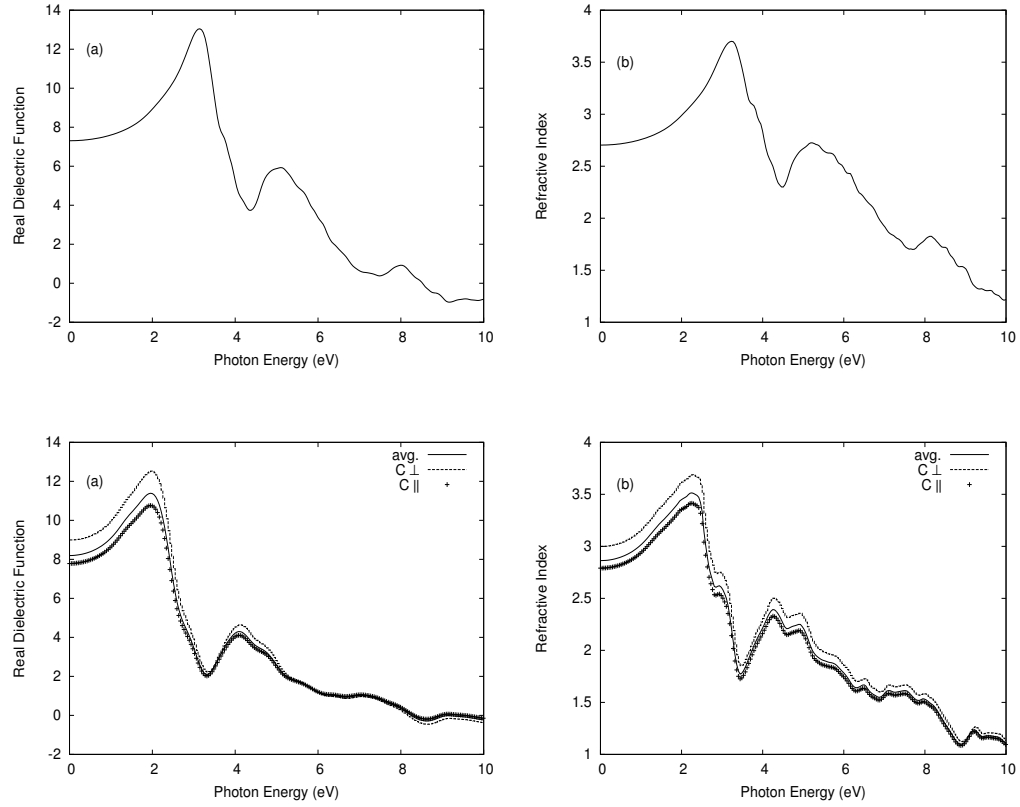

Figure 5.18: (a) real part of dielectric function (b) refractive index : (Top panel) $CuIn_2S_4$ and (Bottom panel) $CuNaIn_2S_4$.

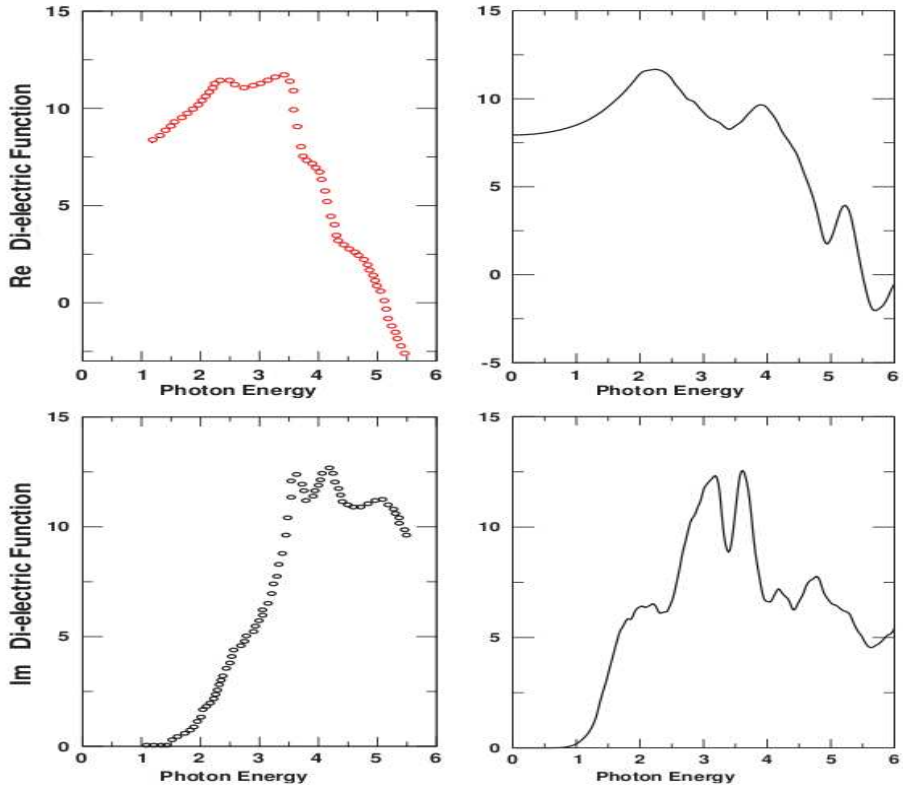

Figure 5.19: Imaginary and real part of dielectric function of $ZnIn_2Te_4$ (left panel) Experimental result (by spectroscopic ellipsometry (SE)) [75], 1st principle TB-LMTO method by Ganguli et. al. [147]

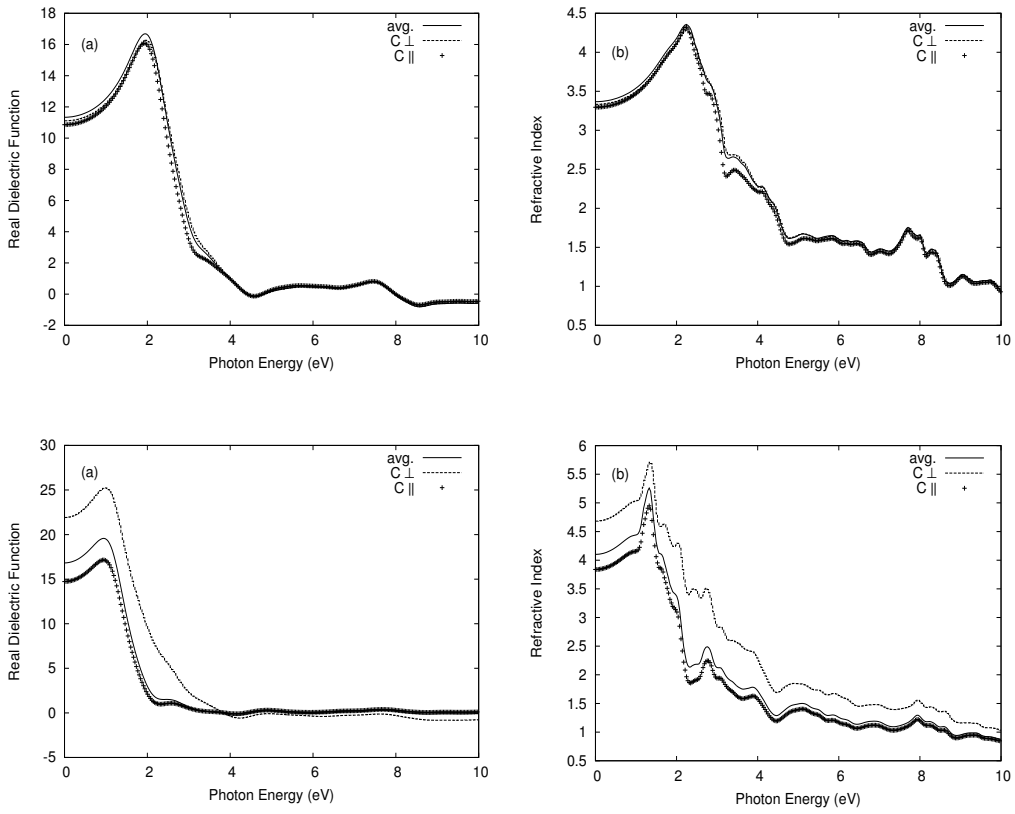

Figure 5.20: (a) real part of dielectric function (b) refractive index.(Top panel) : $ZnMnIn_2Te_4$ and (Bottom panel) $ZnOIn_2Te_4$.

compare our calculated ϵ_2 for the cases $ZnMnIn_2Te_4$ and $ZnOIn_2Te_4$ with the result of Ganguli et.al. for the case of $ZnIn_2Te_4$ to study the effect of substitution in the defect chalcopyrite. Comparing figure 5.19(right-bottom panel), figure 5.9(a) (top panel) and figure 5.10(a) (top panel), we find there is an incremnt in ϵ_2 in both Mn and oxygen substituted cases compared to $ZnIn_2Te_4$. Similar picture we may expect in case of absorption co-efficients also. The static dielectric constant in case of $ZnMnIn_2Te_4$ and $ZnOIn_2Te_4$ (figure 5.20 (a) top and bottom panel) are comparatively larger than $ZnIn_2Te_4$ as seen from figure 5.19(right-top panel). So we expect similar enhancement in refractive indices of both the systems.

Chapter 6

Conclusion

In general our study of structural, electronic and optical properties of many pure, defect and substituted chalcopyrite semiconductors by DFT based first principle TB-LMTO method give satisfactory result. Our result agrees well with the available experimental and other calculated results for the systems studied by others. Our calculated band gaps are found to be lower than the expected. This is purely due to the underestimation by LDA, which is a well known fact. Considering this limitation of LDA, our results are quite accurate. We have, in general, provided quantitative calculations of the effects of p-d hybridization and structural distortion on band gaps and other electronic properties and optical properties. We have also been able to provide detailed study of linear optical properties of few defects and substituted systems. We have shown the effects of various factors like DOS, OME etc in optical properties. Therefore we have provided deeper understanding of physics of these effects. Specifically we have following important outcomes.

1. Structural parameters, such as lattice parameters, anion displacements, tetragonal distortion and bond-lengths show good agreement with the available experimental

results for systems studied by others.

2. Bulk modulus are calculated for all these systems except $ZnXIn_2Te4$ ($X = O, Mn$). Results show inversed proportionality relation between lattice parameters "a" and bulk modulus for all the systems as expected, except in the case of Cu_2InSe_4.

3. Band structure and total density of states(TDOS) of all the systems show they are direct band gap semiconductors.

4. AAl_2Se_4 (A = Ag, Cu), $CuIn_2Se_4$, $CuIn_2S_4$ and Cu_2InSe_4 are found to be p-type semiconductors. But $CdXGa_2S_4$ ($X = Ag, Al$) and $ZnXIn_2Te_4$ (O, Mn) are n-type semiconductors.

5. Band gap increases in defect chalcopyrites in comparison to their corresponding pure and substituted chalcopyrites.

6. Study of partial density of states(PDOS) reveals that the contribution to upper valance band comes from the cation d and anion p hybrid orbitals in case of group $I-III-VI_2$, $I_2-III-VI_4$, $I-III_2-VI_4$ and their substituted chalcopyrites semiconductors. This leads to strong p-d hybridizations in these cases. But in case of group $II-IV-V_2$, $II-III_2-VI_4$ and their substituted chalcopyrites, the main contribution to upper valance band comes from the anion p states. Cation d states behave like core states in these types of compound and contribute to inner valance band. Therefore they do not participate in p-d hybridization. Major contributions come from the anion p states to the conduction band.

7. We have found significant effect of p-d hybridization on band gap reduction in $ZnSnX_2$ ($X = P, As, Sb$). but the same is not found in other systems in the same

group ($II - IV - V_2$).

8. The quantitative estimate of the effects of p-d hybridization on band gap shows that the $\%$ of band gap reduction is more in case of the pure chalcopyrites compared to their corresponding defect chalcopyrites.

9. Though Li & Na do not have d orbitals contribution to upper valence band, they act like catalyst in reducing the band gap in cases of$CuLiIn_2Se_4$ & $CuNaIn_2S_4$ respectively compared to their corresponding defect chalcopyrites.

10. Significant increment in band gaps are found in the case of $AgAlM_2$ (S, Se, Te) and AAl_2Se_4 (Ag, Cu, Cd, Zn) chalcopyrites due to structural distortion. But the effect is reversed in case of $ZnSnX_2$ ($X = P, As, Sb$), $CuInSe_2$, $CuIn_2S_4$, $CuIn_2Se_4$, $CuNaIn_2S_4$ and $CuLiIn_2Se_4$ compounds. That is, this effect leads to decrement in band gap for the above systems.

11. Quantitative estimate of the effect of cation-electronegativity on band gap in cases of $ZnSnX_2$ ($X = P, As, Sb$) chalcopyrites show that there is an increment of band gap with respect to their binary analogs $GaInP_2$, $InGaAs_2$ and $GaInSb_2$ respectively due to this effect.

12. Our study of linear optical properties for defect and substituted semiconductors show that optical properties strongly depend on optical matrix elements (OME) in the infrared and visible region of optical spectrum.

13. Optical properties in the UV region is mainly controlled by the joint density of states (JDOS).

14. Major structures and peaks in imaginary part of the dielectric function (ϵ_2) in infrared and visible region come from the contribution of OME in most of the cases. In few cases like $CuIn_2S_4$, $AgAl_2Se_4$ and $CuNaIn_2S_4$ JDOS always plays important role in this region of spectrum.

15. Significant effects of structural distortion and p-d hybridization are also found on ϵ_2, OME and JDOS of $CuIn_2S_4$, $AgAl_2Se_4$ and $CuNaIn_2S_4$ chalcopyrites.

16. Substitution by Na in $CuIn_2S_4$ and Mn & Oxygen in $ZnIn_2Te_4$ changes optical properties of the host significantly.

17. We have explicitly calculated the optical properties & OME for photon, polarized along c and $\perp$ to c-axis as well as the average value for all the above systems. The average value is calculated for $CuIn_2S_4$. Our study shows that chalcopyrites are anisotropic in nature and the properties get enhanced when photon is polarized $\perp$ to c-axis.

18. Calculation of static dielectric constants $\epsilon_1(0)$ agrees well with the available experimental result in case of $CdIn_2Te_4$ and $CdGa_2Te_4$.

19. Our calculation of ϵ_1 and ϵ_2 in the cases of $CdIn_2Te_4$ and $CdGa_2Te_4$ agrees well with the result of Ozaki et. al.

6.1 Future Works

Our detail study of structural, electronic and optical properties of group $I-III-VI_2$, $II-IV-V_2$, $I-III_2-VI_4$, $II-III_2-VI_4$ and $I_2-III-VI_4$ chalcopyrites reveal

that there are still many issues left to be addressed in future work. We list few of them.

1. Our unsatisfactory results in the case of $CuGaS_2$, $CuGaSe_2$, $CuGaTe_2$, $CuAlS_2$, $AgInS_2$, $AgInSe_2$, $AgInTe_2$ and $ZnGeP_2$ are to be explored further.

2. Magnetic properties of transition metal doped systems to be studied in detail because very little research work is carried out in this direction. It is also important because these doped systems are expected to be future devices for spintronics applications.

3. For the study of magnetic system, spin projected electronic properties are to be studied.

4. To study the magneto-optical properties of the transition metal doped chalcopyrite compounds.

5. The quantitative effect of cation electronegativity on band gap in group $II-IV-V_2$ compounds except $ZnSnX_2$ (X = P, As, Sb) are to be studied.

6. Optical properties of $I_2 - III - VI_4$ compounds are to be studied.

7. Chalcopyrite semiconductors are highly non-linear and therefore their non-linear optical properties are important. They are also found to have applications for non-linear devices. But very little studies of non-linear properties have been carried out. Hence we propose to carry out such studies within the frame work of TB-LMTO method.

8. Extensive research, including ours, have been carried out for 50% defect substituted in place of one of the cation. This is because such systems maintain translational

symmetry. Therefore existing computational techniques can be adopted. But defects or doping $< 50\%$ are also common and studied experimentally. Low concentration of vacancy defect or doping may also tailor various properties. Therefore study of low concentration vacancy defects/ doped is very necessary. But such defects/ doping make systems disordered. Different techniques are required to study disordered systems. There are two approaches to tackle such problems.

(a) To carry out supercell calculation within the same frame work as adopted in the case of 50% defects/doped. But number of atoms per unit cell increases by many fold. Therefore computational time is very large.

(b) Using some meanfield theories like 'Coherent Potential Approximation' [224] or 'Augmented Space Formalism' [223]. Ganguli et. al. [221, 222] have developed a formulation for optical properties of random semiconducting binary alloys using Augmented Space Formalism. The same may be extended to ternary systems also.

Bibliography

[1] Burdick C. L *et. al.*, J. Amer. Chem. Soc., **39** (1917) 2518.

[2] J.L. Shay, I.H. Wernick, Ternary Chalcopyrite Semiconductors: Growth, Electronic Properties and Applications, Pergamon Press, New York, 1975.

[3] Hahn H. *et. al.*, Z. Anorg.Chem., **271** (1953) 153.

[4] Goodman C. H. L. *et. al.* Physica., **20** (1954) 1107.

[5] Hahn H.*et. al.*, Z. Anorg. Allg. Chem., **279** (1955) 241.

[6] Parthe E., Crystal Chemistry of Tetrahedral Structures (Gordon and Breach, New York, 1964).

[7] Goryunova N. A., The Chemistry of Diamond-like semiconductors (Chapman and Hall, New York, 1965)

[8] Treusch J., Festkorperprobleme XIV, (Vieweg, Braunschweig, 1974), 229.

[9] Pankove J.O., Electroluminescence, (Springer, Berlin, 1977), 171.

[10] Treusch J., Festkorperprobleme XXI, (Vieweg Dortmund,1981), 149.

[11] Ehrenreich H*et. al.*, Solid State Physics., **36** (Academic, New York 1981).

[12] Pamplin B. R. *et. al.*, Prog. Cryst. Growth Charact., **1** (1979) 331 .

[13] Kazmerski L. L. Nuovo Cimento., **D2** (1983) 2013.

[14] Horinaka H. *et. al.*, J. Appl. Phys., **32** (Suppl. 32–33) (1993) 109.

[15] Shay J. L.*et. al.*, J. Appl. Phys., **43** (1972) 2805. Wagner S.*et. al*, Appl. Phys. Lett., **22** (1973) 351.

[16] Levine B.F., Phys. Rev.B., **7** (1973) 2600.

[17] Hopkius F. K., Laser Focus World., **31**(1995) 87.

[18] Wagner S.*et. al.*, Appl. Phqs. Lett., **25** (1974) 234.

[19] Gaber A.M.*et. al.*, ALP Conf. Proc., **306** (1994) 59.

[20] Abrahams S.C.*et. al.*, J. Chem. Phys., **59** (1973) 1925.

[21] Jackson A.G.*et. al.*, Infrared Phys. Technol., **38** (1997) 233.

[22] Rashkeev S.N.*et. al.*, Phys. Rev.B., **63** (2001) 165212.

[23] Tang L.C.*et. al.*, J.Phys.: Condens. Matter., **15** (2003) 6043.

[24] Lee M.H.*et. al.*, Phys.Rev.B., **70** (2004) 235110.

[25] Chemla D. S.*et. al.*, Opt. Commun., **3** (1971) 29.

[26] Radautsan S.I.*et. al.*, J. Appl. Phys., **32** (1993) 5.

[27] Joshia N.V.*et. al.*, Mater. Lett., **61** (2007) 1926.

[28] Gentile L.,*et. al.*, Cryst. Growth Charact., **10** (1985) 241.

[29] Koshkin V.M.*et. al.*, Chemistry Reviews., **19** (1994) 1 .

[30] Bi Z.*et. al.*, J. Am. Ceram. Soc., **86** (2003) 2059.

[31] Georgobiani A.N.*et. al.*, Sov. Phys. Semicond., **19** (1985) 1005.

[32] Koroleva L.I.*et. al.*, Physics of the Solid state., **51** (2009) 303.

[33] Park,*et. al*, J. Appl. Phys., **84** (1998) 1567.

[34] Johnson M.B. *et. al.*, Optics Communications., **233** (2004) 403

[35] Miyazaki H.*et. al.*, Journal of Physics and Chemistry of Solids., **64** (2003) 2055.

[36] Jaffe J.E.*et. al.*, Phys. Rev., B **29** (1984) 1882.

[37] Shaukat A.*et. al.*, J. Phys. Chem. Solids., **39** (1978) 1269.

[38] Jaffe J.E.*et. al.*, Phys. Rev., B **27** (1983) 5176.

[39] Jaffe J.E.*et. al.*, Phys. Rev., B **28** (1983) 5822.

[40] Lerner L. S., J. Phys. Chem. Solids., **27** (1966) 1.

[41] Honeyman W. N.*et. al.*, J. Phys. D: Appl. Phys., **4** (1971) 1182.

[42] Tell B.*et. al.*, Phys. Rev., B. **9** (1974) 5203.

[43] Tell B.*et. al.*, J. Appl. Phys., **43** (1972) 2469.

[44] Tang L.C.*et. al.*, J. Phys: Condens.Matter., **15** (2003) 6043.

[45] Tinoco T.*et. al.*, J.Phys. Chem. Solids., **56** (1995) 481.

[46] Gonzalez J.*et. al.*, Phys. Stat, Sol (b)., **223** (2001) 299.

[47] Mori Y.*et. al.*, Phys. Stat. Sol (b)., **211** (1999) 469

[48] Elliot E. Thin Solid Films., **20** (1974) S25.

[49] Padam G K, Mat. Res. Bull., **22** (1987) 789.

[50] Tuttle J R.*et. al.*, Solar Cells., **24** (1988) 67.

[51] Ashida A.*et. al.*, Mater. Sci. Lett., **13** (1994) 1181.

[52] Migliorato P.*et. al.*, Appl. Phys., **46** (1975) 1777.

[53] Horig W.*et. al.*, Thin Solid Films., **48** (1978) 67.

[54] Ashida A.*et. al.*, Proc. of Powder Metallurgy World Congress., (1993) 1172.

[55] Boyd G.D.*et. al.*, IEEE J. Quantum Electron., **7** (1971) 563.

[56] J.C Rife J.C.*et. al.*, Phys. Rev., B **16** (1997) 4491.

[57] Luciano M.J. *et. al.*, Appl.Phys.Lett., **23** (1973) 453.

[58] Andriesh A.M.*et. al.*,Phys.Stat.Sol., B **187** (1995) 83.

[59] Chichibu S.*et. al.*, J.Appl.Phys., **70** (1991) 1648.

[60] Alonso M.I. Phys. Rev., B **63** (2001) 075203.

[61] Sato K. Material Science in Semiconductor Processing., **6** (2003) 335.

[62] Aksenov I. J.Appl. Phys., **76** (1993) 3811.

[63] Nishikawa N.*et. al.* J. Appl. Phys., **34** (1995), part 2 (2B) : L223.

[64] Sato K. J. Appl. Phys., **35** (1996), part 1 (4A) : 2061.

[65] Artus L. J.Phys.C : Solid Stae Phys., **19** (1986) 5937.

[66] Shay J.L.*et. al.*, Phys.Rev., B **5** (1972) 5003.

[67] Hsu T.M. J. Appl. Phys., **69** (1991) 3772.

[68] Shay J.L. Phys. Rev. Lett., **24** (1970) 1301.

[69] Shay J.L. Phys. rev., B **3** (1971) 2004.

[70] Brudnyi V.N. semiconductors., **43** (2009) 1146.

[71] Gastaldi L. *et. al.*,Journal of Solid State Chemistry., **66** (1987) 251.

[72] Errandonea D. *et. al.*, Journal of applied Physics., **104** (2008) 063524

[73] Schwer H.*et. al.*, Kristallogr., **190** (1990) 103.

[74] Shand W.A. Journal of Crystal Growth., **5** (1969) 203.

[75] Ozaki S.*et. al.*, Phys. Rev., B **64** (2001) 085208.

[76] Ozaki S.*et. al.*, Journal of Applied Physics., **97** (2005) 043507.

[77] Ozaki S. *et. al.*, J Mater Sci: Mater Electron., **18** (2007) S347.

[78] Couturier G.*et. al.* Materials Science and Engineering., B **21** (1993) 333.

[79] You S.H.*et. al.*, Journal of Applied Physics., **95** (2004) 4042.

[80] Couturier G.*et. al.*, J. Appl. Phys., **701** (1991) 4472.

[81] Couturier G.*et. al.*, Appl. Phys., **73(4)**, (1993) 1813.

[82] Riede V. *et. al.*, Solid State Communications., **78** (1991) 211.

[83] Unger W.K.*et. al.*, Solid State Communications., **25** (1978) 913.

[84] You S.H.*et. al.*, Journal of Crystal Growth., **256** (2003) 116.

[85] Albornoz J.G.*et. al.*, Cryst. Res. Technol., **34** (1999) 1191.

[86] Ishida Y.*et. al.*, Phys. Rev. Lett., **91** (2003) 107202-1.

[87] Theodoropoulou S. Semiconductor. Sci.Technol., **24** (2009) 015014.

[88] Watanabe T. Solar Energy Mater & Solar cells., **49** (1997) 357.

[89] Watanabe T. Tech. Dig. 9th Int. Photovoltaic Science & Engineering Conf.,Miyazaki, Tokyo, (1996).

[90] Fukuzaki K. Appl. Phys. Lett., **73** (1998) L1478.

[91] Yao J. Journal of Solid state Chemistry., **182** (2009) 2579.

[92] Koroleva L.I. Physics of Solid State., **51** (2009) 303.

[93] Souilah M. Thin Solid Films., **517** (2009) 2145.

[94] Rabeh M.B. Journal of Optoelectronic and Biomedical Materials., **1** (2009) 70.

[95] Rabeh M.B. Physics Procedia., **2** (2009) 745.

[96] Rabeh M.B. Chalcogenide Letters., **6** (2009) 83.

[97] Zribi M. Thin Solid Films., **519** (2011) 3865.

[98] Tsai W.J. Thin Solid Films., **519** (2010) 1712.

[99] Zribi M. materials Letts., **60** (2006) 98.

[100] Chaki S.H. Acta Physica Polonica A., **116** (2009) 221.

[101] Scheer R. Thin Solid Films., **392** (2001) 1.

[102] Johnson M.B. Optics Communications., **233** (2004) 403.

[103] Slobodskyy A. Phys. Rev., B **82** (2010) 201105.

[104] Koteski V. Phys. Rev., B **81** (2010) 245213.

[105] Mitaray S. Thin Solid Films., **135** (1986) 251.

[106] Belhadj M. Phys.Stat.Sol., (b) **241** (2004) 2516.

[107] Delgado G.D. Chalcogenide Letters., **6** (2009) 293.

[108] Goya. Phys. Rev., B **64** (2001) 235208.

[109] Scheer R. Thin Solid Films., **361-362** (2000) 468.

[110] Shay J.L. *et. al.*, Phys. Rev. Letts., **29** (1972) 1162.

[111] Poplavnoi A.S.*et. al.*, Izv.Akad.Nauk SSSR, Neorg Mater., **7** (1971) 1706.

[112] Poplavnoi A.S.*et. al.*, J.Sov.Phys., **19** (1976) 689.

[113] Yoodee K. Phys. Rev., B **30** (1984) 5904.

[114] Kane O.E. J.Phys.Chem.Solids., **1** (1957) 249.

[115] Oguchi T. ‘proceedings of the fourth International Conference on Ternary and Multinary Compounds’, Tokyo, Japan J.Appl.Phys., **19** (1980) 19-3

[116] Wei S.H. J.Appl.Phys., **78** (1995) 3846.

[117] Maeda T. Journal of Physics and Chemistry of solids., **66** (2005) 1924.

[118] Wei S.H. Journal of Physics and Chemistry of solids., **66** (2005) 1994.

[119] Chen S. Phys. Rev., B **75** (2007) 205209.

[120] Abdellaoui A. Journal of Alloys and Compounds., **487** (2009) 206.

[121] Jayalakshim V. J. Phys.Chem.Solids., **67** (2006) 669.

[122] Reshak A.H. J. Solid State Communication., **145** (2008) 571.

[123] Parlak C. J.Phys. Rev., B **73** (2006) 245217.

[124] Kopytov A.V. Physics of the Solid States., **51** (2009) 2115.

[125] Laksari S. Computational Material Science., **38** (2006) 223.

[126] Kumar V. J. Phys.Chem.Solids., **71** (2010) 1513.

[127] Meng Q.B. Solid State Communication., **107** (1998) 369.

[128] Xue D.*et. al.*, Phys. Rev., B **62** (2000) 13546.

[129] Jaffe J.E.*et. al.*, Phys. Rev., B **30** (1984) 741.

[130] Martins J.L. Phys. Rev., B **32** (1985) 2689.

[131] Chiker F. Solid State Communication., **151** (2001) 1568.

[132] Chiker F. Materials Science and engineering., B **98** (2003) 81.

[133] Basalaev Y.M. Russian Physics Journal., **48** (2005) 78.

[134] John R. Solid State Phenomena., **124-126** (2007) 57.

[135] John R, Computational Material Science., **44** (2008) 106.

[136] Phillips J.C. J.Phys.Chem.Solids., **35** (1974) 1205.

[137] Person C. Phys. Rev. Letts., **91** (2003) 266401.

[138] Lany S. Phys. Rev. Letts., **100** (2008) 066401.

[139] Jiang X. Phys.Rev., B **69** (2004) 035201.

[140] Lavrentyev A.A. Bulletin of the Russian Academy of Sciences:Physics., **73** (2009) 1140.

[141] Jiang X.S. Chin. Phys. Lett., **26** (2009) 077102.

[142] Baldereschi A. Solid State Communication., **21** (1977) 113.

[143] Lavrentyev A.A. Journal of Physics and Chemistry of Solids., **64** (2003) 1251.

[144] Ouahrani T. Journal of Solid State Chemistry., **183** (2010) 46.

[145] Singh P. Journal of Physics and Chemistry of Solids., **72** (2011) 1414.

[146] Reshak A.H. Current Opinion in Solid State and Material science., **12** (2008) 14.

[147] Ganguli B. Physica B**348**(2004) 382.

[148] Ayeb Y. computational Material Science., **50** (2010)651.

[149] Mahadevan P. Phys.Rev.Lett., **88** (2002) 047205.

[150] Zhao Y.J. Phys. Rev. B **63** (2001) 201202, (2002) Phys. Rev., B **65**, 094415.

[151] Aguilera I. Thin Solid Films. **516**,(2008) 7055.

[152] Palacios P. Thin Solid Films., **515** (2007) 6280.

[153] Krivosheeva A.V. J. Phys.: Condens. Matter., **21** (2009) 045507.

[154] Yamamoto T. J.Appl. Phys., **37** (1998) L1478.

[155] Yamamoto T. Applied Surface Science., **159-160** (2000) 345.

[156] Yi. Physica., B **359-361** (2005) 1466.

[157] Lany S. Phys. Rev. Letts., **100** (2008) 016401.

[158] Kilic C. Applied Phys. Lett., **83** (2003) 2007.

[159] Lany S. Journal of Applied Physics., **100** (2006) 113725.

[160] Zunger A. Applied Physics Letters., **83** (2003) 57.

[161] Lany S. Applied Phys. Lett., **86** (2005) 042109.

[162] Persson C. Phys. Rev., B **72** (2005) 035211.

[163] Jiang X.S.*et. al.*, China Phys. Lett. , **26** (2009) 077102.

[164] Born M.*et. al.*, Ann. Phys. (Leipzig) **84** (1927) 457.

[165] J. C. Slater, Quantum Theory of Molecules and Solids, Vol. IV (McGraw Hill, NewYork) (1974).

[166] Hohenberg P. *et. al.* , Phys.Rev **136**, B (1964) 864.

[167] Kohn W. *et. al.*, Phys. Rev. **140** A (1965) 1133.

[168] J.C. Slater, Phys.Rev **81** (1951) 385.

[169] Von Barth U. *et. al.* , J. Phys. C:**5** (1972) 1629.

[170] J. F. Janak *et. al.* , Phys. Rev. B **12**, (1975)1257 ; **11**, (1975) 1522; **6**, (1972) 4367.

[171] J.C. Slater, Int.J.Quantum Chem. **5S** (1971) 403.

[172] O.K. Andersen, Phys.Rev. B **12** (1975) 3060.

[173] Jepsen O. *et. al.* Solid State Communication **9** (1971) 1763.

[174] “Electronic structure and total energy calculation methods for solid :Tight binding and Linear methods” by G.P. Das (BARC), Electronic structure and Physics of materials, SERC School, S.N. Bose National Center for Basic Sciences (1999).

[175] O. K. Andersen, in ”Computational Methods in Band Theory“ eds. P.M. Marcus. J.F. Janak and A.R. Williams (Plenum, NewYork, 1971), 178.

[176] O.K. Andersen, ”Band structure of transition metals“ , in Mont Tremblant International Summer School (1973), unpublished.

[177] H. Skriver, ”The LMTO method“, Springer, NewYork, (1984).

[178] Andersen O.K.*et. al.*, in ”Electronic band structure and its applications, vol.283 of Lecture notes in Physics, Ed. M. Yussouff, Springer Verlag, Berlin, 1987, 1.

[179] Andersen O.K. *et. al.* , in “Applications of Multiple scattering Theory in Materials Science”, eds. Butler W.H. *et. al.*, (Mat.Res.Soc.Proc. 253, Pittsburgh, (1991), 37.

[180] Andersen O.K. *et. al.* , Phys. Rev. Lett. **53** (1984) 2571.

[181] Andersen O.K. *et. al.* , in “Highlights in Condensed matter Theory”’ Eds. F.Bassani, F.Fumi and M.P.Tosi, North-Holland, Amsterdam (1985) 59.

[182] P. Blochl, Phd. Dissertation, Stuttgart University (1989).

[183] Parkes J. *et. al.* , J. Appl. Cryst. **6** (1973) 414.

[184] Vaipolin A. A. *et. al.* , Phys. Status Solidi **29** (1968) 435.

[185] Vaipolin A. A. , Sov. Phys.-Solid State **15** (1973) 965.

[186] Cohen M. L. , Phys. Rev. B **32** (1985) 7988.

[187] Gaith M. *et. al.* , Adv. Mater Sci. **21** (2009) 183.

[188] Fauret R. et. al., Phys. Rev. B **47** (1993) 8269.

[189] Wei S.H. *et. al.* , Phys. Rev. B **58** (1998) R1710.

[190] H. Neumann *et. al.* , Cryst. Res.Technol. **23** (1988) 97.

[191] Bernard J.E. *et. al.* , Phys. Rev. B, **37** (1988) 6835.

[192] Suzuki M. *et. al.* , Jpn.J.Appl.Phys. **36** (1997) L1139.

[193] O. Madelung, in: O. Madelung (Ed.), Numerical Data and Functional Relationship in Science and Technology, Landolt-Börnstein, New Series, Vol. 17h, Springer, Berlin, 1985.

[194] Neumann H. *et. al.* , Crystal Research and Technology **28**, (1993) 635.

[195] Weise S. *et. al.* , Journal of Crystal Growth **166** (1996) 718.

[196] Abdellaoui A.*et. al.* , J. Alloys Compds. **487** (2009) 206.

[197] Goryunova N. A. *et. al.* , Fiz. Tekh. Poluprov. **2** (1968) 1344 .

[198] L. Pasemann, Phys. Stat. sol. (b) **56** (1973) K69.

[199] Rud Y. V. *et. al.* , Fiz. Tekh. Poluprov. **2** (1968) 893.

[200] Scott W. , J. Appl. Phys. **44** (1973) 5165.

[201] Krauss G. *et. al.* , Cryst. Res. Technol. **32** (1997) 223.

[202] Gourmelon M. W. E. *et. al.* , Proc. 28th IEEE PVSC (2000) 454.

[203] Gloeckler M. *et. al.* , The Journal of physics and chemistry of solids **66** (2005) 1891.

[204] E. Gusev, Defects in High-k Gates Dielectric Stacks, NATO Science Series II, Mathematics, Physics and Chemistry, Springer, New York, (2006).

[205] Sahin S. *et. al.* , Journal of Alloys and Compounds **529** (2012) 1.

[206] Kradinova L. V. *et. al.* , Phys. Stat. Sol. (A)**5** (1971) K137.

[207] Animalu Alexander O.E. ,"Intermediate Quantum Theory of Crystalline Solids" (Prentice Hall of India Private Limited, Newdelhi (1978).

[208] Kubo, J.Phys.Soc.Japan **12**, (1957) 570 .

[209] Zavetova M. *et. al.* , "The optical properties of solids-New developments", edited by B.O. Seraphin (North-Holland Publishing company, Amsterdam (1976).

[210] Yu Uspenski A. *et. al.* , Z.Phys. B **53**, (1983) 263.

[211] Alouani M. *et. al.* , J.Phys. F : Met. Phys. **16**, (1986) 473.

[212] Alouani M. *et. al.* , Phys. Rev. B **37**, (1988) 1167.

[213] Zemach R. *et. al.* , Phys. Rev. B **39**, (1989) 1891.

[214] Hobbs D. *et. al.* , J.phys : Condens.Matter **7**, (1995) 2541.

[215] M.E. Rose , “Elementary theory of angular momentum” (New York :Wiley) (1957).

[216] Gilat G. *et. al.* , Phys. Rev **144**, 390 (1966); Phys.Rev. **157**, (1967) 586.

[217] Lehmann G. *et. al.* , Phys. Status. Solidi **54**,(1972) 469 .

[218] Dennery P. *et. al.* , ”Mathematics for Physicsts“ (New York : Harper International) (1967).

[219] Smith N. V., Phys.Rev. Lett. **21** (1968) 96.

[220] Mahan G. D., Phys. Letts. **24** A (1967) 708.

[221] Ganguli B. et. al., International Journal of Modern Physics B **15** (2000) 1537.

[222] Ganguli B. et. al., International Journal of Modern Physics B **16** (2002) 3681.

[223] Mookerjee A., J. Phys. C **6** (1973a) L205; (1973b) 1340; J. Phys. C **8** (1975a) 24 ; (1975b) 1524.

[224] Soven P., Phys. Rev. **156** (1967) 1809.

PUBLICATIONS

- **Published :**

1. S. Mishra, B. Ganguli, 'Effect of p-d hybridization and structural distortion on the electronic properties of $AgAlM_2$ (M = S, Se, Te) chalcopyrite semiconductors', Solid State Communications **151** (2011) 523-528.

2. S. Mishra, B. Ganguli, 'Electronic and Structural Properties of AAl_2Se_4 (A = Ag, Cu, Cd, Zn) Chalcopyrite Semiconductors', Journal of Solid State Chemistry, **184**, Issue 7 (2011) 1614-1621.

3. S. Mishra, B. Ganguli, 'Effect of structural distortion and nature of bonding on the electronic properties of defect and Li-substituted $CuInSe_2$ Chalcopyrite Semiconductors', Journal of Alloys and Compounds **512** (2012) 17-22.

4. S. Mishra, B. Ganguli, 'Structural, electronic and optical properties of oxygen and Mn substituted $ZnIn_2Te_4$ chalcopyrite semiconductors.', SPIE : International Society for Optics and Photonics (accepted 2012-May).

5. Biplab Ganguli and Surabala Mishra, "Structural, electronic and optical properties of defect Cu_2InSe_4 and Ga, Al substituted $CuInSe_2$ chalcopyrite semiconductors " , Ed. by S. Jayakumar, P. Ravindran, R. Arun Kumar and C. Sudarshan, "Crystal Growth and Computational Materials Science : MACMILLAN Advanced Research Series", Macmillan Publishers India Ltd., (2012) 250-253.

- **Conference Papers presented :**

1. Title : 'Electonic and Structural Properties of Doped $CuInX_2$ (X = Se, T e)

Semiconductors' presented in XVth International Workshop on the Physics of Semiconductor Devices (IWPSD-2009) jointly organised by Solid State Physics Laboratory & Jamia Millia Islamia, New Delhi, India from 14th-19th Dec. 2009.

2. Title : 'Band gap tailoring by p-d hybridization in doped $CdGa_2S_4$ chalcopyrite semiconductors" presented in DAER-BRNS International Conference on Physics of Emerging Functional Materials (PEFM-2010) organised by Bhabha Atomic Research Center, Mumbai, India, 22nd-24th Sep. 2010.

- **Papers to be communicated :**

1. 'Effect of cation-electronegativity, p-d hybridization and structural distortion on electronic properties of $ZnSnX_2$ (X = P, As, Sb) chalcopyrite semiconductors' to **Journal of Solid State Chemistry**.'
2. 'Effect of Na substitution on electronic and optical properties of defect $CuIn_2S_4$ chalcopyrite semiconductor' to **Solid State Communication**.
3. 'Effect of structural distortion and p-d hybridization on the electronic and optical properties of $CdIn_2Te_4$' to **Material Chemistry and Physics**.
4. 'Effect of structural distortion on optical properties of $CdGa_2X_4$ defect chalcopyrite semiconductors' to **Optical Material**.